Fine-Time-Resolution Passive RF Source Imaging

PhD Thesis

William T. Coventry

Centre for Signal and Image Processing

Electronic and Electrical Engineering

University of Strathclyde, Glasgow

January 29, 2023

This thesis is the result of the author's original research. It has been composed by the author and has not been previously submitted for examination which has led to the award of a degree.

Abstract

With the electromagnetic spectrum more congested than ever, the task of passively monitoring the spectrum to detect, separate, identify and locate emitters is fraught with difficulty. Enabled by modern solid state RF technologies, Radar and communications systems are more agile, providing a foundation for low probability of intercept (LPI) emitters to exist for both, Radar and communications systems. One of the key characteristics is a broadband, spread-spectrum modulation scheme.

Previous efforts in this area have focussed on improving signal to noise and signal to interference plus noise ratios (SNR and SINR) of LPI emitters using various time and frequency domain methods. This neglects an important aspect of electronic surveillance - the spatial domain using antenna arrays. Current literature on antenna array signal processing exploits the simplifications inherent in the frequency domain at the expense of limiting these techniques to narrowband signals and making them inadequate for broadband sources.

This thesis addresses spatio-temporal antenna array signal processing for LPI emitters in order to improve spatial resolution for signal separation. One of the key tools throughout this thesis is the use of polynomial matrices and the polynomial eigenvalue decomposition that allow spatial super resolution techniques, such as the MUSIC algorithm, to be extended to the broadband domain.

Results are demonstrated via simulations and statistical analysis throughout this thesis, concluding that while computationally expensive, the novel methods contained within this thesis provide an attractive solution to the processing of LPI emitters.

List of Acronyms

AWGN	Additive White Gaussian Noise
CPU	Central Processing Unit
CW	Continuous Wave
CWD	Choi-Williams Distribution
dB	Decibels
DFT	Discrete Fourier Transform
DoA	Direction of Arrival
EM	Electromagnetic
ES	Electronic Surveillance
ESPRIT	Estimation of Signal Parameters by Rotational Invariance Techniques
EW	Electronic Warfare
FFT	Fast Fourier Transform
FIR	Finite Impulse Response
FMCW	Frequency Modulated Continuous Wave
FPGA	Field Programmable Gate Array
FSK	Frequency Shift Keying
GPU	Graphics Processing Unit
i.i.d	independent and identically distributed
LFM	Linear Frequency Modulation
LFMCW	Linear Frequency Modulated Continuous Wave
LPI	Low Probability of Intercept
MIMO	Multiple Input Multiple Output
MRA	Minimum Redundancy Array
MUSIC	Multiple Signal Classification

MVDR	Minimum Variance Distortionless Response
pdf	Probability Density Function
PDW	Pulse Descriptor Word
PEVD	Polynomial Eigenvalue Decomposition
PMUSIC	Polynomial MUSIC
POI	Probability of Intercept
PRI	Pulse Repetition Interval
PSD	Power Spectral Density
SAR	Synthetic Aperture Radar
SMD	Sequential Matrix Diagonalization
SNIR	Signal to Interference plus Noise Ratio
SNR	Signal to Noise Ratio
SoC	System on chip
SP-MUSIC	Spatial Polynomial MUSIC
SSP-MUSIC	Spatio-Spectral Polynomial MUSIC
STFT	Short Time Fourier Transform
SWAP	Size, Weight And Power
TDoA	Time Difference of Arrival
ULA	Uniform Linear Array
WSS	Wide Sense Stationary
WVD	Wigner-Ville Distribution
WVHT	Wigner-Ville Hough Transform

List of Symbols

To conform with standard notation, vectors and matrices are denoted via lower- and uppercase bold letters, for example $\boldsymbol{a}$ and $\boldsymbol{A}$. Non-bold variables represent scalars. Efforts have been made to keep all variables unique throughout this thesis, however, some variable names are re-used in different chapters.

List of Symbols

$\boldsymbol{A}$	Array manifold vector
B	Bandwidth
c	Speed of Light
d	Distance between antenna elements
δ	Sensitivity
$\delta(n-\tau)$	Ideal Fractional Delay Filter of delay τ
$\delta(n)$	Kronecker Delta Function
$\delta(t)$	Dirac Delta Function
$DFT\{\cdot\}$	Discrete Fourier Transform
$e^{\cdot}$	Exponent
$E[\cdot]$	Expectation operator
$F(\theta)$	Far-field Radiation Pattern
$FFT\{\cdot\}$	Fast Fourier Transform
$G_{\{\cdot\}}$	Gain in relation to parameter
$\boldsymbol{I}$	Identity matrix
i, j, p, q, k	Generic index between defined bounds

j	Square root of -1
k	Boltzmann constant
K	Number of Sub-arrays in Spatial Smoothing
L	Number of signals
$L_{\{\cdot\}}$	Loss due to parameter in subscript
$\mathbf{\Lambda}$	Eigenvalue Matrix
λ	Wavelength
λ_i	i^{th} eigenvalue
M	Number of elements in array (in array context)
M	Number of Scan Positions (in a radar Context)
$\mathcal{M}$	Difference set
$\mathcal{C}$	Complex Number
n	Discrete time index
N	Number of (context dependent)
$\nu(t)$	Additive White Noise
$\boldsymbol{O}$	Zero matrix
ω	Angular Frequency
ω_c	Carrier Angular Frequency
ω_d	Down Converting Angular Frequency
$P_{\{\cdot\}}$	Power related to parameter
p, q	Intermediate variables used in derivations and analysis
$P(\theta, \omega)$	Spatio-spectral spectrum
$P(\theta)$	Spatial Spectrum
R	Range
$\boldsymbol{R}_{ij}$	Covariance matrix between variables i and j
$s(t)$	Source signal
σ	Radar cross section (in radar context)
$\sigma_{\{\cdot\}}$	Standard deviation
$\sigma^2_{\{\cdot\}}$	Variance
$\text{sinc}\{\cdot\}$	Sinc function

t	Continuous time index
T_0	Standard temperature (290K)
T_s	Sample Period
T_x	Time span
τ	Lag parameter
τ_c	Chirp Duration
$\hat{\tau}$	Normalised Delay in Samples
τ_l	Time delay between elements for source l
θ	Direction of Arrival
$\boldsymbol{U}$	Eigenvector Matrix
$\boldsymbol{U}_n$	Noise Subspace Eigenvector
$\boldsymbol{U}_s$	Signal Subspace Eigenvector
$\hat{v}$	Velocity
$\boldsymbol{w}$	Array Weights
$w(u)$	Array Weight Function
$\boldsymbol{x}(t)$	Measured signal
$\langle\cdot\rangle_{ij}$	ij^{th} element of matrix
$\langle\cdot\rangle_i$	i^{th} element of vector
$\otimes$	Convolution Operator
$\odot$	Kronecker Product
$\in$	Member of
$\forall$	For All

Superscript

$\{\cdot\}^*$	Complex Conjugate
$\{\cdot\}^T$	Transpose
$\{\cdot\}^H$	Hermitian operator
$\{\cdot\}^P$	Parahermitian operator

Contents

List of Figures

List of Figures

List of Tables

Acknowledgements

This thesis has been conducted at the Department of Electronic and Electrical Engineering of Strathclyde University.

First, I would like to thank my academic supervisors, Dr Carmine Clemente and Professor John Soraghan for their excellent and invaluable guidance, encouragement and contribution to the development and completion of this thesis. Under their supervision, I developed strong fundamental skills to become a researcher, including analytical thinking and creativity to find innovative solutions.

Major thanks to my industrial supervisor, Dr Neil Cade from Leonardo UK Ltd. Our periodic technical meetings were instrumental to many of the novel techniques presented within this thesis. His wealth of industry expertise helped drive general direction to ensure the research outputs could positively impact real-world applications.

Special thanks to my friends and family for their support throughout this studentship. Extra special thanks to my partner, Varisha, for her continued love, support and utmost patience over the last few years.

Finally, I would like to thank my sponsors, Leonardo UK Ltd and EPSRC for funding this studentship. Without them, this work would not have been possible.

Chapter 0. Acknowledgements

Chapter 1

Introduction

1.1 Preface

Recent years have shown a strong convergence of radar and communications systems. In the past, radar systems were limited to the higher frequencies, and characterised by their short, high power pulses in order to meet range and Doppler requirements. Conversely, communications systems were mainly at the lower frequencies due to lower atmospheric absorption promoting a greater range. This is no longer the case. This is largely enabled by advances in solid state RF technology, allowing devices to be highly agile, more efficient, lower power, smaller physical sizes or even lower cost. Now, there are more wireless devices than ever before exploiting the use of the electromagnetic spectrum. The congestion of the electromagnetic spectrum is further exacerbated by spectrum users demanding greater data rates and wider bandwidths. This includes radar systems that can also exploit the agility of modern solid state RF technology to avoid detection.

Modern radars are a vital piece of technology in today's world of defence. They provide the ability to detect and identify threats and estimate their range and velocity with high accuracy, even in highly cluttered and/or contested electromagnetic environments. Radar technology has constantly evolved since its inception in the early 20^{th} century, and this evolution was accelerated by military needs as well as advances in technology. The classic radar is characterised by a circular or raster scanning pattern, with

a consistent transmit pattern. The modern radar is considerably more sophisticated with advanced scan patterns to interleave acquisition and track modes of the radar, also known as 'track while scan'. In addition, a modern radar may try to deliberately avoid detection via low probability of intercept (LPI) design characteristics.

Electronic warfare (EW) is an all-encompassing term for monitoring use of the electromagnetic spectrum, including identifying, classifying, disabling or even exploiting adversary communications and radar emissions. Electronic Surveillance (ES) is the branch of EW that focuses on detection, identification and localisation of electromagnetic emissions. However, the increased level of congestion within the electromagnetic spectrum, along with emerging technology of LPI radar systems poses a significant challenge for future ES technology.

The general properties of LPI emissions include broad bandwidth, long pulse length, sophisticated modulations and low antenna sidelobes. Conventional time domain approaches do not provide sufficient processing gain to detect weak LPI emissions. Frequency domain approaches can provide some processing gain, but only at the expense of reduced temporal fidelity. There is a considerable amount of existing literature that proposes the use of time-frequency distributions to get the best from both domains.

Another domain that can also be exploited is the spatial domain. By sampling in space through an array of antennas, another key emitter parameter can be extracted - its direction of arrival (DoA). Super-resolution DoA estimation algorithms have been a popular research area for quite some time. However, most techniques simplify the problem by using a narrowband assumption. This is inadequate for broadband LPI emissions.

This thesis studies and evaluates novel spatio-temporal array signal processing techniques for the detection and localisation of LPI emissions. Results are demonstrated via simulations and statistical analysis.

1.2 Contribution

The key contributions of this thesis are:

- A multi-correlation antenna array/receiver architecture for enhanced spatio-temporal processing of LPI emitters.
- Extension of the Root MUSIC algorithm to polynomial matrices to achieve broadband angular super-resolution with reduced computational complexity.
- Development of broadband emitter decorrelation methods (spatial smoothing, and Doppler induced spatial smoothing) in the context of polynomial matrix representations.
- Demonstrating the practicality of sparse array signal processing using polynomial matrix methods.

1.3 List of Publications

Many of the results presented in this thesis have been the subject of refereed journal and conference publications. These publications are listed below.

- Coventry, W., et al.: Bearing estimation of low probability of intercept sources via polynomial matrices and sparse linear arrays. IET Radar Sonar Navig. 15(11), 1408– 1419 (2021). https://doi.org/10.1049/rsn2.12133
- Coventry, W., Clemente, C. and Soraghan, J. (2019), Broadband direction of arrival estimation via spatial co-prime sampling and polynomial matrix methods. The Journal of Engineering, 2019: 6259-6263. https://doi.org/10.1049/joe.2019.0192
- W. Coventry, C. Clemente and J. Soraghan, "Enhancing polynomial MUSIC algorithm for coherent broadband sources through spatial smoothing," 2017 25th European Signal Processing Conference (EUSIPCO), 2017, pp. 2448-2452, doi: 10.23919/EUSIPCO.2017.8081650.

- W. Coventry, C. Clemente and J. Soraghan, "Polynomial Root-MUSIC Algorithm for Efficient Broadband Direction of Arrival Estimation," 2017 Sensor Signal Processing for Defence Conference (SSPD), 2017, pp. 1-5, doi: 10.1109/SSPD.2017.8233256.
- W. Coventry, C. Clemente and J. Soraghan, "Broadband Sparse Sensing: A Polynomial Matrix Approach to Co-Prime and Super Nested Arrays," 2019 IEEE Radar Conference (RadarConf), 2019, pp. 1-6, doi: 10.1109/RADAR.2019.8835665.
- C. V. Ilioudis et al., "GNSS Based Passive Radar for UAV Monitoring," 2019 IEEE Radar Conference (RadarConf), 2019, pp. 1-6, doi: 10.1109/RADAR.2019.8835606.

1.4 Thesis Organisation

This Thesis is organised as follows:

Chapter 2 provides the problem formulation behind the techniques developed throughout this thesis and introduces radar and ES systems, with emphasis on the existence of low probability of intercept radars as well as advanced signal processing functions to counter such emitters. The basic functionality of a radar system is discussed, with particular attention paid to waveform, antenna and operational parameters which affect its maximum range. Conversely, analysis is provided to demonstrate how a radar designer can modify these parameters to reduce the maximum interception range of the intercept receiver. This concept is expanded by a literary review into techniques to reduce the maximum interception range, while maintaining a good radar detection range, thus describing the key design features of a low probability of intercept radar.

The corresponding literature on advanced ES techniques is also presented, with an emphasis on the relevance to detection of LPI emitters. Here the emphasis is on time-frequency distributions and their use in increasing processing gain. This emphasis is driven by the fact that current literature addressing LPI emitters has largely focussed on such time-frequency methods and neglected spatial processing.

Chapter 3 introduces the concept of spatial processing using a fully digital antenna array, optimal sensor placement and advanced processing techniques. A literature review is provided on direction of arrival (DoA) methods, specifically those which can

achieve super resolution. Super resolution is the ability to estimate the directions of more than one source within a typical antenna beam-width. This chapter also discusses various sparse array geometries and processing techniques to exploit the properties of sparse arrays. However, all of the aforementioned techniques in literature have heavily focussed on processing for the narrowband signal problem and, as discovered in Chapter 2, are inapplicable to broadband low probability of intercept emitters. The Chapter then discusses broadband array processing techniques discovered in literature, and concludes that very recent polynomial matrix techniques provide a promising solution to the broadband array processing problems.

The first novelty of this thesis is discussed in Chapter 4: the proposal and analysis of a multi-correlation receiver. This Chapter begins with a toy problem with only two channels to highlight the benefit of correlation analysis methods over conventional Fourier based techniques. This is then generalised to the case of an arbitrary number of sensors within a linear aperture. The second novelty discussed within this Chapter is an algorithm for direction of arrival estimation of broadband emitters with a significant reduction in computational cost. These techniques are then analysed using (a) a simulation of a particularly challenging example of two LPI waveforms and (b) Monte Carlo analysis to highlight and calculate the reduction in computational cost with no reduction in estimator accuracy.

Chapter 5 addresses the problem of estimating the direction of arrival of multiple strongly correlated or coherent emitters. Coherent signals pose a problem to subspace based super-resolution methods, and this Chapter provides analysis that highlights the difficulties. A novel technique is proposed in order to effectively decorrelate the coherent broadband sources, and regain the super resolution property of the DoA estimator. In addition, this section covers a novel analysis which suggests that the spatial averaging effect arises naturally for an array in motion due to slight differences in Doppler shift of the emitters at different angles.

Up until this point in the thesis, all analysis has been focussed on the case of a uniform linear array (ULA). For a wideband system, a ULA is an inefficient design. Close antenna spacings are required for ambiguity free DoA estimates of the higher

frequency sources, yet a wide overall aperture is required for sufficient resolution of lower frequency sources. Thus, if designed using a ULA, many antenna elements are required to meet both objectives, increasing overall size, weight and power of the system. To combat this, Chapter 6 introduces novel signal processing to exploit the geometries of some sparse arrays. Techniques in this Chapter also involve leveraging the novel algorithms developed in Chapters 4 and 5. Simulations are provided to analyse (a) the performance of the techniques in a multi-emitter environment (b) the accuracy of the novel techniques through Monte-Carlo analysis and (c) the resolution of the techniques, also presented via Monte-Carlo analysis.

Finally, Chapter 7 provides concluding remarks of this thesis, which include areas where the techniques presented may be leveraged for real-world applications. This chapter also discusses future work required to support such exploitation into real-word applications.

Chapter 2

Radar And Electronic Surveillance Systems

2.1 Introduction

While Electronic Surveillance (ES) is the primary application focus of the algorithms and methods discussed throughout this thesis, it is intuitive to start by discussing modern radar systems themselves. In this chapter, the basic principles of both conventional and modern radars are covered in Section 2.2. This provides a foundation for understanding the requirements of modern ES systems, and identifies the key challenges in this area. Following this, Section 2.3 discusses advances in modern radar technology which enable the radar to avoid being detected or intercepted, including techniques involving advanced antenna and waveform design, and advanced operation techniques. Section 2.3.5 covers advanced ES system design and methods proposed in zthe literature in effort to improve ES performance and enhance detection capabilities. This section also identifies a gap in the literature where such methods alone are insufficient, and how the novel signal processing presented throughout this thesis can fill this gap.

2.2 Radars and Intercept Receivers

The basic concept of a radar system exploits the fact that electromagnetic (EM) energy transmitted from an emitter may be reflected, or scattered from a surface towards a receiver. The physics behind the propagation and scattering of EM waves is outside the scope of this thesis, but can be found in [1]. In the simple case of a monostatic radar, whereby the transmitter and receiver are co-located, zthe object range, R,

$$R = \frac{c\Delta T}{2}, \tag{2.1}$$

zcan be estimated by measuring the round trip delay, ΔT, where c is the EM propagation speed in the medium. In order to locate an object in a two- or three- dimensional space, the radar system requires angular information. Typically, this is achieved through pointing a highly directional antenna in a specific direction, and overall spatial awareness is gained through mechanically or electrically scanning over an angular range (or search volume). The total time to search this volume is defined by the scan frame time, T_{fs}z,

$$T_{fs} = MT_d, \tag{2.2}$$

where T_d is dwell time, defined by the number of pulses and pulse repetition interval (PRI) to achieve range-Doppler requirements, and M is the total number of scan positions to cover the volume which is calculated as

$$M = \frac{\Omega}{\phi_3\theta_3}, \tag{2.3}$$

where Ω is the total angular area for the search (in steradians), and ϕ_3 and θ_3 are the azimuth and elevation beamwidths [2]. Clearly, there is a trade space between angular resolution and scan frame time. The following is not an exhaustive list of radar scan patterns, however, it does discuss key scanning methods to highlight challenges for the ES receiver in the following section.

The more traditional approach to radar scanning is to mechanically steer a highly

directional antenna to each one of the scan positions in a sequential manner. A circular scan can be seen in Figure 2.1 and involves using an antenna with a large beamwidth in elevation, and narrow in azimuth. Due to the large elevation beamwidth, the radar only needs to scan in azimuth - simplifying the search.

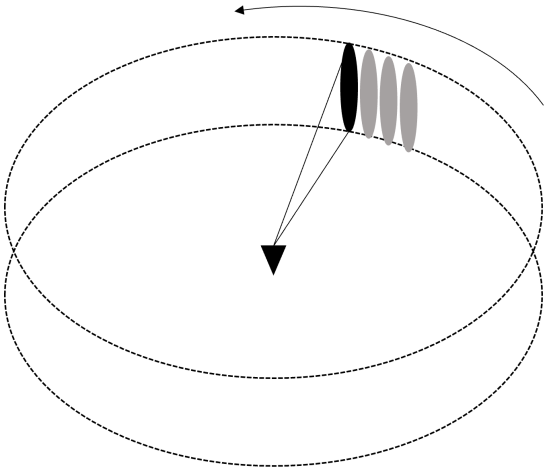

Figure 2.1: Circular Scan

While simple, such a scanning method provides no elevation information. A raster scanning pattern is similar to a circular scan, however, an antenna with a relatively narrow beamwidth in both azimuth and elevation is used. This is illustrated in Figure 2.2.

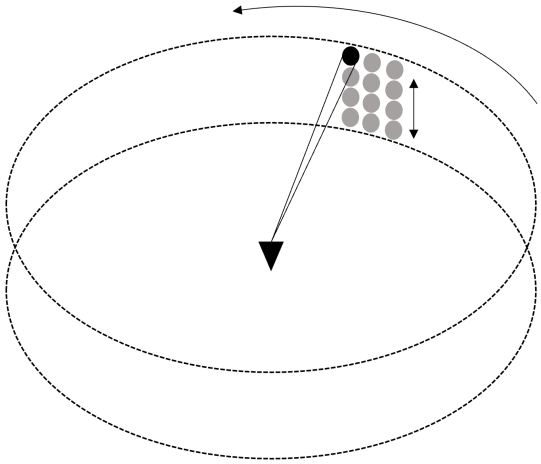

Figure 2.2: Raster Scan

The disadvantage of such an approach is that the radar is looking in only one direction at a time with a relatively long scan frame, potentially missing significant targets. By using a modern AESA (active electronically scanned array) based radar system, more advanced scanning techniques can be adopted, which allow the radar to perform several functions simultaneously, such as track while scan [3]. This is enabled by highly agile electronic scan capabilities, including forming multiple beams and simultaneously tracking multiple targets as illustrated in Figure 2.3.

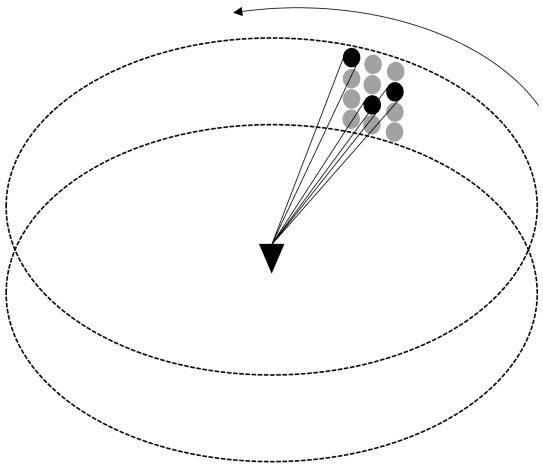

Figure 2.3: Multi-beam Scan

At the more extreme end of this, a radar can transmit omnidirectionally, and form many parallel spatial beams on receive to locate multiple targets simultaneously with a zero time scan frame. This is shown in Figure 2.4. This approach has recently been used in [4] in their 'Holographic Radar', citing a 'staring not scanning' approach. The clear disadvantage of this method is that due to a considerably lower transmit antenna gain, the system needs to transmit with a considerably higher power to maintain the same maximum range. In addition, estimating the location of several targets simultaneously over a large area forces a considerably higher size, weight and power (SWAP) requirement as large fully digital antenna arrays are required.

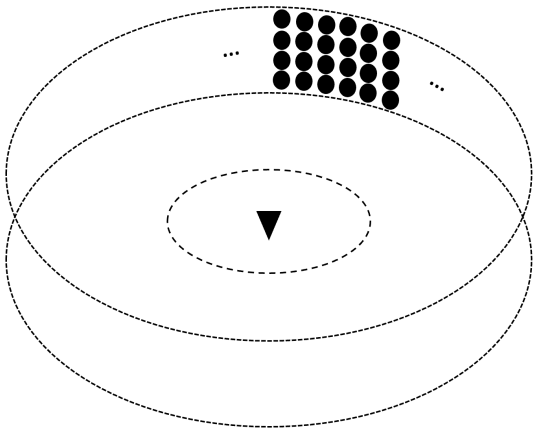

Figure 2.4: Omni Scan Radar

The key purpose of an ES system is to passively gain situational awareness in the RF domain through the interception, classification, identification and localisation of emitters.

In order to intercept an emitter such as a radar, the ES system needs to monitor the RF spectrum. A consistent peak in the spectrum would imply the presence of an emitter. Upon further processing, features of the emitter, such as frequency, scan rate and pulse width can be extracted [5]. zThese extracted features are typically combined into pulse descriptor word (PDW). These zPDWs can be used to classify or identify emitters. It is important to accurately classify what the transmitter is as this would determine whether an action is taken by the operator. If the ES sensor suite has the ability to estimate the direction of arrival (DoA) of the emitter, then the emitter can be localised through triangulation after intercepting over a span of angles [6]. Localisation of emitters is important as this would help inform an appropriate action for the operator to take. The following sections identify radar parameters which determine the maximum range of the radar system, and analyse the maximum intercept range from an intercept receiver.

2.2.1 Radar Range Equation

The radar range equation is a simple and well known analytical model of a radar system, and is derived in many textbooks, such as [2]. The power received at the radar (expressed in Watts) from a target with a radar cross section (RCS) of σ (expressed in square meters) at range R can be estimated as

$$P_r = \frac{P_t G_t G_r \lambda^2 \sigma L_2}{(4\pi)^3 R^4 L_R}, \tag{2.4}$$

where

- P_t is the transmitted power
- G_t is the gain of the transmit antenna
- G_r is the gain of the receive antenna
- λ is the wavelength of the transmitted waveform
- $L_2 = e^{-2\alpha R}$ and is the two way loss due to atmospheric attenuation, where α is the attenuation coefficient
- L_R is the remaining loss in the radar system (Tx + Rx paths)

This is known as the monostatic radar range equation, and [2] provides an excellent derivation of this. Perhaps a more useful version of this equation is formed when used for estimating received signal to noise ratio (SNR). The noise power of the receiver can be expressed as [7]

$$P_n = kT_0FB, \tag{2.5}$$

where

- k is Boltzmann's constant
- T_0 is the standard temperature (290K)
- F is the receiver noise figure

- B is the receiver instantaneous bandwidth

Thus the input SNR of a single pulse is

$$\text{SNR} = \frac{P_r}{P_n} = \frac{P_t G_t G_r \lambda^2 \sigma}{(4\pi)^3 R^4 L k T_0 F B}, \tag{2.6}$$

To calculate the maximum range of the radar system, first, the radar input sensitivity needs to be defined

$$\delta_{ri} = P_n \times \text{SNR}_{min} = kT_0 FB(\text{SNR}_{min}), \tag{2.7}$$

where SNR_{min} is the minimum input SNR to make a detection. Often it makes greater sense to express sensitivity in terms of the required SNR after applying some processing such as pulse compression or coherent integration gain (from multiple pulses). zThe sensitivity including processing gain, δ_{ro},

$$\begin{aligned} \delta_{ro} &= kT_0 F_i B(\text{SNR}_o) \\ \delta_{ro} &= \delta_{ri} G_p, \end{aligned} \tag{2.8}$$

where G_p is the processing gain and is defined as

$$G_p = \frac{\text{SNR}_o}{\text{SNR}_i} \tag{2.9}$$

Rearranging (2.8), the maximum range of the radar can be calculated to detect a target of RCS of σ

$$R_{max} = \sqrt[4]{\frac{P_t G_t G_r \lambda^2 \sigma}{(4\pi)^3 L \delta_{ro}}} \tag{2.10}$$

2.2.2 Intercept Receiver Range Equation

The power received at the intercept receiver (Figure 2.5) can be estimated through the link budget equation: [8]

$$P_i = \frac{P_t \hat{G}_t G_i \lambda^2 L_1}{(4\pi)^2 R^2 L_i} \tag{2.11}$$

where

- $\hat{G}_t$ is the emitter antenna gain in the direction of the intercept receiver
- G_i is the antenna gain of the intercept receiver
- $L_1 = e^{-\alpha R}$ and is the one way loss due to atmospheric attenuation, where α is the attenuation coefficient
- L_i is the remaining losses in the intercept receiver

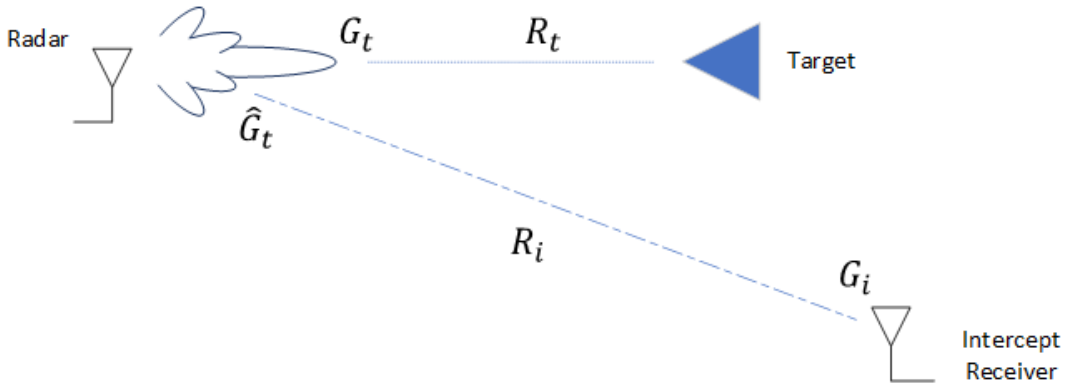

Figure 2.5: Radar and Intercept Diagram

Since the radars received power scales with the inverse of R^4 while the received power at the intercept receiver only scales with R^2, it would be intuitive that the intercept receiver has an easier job of detecting the pulse. However, it is important to note that unless the radar is looking directly at the intercept receiver, the power transmitted in the direction of the receiver is significantly lower than the power transmitted in the direction of the radar's main lobe, i.e. $\hat{G}_t \ll G_t$. In addition, the intercept receiver is at a disadvantage since unlike the radar, it has no knowledge of the radar's location, operating frequency or bandwidth. Thus, in general, wideband antennas with low directivity are required, which results in a low antenna gain. In addition, the intercept receiver requires a large instantaneous bandwidth, which results in a greater sensitivity value (i.e. less sensitive), since the sensitivity of the intercept receiver is

$$\delta_i = kT_0F_iB_i(\text{SNR}_i) \tag{2.12}$$

where

- F_i is the noise figure of the intercept receiver
- B_i is the instantaneous bandwidth
- SNR_i is the minimum SNR for an interception

Similar to the sensitivity of the radar system, it is often useful to express this as a function of the output SNR after some processing gain. However, the ES receiver is far more limited when it comes to processing gain. For example, since it has no prior knowledge of the waveform, no matched filter can be applied. The PRI is also unknown, and thus, coherent or even incoherent integration is difficult. However, a modern digital receiver can generate many parallel narrower band channels - thus decreasing the noise floor in each channel and improving sensitivity [8]

$$\delta_{ro} = kT_0F_iB_o(\text{SNR}_o) \tag{2.13}$$

Thus, the maximum range of an intercept receiver detecting a radar with transmitted power P_t is

$$R_{i\max} = \sqrt{\frac{P_t\hat{G}_tG_i\lambda^2}{(4\pi)^2L_1\delta_i}} \tag{2.14}$$

Unless the intercept receiver has an instantaneous bandwidth that matches the entire operational frequency, the system will have to spectrally search for emitters, i.e. just because the intercept receiver is within the maximum range, interception is not guaranteed. For example, if a system is required to operate with over a 10 GHz bandwidth and the receiver has a 1 GHz instantaneous bandwidth, then each 'dwell' in frequency will only cover 10% of the overall bandwidth. Thus, some kind of frequency sweep or receiver dwell strategy needs to be implemented. While the theory of frequency dwell scheduling is outside the scope of this thesis, it is important to note this limitation.

To summarise, this section has covered the basic operations of a radar and an ES interceptor system and has provided a brief analysis into the factors affecting their maximum range. The following section explores how a radar system designer can exploit these factors to minimise intercept range while maintaining a suitable operating range.

2.3 Low Probability of Intercept Radar

The key task of an LPI radar is 'to see and not be seen' [8]. When comparing the maximum radar and intercept range equations, it is not obvious how one can design a radar system to reduce the maximum intercept range without greatly sacrificing radar range (recall that the power received at the intercept system scales with R^{-2} vs the R^{-4} of the radar). One measure of how 'quiet' a radar is, is to analyse the ratio between the maximum intercept range and maximum radar range. This is derived as [8]

$$\frac{R_{i\max}}{R_{R\max}} = R_{R\max}\left[\frac{\delta_R 4\pi \hat{G}_t G_i G_{pi} L_1}{\delta_i \sigma_T G_t G_R G_{ri} L_2}\right]^{1/2}, \tag{2.15}$$

If $R_{i\max}/R_{R\max} < 1$, then the radar cannot be intercepted beyond its maximum range. From section 2.2, a searching radar will spend most of its time not looking in the direction of the intercept receiver. Thus, we can consider the general case of $\hat{G}_t$ being the mean sidelobe level of the radar. A ratio less than 1 means the radar can operate without being intercepted while it is not scanning in the direction of the interceptor.

Thus, if an LPI radar designer can achieve ultra-low sidelobe levels of the transmitting antenna, then the maximum sidelobe intercept range significantly reduces. The techniques to acheive this are discussed in Section 2.3.1. From (2.15), the radar designer can also design a waveform or dwell pattern that either increases the radar's processing gain, or reduces the interceptor's processing gain. These techniques are discussed in Section 2.3.2

2.3.1 Ultra Low Sidelobe Antenna Design

As discussed previously in this chapter, a scanning radar will not be radiating directly towards the ES receiver for the vast majority of its time - thus, the ES receiver will

be mostly intercepting the radar from its sidelobes. Hence, one of the key ingredients of a low probability of intercept radar is an antenna system which utilises low sidelobe levels. This review is focussed on the area of electronically scanned arrays, rather than mechanically scanned arrays, owing to the operational benefit discussed in Section 2.2.

The far field radiation pattern ($F(\theta)$) of a ULA of spacing d is [8]:

$$F(\theta) = \sum_{n=1}^{N} A_e(\theta)\boldsymbol{A}(n)e^{j\omega\frac{(n-1)d\sin(\theta)}{c}} \tag{2.16}$$

where

- $A_e(\theta)$ is radiation pattern of a single element of the array
- $\boldsymbol{A}(n)$ is the element weighting for element n, where $\boldsymbol{A}$ is the manifold taper vector
  - This quantity is complex for electronic steering (discussed further in Chapter 3). In this Chapter, assume $\boldsymbol{A}$ is a real amplitude vector
- d is the spacing between elements
- N is the total number of elements in the array
- ω is the transmit angular frequency
- c is the speed of light.

Consider a ULA of omnidirectional antennas, i.e. $A_e(\theta) = 1$, then (2.16) simplifies to

$$F(\theta) = \sum_{n=1}^{N} \boldsymbol{A}(n)e^{j\omega\frac{(n-1)d\sin(\theta)}{c}}, \tag{2.17}$$

It is clear that this is an N point DFT of the array taper $\boldsymbol{A}$. As such, this far field radiation pattern has the same 'scalloping' effect in the spectral density estimate as a conventional time-domain Fourier transform. If the array manifold vector is a set of ones, then this is analogous to a rectangular DFT window of length N, and thus, has a peak sidelobe level of around -13 dB. Conventional windows applied to a DFT, such as Hann, Hamming, and Blackman-Harris windows are a well studied problem in signal processing, and it is generally well known that a range of windows can be applied in

order to reduce these sidelobes at the cost of widening the main lobe. Such windows can also be applied to the array taper vector in order to minimise the sidelobes in the radiation pattern, at a cost of broadening the main beam. This is demonstrated in [9], however, the authors only study the peak sidelobe level, without the beam broadening effect. Here, this analysis is extended to consider this. Figure 2.6 shows the normalised radiation pattern of a 20 element ULA spaced at Nyquist (half wavelength spacing) for rectangular, Hann, Hamming and Blackman-Harris windows, and is summarised in Table 2.1.

Table 2.1: Comparison between peak sidelobe levels for popular array manifold vectors

Window	Peak Sidelobe Level (dB)	Beamwidth (degrees)
Rectangular	-13.2	5.44
Hann	-31.5	8.44
Hamming	-38	7.76
Blackman-Harris	-58.2	9.66

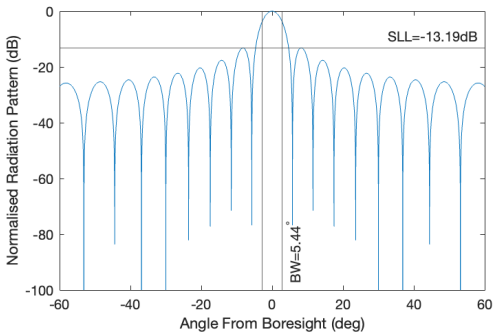

(a) Rectangular window

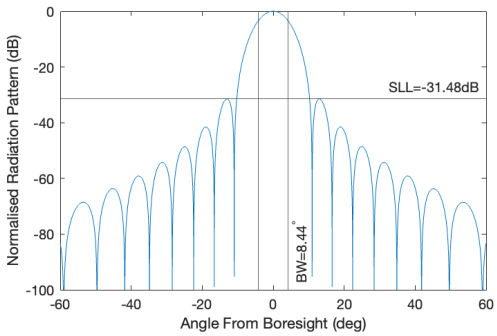

(b) Hann window

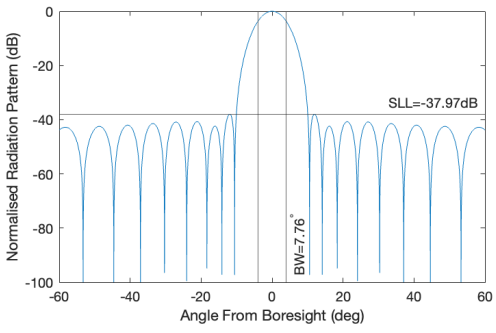

(c) Hamming window

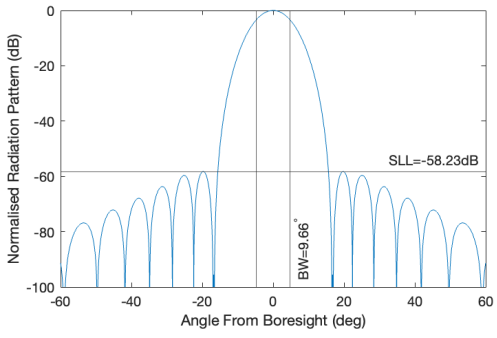

(d) Blackman-Harris window

Figure 2.6: Normalised Radiation Pattern for Selected Windowing Methods

While this analysis only considers the linear array, these windowing techniques can be extended to planar arrays via a 2D window, as discussed in [9].

The Taylor amplitude taper [10,11] is another significant amplitude tapering method worth discussing. The authors aimed to reduce the peak sidelobe levels of a circular array, while maintaining a narrow beamwidth. Unlike the more conventional windows, the maximum sidelobe level and beamwidth are tunable parameters, while the array geometry is a dependent variable. The design process for the Taylor scheme is outside the scope of this thesis, however, [12] provides a good reference of this. In [8], the authors provide examples of the Taylor weighting characteristics and demonstrate how sidelobe levels of up to -50 dB can be achieved. In [13] the authors designed, simulated and experimentally validated an 18 element 24.125 GHz antenna array. The array geometry was synthesised using the aforementioned Taylor weighting and synthesis technique. The paper provides impressive results, and the array produced a sidelobe level of -28.88 dB.

The amplitude weighting methods suggested above are simple to implement as one signal source can drive multiple antennas via variable attenuators or amplifiers. However, modern radars may be fully digital, i.e. each element can be driven by several independent yet synchronised sources - this provides further options for beamforming techniques (as opposed to conventional delay and sum methods). In [14] the authors present a novel LPI beamforming scheme where several low-directional, 'spoiled' beams are transmitted to reduce intercept range. However, the radar's performance remains unchanged as the original high-gain beam can be formed by processing the return from the spoiled beams. Although a lower effective power is radiated per pulse, the radar can maintain its detection performance since the total energy return from the target remains unchanged. The authors quote a 90% reduction in intercept range with this technique. There are many papers proposing LPI beamforming techniques similar to the above technique, where the transmit signal is modulated in both, space and time in order to reduce intercept range, such as [15–17].

2.3.2 LPI Waveform design

Recall that in Section 2.2.2, the wideband receiver was decomposed into narrowband channels via a Fourier Transform to decrease overall noise bandwidth per channel in order to improve the sensitivity in (2.13). However, this logic follows the assumption that the emitter must lie within one frequency bin - this is one area where an LPI radar can exist. For example, if an emitter has a bandwidth that covers two frequency bins, then the noise bandwidth is doubled, reducing the processing gain and thus, increasing (worsening) the sensitivity and decreasing the maximum intercept range. In reality, an emitter may use a spread-spectrum modulation scheme spanning several frequency bins (of the intercept receiver) in order to reduce the sensitivity significantly. The concept of a spread-energy LPI waveform is illustrated in Figure 2.7.

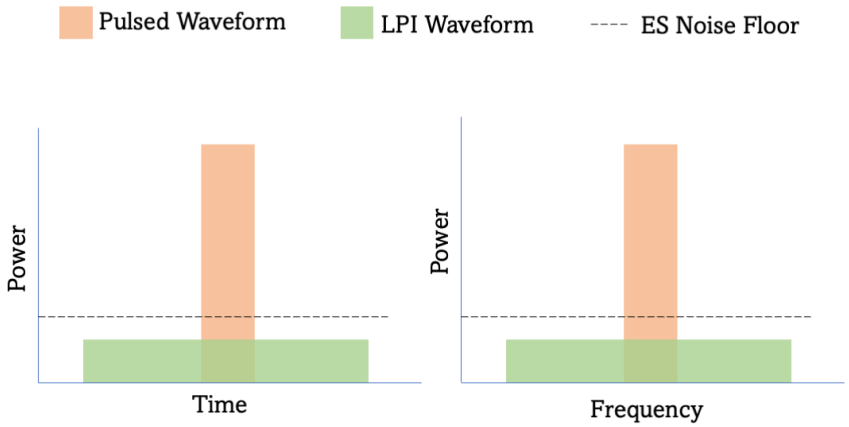

Figure 2.7: Spread Energy vs Conventional Waveform

The key to maintaining good radar range performance for spread energy waveforms is pulse compression [8], where the received signal is correlated with the time-reversed conjugate of the transmitted signal. This stage is also known as a matched filter, and is the optimum filter for received SNR (under the assumption that the noise is additive, white and has Gaussian distribution). The processing gain from this is approximately the time-bandwidth product of the waveform [2].

One such example of an LPI waveform is the linear frequency modulated continuous

wave (LFMCW) waveform. This example waveform is commonly used in literature as a benchmark in LPI radar analysis. An example of an existing LPI radar using such waveforms is the Thales Scout Maritime Radar [18].

Non-linear frequency modulation schemes such as frequency shift keying (FSK) can also possess this LPI property [19]. Certain FSK patterns such as Frank codes [8] are often used in literature for LPI detection analysis. Another common method of spreading the energy of the radar pulse is to apply a phase code (i.e BPSK, M-PSK) to the carrier. Phase coded pulse compression radar is a well studied area [2], and example schemes which possess an LPI property are Frank and polyphase codes [8, 20–22].

Random or noise modulation is another effective method of generating an LPI waveform [23]. A random signal has the added benefit of the interceptor finding it considerably difficult to classify the waveform, even if the waveform is intercepted. However, synthesising a random signal is difficult. Hence, most signals of this type are based on pseudorandom sequences, or generalised as 'chaotic radar signals'. An example of this is presented in [24], wherein the authors propose a method of generating a pseudorandom signal which is band-limited and optimally flat in the frequency domain, providing close to the ideal 'thumbtack' ambiguity function.

2.3.3 Power Optimised Operation

The maximum range of a radar scales with the fourth root of the transmitted power. If a radar is tracking a target at less than maximum range, then transmitting at full power will only increase the probability of it being intercepted. Thus, another method of reducing the probability of a radar being intercepted is to not transmit more power than necessary for the task. This idea can be taken a step further and applied to a network centric approach, or a multi-static system of radars to minimise the power transmitted towards an intercept receiver. A bistatic LPI radar system was demonstrated in [25], and indicates the scalability to multi-static systems.

In [26], the authors propose a resource allocation scheme for a multi-static radar system to meet location accuracy requirements, while minimising the transmit power. In [27], the authors present analysis of transmit scheduling and power allocation in a

cognitive radar network for multiple target tracking and propose optimisation methods for finding an optimal subset of radar systems and their respective transmit power. Minimising the transmit power while still transmitting enough power to meet localisation requirements is a well studied problem, and more analysis and optimisation can be found in [28].

Since the quality of an intercept is dependent on the number of pulses illuminating the receiver, some studies take the idea of minimising transmit power a step further by also minimising dwell times in any particular direction. This in turn minimises the energy at the intercept receiver [29]. zThe approach in [30] presents an optimisation for Tx power and dwell allocation of individual radars in a multi-static radar system. In this paper, spatial diversity through multiple input multiple output (MIMO) radar techniques is exploited, along with using orthogonal waveforms to mitigate cross radar interference. The authors also claim such an approach can reduce probability of interception (POI) by up to 75%.

2.3.4 LPI Radar Summary

The main theme of LPI radar strategies is to minimise the power, or overall energy over a dwell arriving at any potential intercept receiver. Advanced antenna array design and operation can yield ultra low sidelobe levels to reduce the probability of being intercepted from a sidelobe illumination. The waveform itself can be spread in both time and frequency, minimising the (instantaneous) power per unit frequency incident on the intercept receiver, effectively reducing the processing gain applied by the receiver. Intelligent power management can be applied to a network of radar systems, so each system minimises energy towards the intercept receiver.

For the next generation of intercept receivers, the ability to detect such emitters is crucial. The key challenge in this area is to detect, classify and locate weak emissions with a low received SNR, in addition to being able to resolve multiple emitters from different multi-static radar sites.

2.3.5 Detecting & Locating LPI waveforms

A key aspect of an LPI radar waveform is some form of phase or frequency modulation to enable low peak power transmissions. Thus, the signal is no longer stationary as is the case with a conventional waveform, reducing the processing gain of the Fourier transform and therefore, worsening sensitivity. Since the initial processing stage is the deciding factor between further processing of the data window or ignoring it, this is where an LPI emitter exists. Thus, in order to improve the detectability of LPI waveforms, the initial processing stages are of crucial importance. One popular trend for increasing processing gain for such emitters is time-frequency analysis, which can be categorised under short time Fourier Transforms (STFT), Wigner-Ville Distributions(WVD), Choi-Williams Distributions (CWD) and wavelets. A study with comparisons between these techniques can be found in [8] and [31], where examples are presented for several types of LPI waveforms.

In [32], the authors explore the use of STFTs to detect frequency and phase modulated waveforms and conclude that such a technique can detect LPI waveforms at low SNR and provide sufficient detail to extract the modulation features of the waveform. STFTs are also used within [22] whereby the authors propose a STFT for detection and a convolutional neural network for the classification stages. Another example of a novel paper exploiting STFTs for LPI detection and classification is [33]. The authors propose classifying the emitter using visibility graphs and utilising the frequency and phase modulations in order to identify and classify the waveform. While it is difficult to numerically compare the performance of this to deep-learning based methods such as [22], it does suggest that the graph based method is more efficient computationally. Other examples of where the STFT is proposed as a detection stage can be found in [34]. While simple, the STFT approach for time-frequency analysis is not necessarily the most appropriate tool for LPI signal analysis. If data windows are non-overlapping, then it is a strict trade off between time and frequency resolution. Data windows can be overlapped, however this significantly increases computational cost, and can lead to 'smearing' in the time-frequency distribution.

For LFM or FMCW signals, the WVD exhibits a high signal energy concentration in

the time-frequency domain and can provide a processing gain close to that of a radar's matched filter [8]. In [35], the authors propose leveraging the WVD for detection and feature extraction of FMCW and phase coded waveforms and conclude that as a tool, the WVD is good for identifying the modulation characteristics of non stationary signals. However, the authors noted the high computational cost of this, but the key drawback from this method is the existence of 'cross terms', which are manifested as 'ghost signals'. A similar conclusion was presented in [36]. Smoothing in time and frequency is a simple and widely used technique to reduce this effect, and is often cited as the 'smoothed psuedo' Wigner-Ville distribution (PSWVD). There have been multiple studies, such as [37–39], to further suppress these cross terms. Another important variation of the WVD is the Wigner-Ville Hough transform (WVHT), initially proposed in [40]. The classic WVD can provide a high level of processing gain for a linearly frequency modulated waveform, and the Hough transform can be applied to estimate the chirp rate. As such, this is an optimal estimator for a single LFM waveform [41]. However, without further modification, the basic WVHT is suboptimal for multiple simultaneous chirps due to the cross terms present in the WVD. Some efforts to address this have been studied in [42–44], where the authors exploit the periodicity of the LFMCW waveform. In [45], the authors provide an overview of the modified WVHT algorithms for LFMCW signal detection and parameter estimation, and provide analysis into how they could be implemented on an FPGA (Field Programmable Gate Array) for real time processing. [46] was later published by the same authors demonstrating a modified WVHT running in real time on an FPGA, showing a higher level of maturity than many of the other methods considered within this review.

The Choi-Williams Distribution is another key method used for time-frequency analysis within the area of LPI waveform detection and classification. The CWD is largely similar to the conventional WVD, except it uses an exponential weighting kernel to minimise the cross term components that are prevalent in the WVD. The CWD is used as the time-frequency analysis stage of the LPI detection method proposed in [20, 21, 47]. This was shown to have the same processing gain as the WVD, but can handle multiple LFM waveforms due to significant suppression of cross terms.

In [48], the authors noted that while these 'classical' time-frequency analysis methods demonstrated an improvement in detection performance, they had poor resolution in both, time and frequency domains, leading to inaccurate estimates of frequency and time of arrival. The authors propose a novel 'reassignment' technique and present simulation results for FSK pulses demonstrating an increase in parameter estimation accuracy.

To summarise, time-frequency analysis techniques demonstrate a significant increase in processing gain in comparison to conventional windowed FFT (fast Fourier transform) based processing. While the reviewed methods are different, they all function in a similar way by correlating the signal with some time-frequency kernel and measuring the resulting power. In the cases where the kernel exactly matches the modulation of the signal, a processing gain similar to that of the matched filter can be achieved. While these techniques work well for linear frequency modulated signals, they are sub-optimal for phase coded or random waveforms.

Another class of LPI detection strategies are correlation based receivers. Rather than correlating the signal with a known kernel, these techniques correlate the signal received by two or more synchronised sensors, exploiting the fact that the signal 'seen' at the two sensors will have uncorrelated noise, while the LPI signal at the receivers will be highly correlated. In theory, the same pulse compression gain can be achieved as the radar. This technique was proposed in [49]. While analysis was limited to CW sinusoids and binary phase shift keying (BPSK) signals, a significant amount of processing gain was observed. In [50], the authors proposed that a cross correlation technique could be used for time difference of arrival (TDoA) estimates between two elements of a bistatic system for detecting LPI emissions, and concluded that such a technique would work well when one receiver was in the radar's main beam, and another receiver was in the sidelobe (i.e. receiver 2 could not make a detection in isolation). However, the technique proposed in [50] makes the assumption that one of the ES receivers is in the main beam, which, as was addressed earlier in this chapter, was an unlikely scenario for a modern LPI radar. In [51], the authors noted the fact that LFM signals are typically good for synthetic aperture radar (SAR) processing, and exploited the correlation stages of

SAR processing for detection of an LPI emitter, and applied SAR spatial processing in order to locate the emitter.

2.4 Summary

This section has introduced the basic zprinciples of radar and Electronic Surveillance systems, and discussed parameters which define their maximum detection ranges. Of particular interest were parameters which could reduce the maximum detection range of the ES receiver without having too great an impact on the radar's maximum range - this is the basis of low probability of intercept radars. Reviewing modern literature in Section 2.3, we concluded that the radar could minimise the interception range by

- Spreading its energy spectrally to reduce its overall power spectral density
- Reducing sidelobe levels of the transmitting antenna to minimise energy transmitted in the direction of the ES receiver
- Operating in a multistatic geometry
- Minimising transmit power when tracking (while still being able to track)

zThe net result is an overall lower power waveform at the intercept receiver (i.e. low SNR), where its power is spread across a broad bandwidth. Efforts presented in Section 2.3.5 demonstrated some methods of being able to detect and classify LPI radar waveforms. However, these methods mainly focus on temporal processing of such waveforms and using low-gain, wide field of view antennas. From Section 2.2, it can be seen that the maximum range of the intercept receiver can be improved when using a high gain antenna. High gain antennas are highly directional, and are often considered unsuitable for ES receivers due to their low field of view. However, as we will discover in Chapter 3, a full digital array of low directional antennas can form a highly directional high gain beam, and spatial signal processing maintains a wide field of view. In the remainder of this thesis, novel spatio-temporal signal processing algorithms will be applied for the purposes of detecting, and locating low probability of intercept radars.

Chapter 3

Antenna Array Signal Processing

There are three main domains in which sources can differ from one another; space, time and frequency. As mentioned in Chapter 1.4, modern ES receivers can use information from all three domains to characterise an emitter. In Chapters 1 and 2, it was noted that modern transmitters are highly agile in both, the time and frequency domains in order to decrease the probability of an emission being intercepted. This forces a greater emphasis on exploiting the spatial domain to gather key information on RF emissions. Rather than thinking of an antenna array as a number of elements combined in such a way that the beam is steered electronically, this chapter will provide an alternative perspective - a spatial sampler. Combined with digitisation at element level, the problem can now be considered a multi-dimensional (spatio-temporal) signal processing problem. This chapter provides a review of modern state of the art technologies and algorithms in the area of direction finding methods for narrow- and broadband applications. In-depth theory of how electromagnetic waves propagate, and how antennas absorb electromagnetic energy are outside the scope of this chapter, however [1] provides a compressive overview of this. Moreover, this chapter only considers the case of far-field point sources.

3.1 Antenna Array Basics

As opposed to mechanically steering a single high gain (directional) antenna, an alternative approach is to use a combination of omnidirectional antennas to achieve a peak antenna gain in a particular direction through exploiting the concept of superposition. Such an approach has a few advantages, such as faster beam steering, smaller footprint and ease of maintenance due to the lack of mechanical parts. This process of electronic steering is referred to as beamforming and is discussed in Section 3.1.2.

In the far-field region, wavefronts traversing the antenna array can effectively be modelled as plane waves [52]. Figure 3.1 depicts a source at azimuth angle θ, and zero elevation illuminating an N element uniform linear array, with an inter element spacing of d.

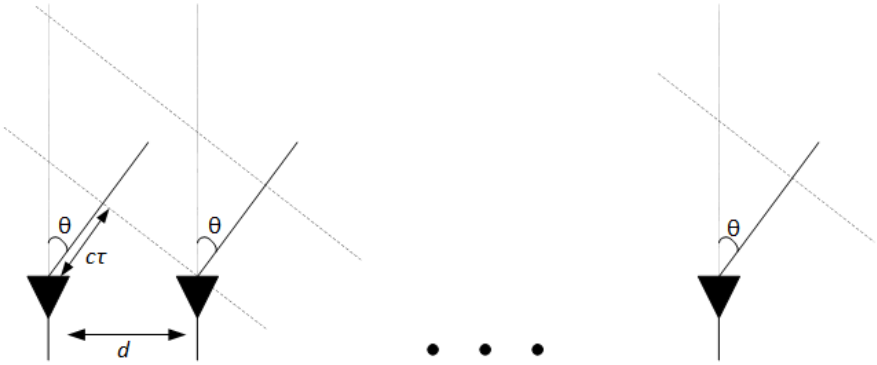

Figure 3.1: Wavefronts from an angle θ illuminating an N element array

The distance the wavefront travels between adjacent elements is $c\tau = d\sin\theta$, and therefore the signal 'seen' between adjacent elements is time delayed by $\tau = (d/c)\sin\theta$. Antenna arrays sample at discrete points in space, as such the Nyquist theorem still applies. Thus to ensure there is no ambiguity with respect to θ, the distance between two elements must be at most half the shortest wavelength expected in the system, i.e. $d \leq \lambda_{min}/2$ [53].

3.1.1 Received Signal Model

Consider the case of L far-field sources illuminating an M element uniform linear array of isotropic antennas, of spacing $d = \lambda/2$, where λ is the wavelength of the sources. This can be modelled as the superposition of L 'steered' sources

$$\boldsymbol{x}(t) = \sum_{l=1}^{L} \begin{bmatrix} s_l(t) \\ s_l(t-\tau_l) \\ \vdots \\ s_l(t-(M-1)\tau_l) \end{bmatrix} + \boldsymbol{\nu}(t) \tag{3.1}$$

where $s_l(t)$ is the l^{th} source illuminating the array, and $\boldsymbol{\nu}$ is the noise vector, which can be assumed to be white, Gaussian, zero-mean, independent and identically distributed (IID) between antennas. Here, τ_l represents the time delay between two adjacent antenna elements for source l, as described in Figure 3.1, and is calculated as

$$\tau_l = \frac{d\sin(\theta_l)}{c} \tag{3.2}$$

where θ_l is the direction of arrival of source l, and c is the wave propagation speed in the medium. In essence, all direction of arrival estimation methods aim to estimate this time delay, τ_l. Further assumptions can be made to simplify this problem. If the source is narrowband, then the complex envelope is approximately constant across the array [53], simplifying the problem to a time shifted sinusoid, i.e. a simple phase shift. Thus, (3.1) can be factored as the source multiplied by some steering vector, $\boldsymbol{a}$.

$$\begin{aligned} \boldsymbol{x}(t) =& \sum_{l=1}^{L} [\boldsymbol{a}_l s_l(t)] + \boldsymbol{\nu}(t) \\ =& \boldsymbol{A}\boldsymbol{s}(t) + \boldsymbol{\nu}(t) \end{aligned} \tag{3.3}$$

where $\boldsymbol{A} = [a_1, a_2, \ldots, a_L]$, and $\boldsymbol{s}(t) = [s_1(t), s_2(t), \ldots, s_L(t)]^T$. By taking the first antenna as a reference, this steering vector can be expressed as

$$a_l = \begin{bmatrix} 1 \\ e^{j\omega\tau_l} \\ e^{j\omega 2\tau_l} \\ \vdots \\ e^{j\omega(M-1)\tau_l} \end{bmatrix} \tag{3.4}$$

Discretely sampling $\boldsymbol{x}(t)$ to $\boldsymbol{x}(n)$, where $t = nT_s$, T_s being the sample period, (3.3) becomes

$$\boldsymbol{x}(n) = \boldsymbol{A}\boldsymbol{s}(n) + \boldsymbol{\nu}(n) \tag{3.5}$$

This simple model will be used to demonstrate advanced array processing concepts throughout the remainder of this chapter.

3.1.2 Beamforming

By exploiting the concept of superposition, the received signals can be delayed (or simply phase shifted in the case of narrowband signals) and summed to achieve a desired antenna gain pattern known as the array factor. In modern applications, two key approaches exist: analog and digital beamforming. Figure 3.2 shows a simple comparison between these two architectures.

The analog beamformer applies these phase shifts (commonly referred to as weights) in the analog domain, combines the analog voltages and then digitises the resulting signal. Such an approach is attractive as the succeeding digital signal processing can be performed at relativity low data rates. There are limitations to this approach as each analog beamforming circuit can only produce one beamformed channel. If we wanted to 'look' in several directions simultaneously, then several parallel analog beamformers will be required, increasing SWAP requirements. In contrast, the digital beamformer does not suffer from this hardware limitation. Since each antenna signal is digitised, several parallel firmware/software streams can 'look' in several directions simultaneously. While this does increase firmware/software complexity, owing to Moore's Law, this is less of an issue, and means future systems can easily be upgraded with only

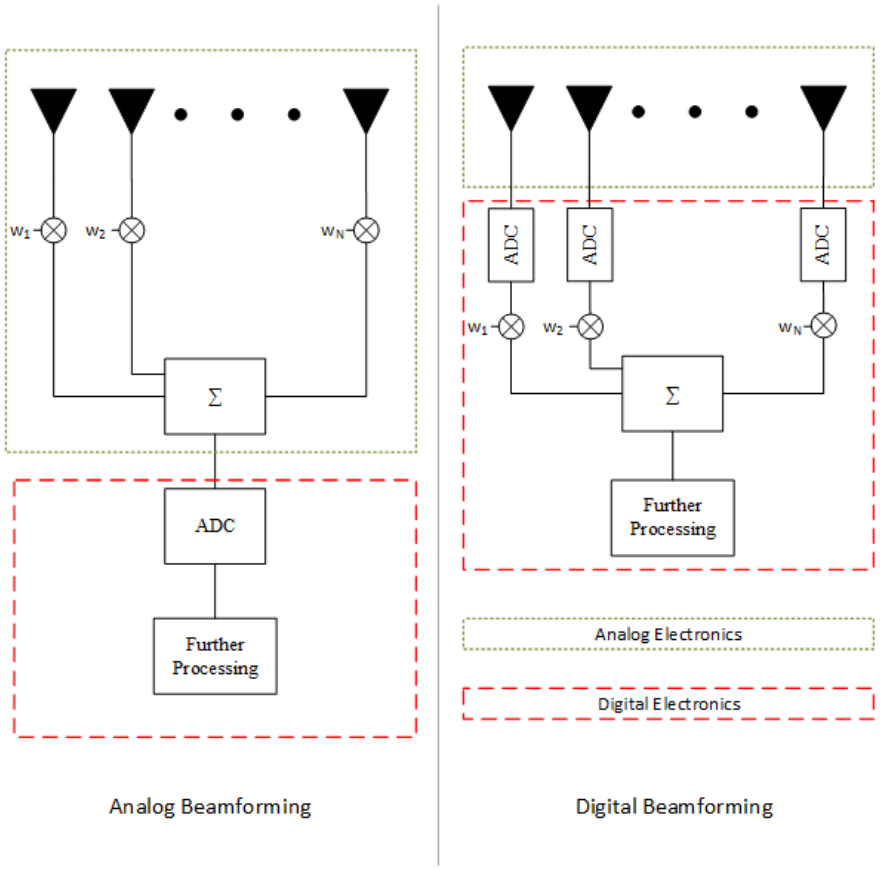

Figure 3.2: Analog and Digital Beamforming Architectures

digital components. In addition, more complex processing can be performed and more sophisticated beamformers can be implemented such as optimal, or adaptive methods [53].

3.1.2.1 Array Factor

The directionality of the beamformed array can be analysed through the calculation of the array factor, analog to the antenna gain pattern on a traditional directional antenna.

By applying complex weights in the architectures shown in figure 3.2, a similar antenna gain pattern can be applied. This antenna gain pattern is known as the array factor, and is calculated as [53]

$$AF(\theta) = \sum_{m=1}^{M} w_m e^{j\omega(m-1)\frac{d}{c}\sin(\theta)} \tag{3.6}$$

where w_m is the complex weight applied to the m^{th} element.

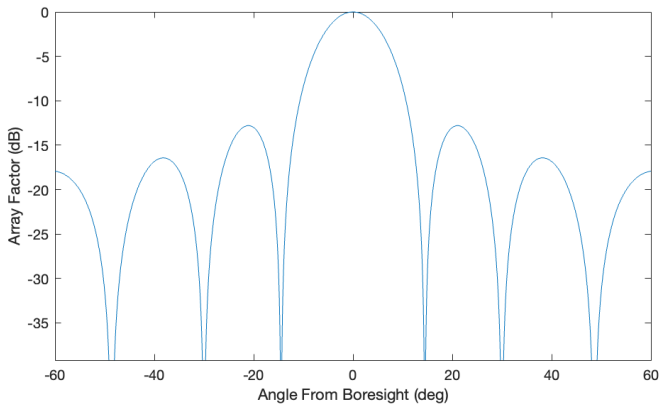

Figure 3.3: Example Array Factor for an $M = 8$ array, steered to 0 degrees

An example array factor can be seen in Figure 3.3, whereby the steering angle is 0 degrees for a Nyquist sampled 8 element ULA.

3.2 Direction Finding Methods

Direction finding is a technique used in many localisation applications. In this section, major advances in the field, and recent state of the art methods are reviewed. For simplicity, only linear arrays will be considered, and the antenna elements are assumed to be perfectly calibrated and isotropic.

Recall the narrowband signal model for a digitised array

$$\boldsymbol{x}(n) = \boldsymbol{A}\boldsymbol{s}(n) + \boldsymbol{\nu}(n) \tag{3.7}$$

where $\boldsymbol{x}(n) \in \mathcal{C}^{M\times 1}$ represents the array signal at discrete time index n, $\boldsymbol{s}(n) \in \mathcal{C}^{L\times 1}$ represents the L source signals, $\boldsymbol{A} \in \mathcal{C}^{M\times L}$ represents the steering matrix, and finally $\boldsymbol{\nu}(n)$ represents the additive noise vector.

To estimate the direction of arrival of all sources, the task is to estimate $\boldsymbol{A}$, which is time independent. Assuming that both $\boldsymbol{s}(n)$ and $\boldsymbol{\nu}(n)$ are zero mean wide sense

stationary (WSS) processes, the time domain statistical properties of these variables can be exploited in order to simplify the problem. Specifically, by estimating the second order moment of $\boldsymbol{x}(n)$, the time domain information essentially compresses into a measure of covariance. Owing to the instantaneous mixture model from (3.7), only instantaneous spatial correlations are of interest. Thus, the $M \times M$ spatial covariance takes the form

$$\boldsymbol{R}_{xx} = E[\boldsymbol{x}(n)\boldsymbol{x}^H(n)] \tag{3.8}$$

The remainder of this section discusses key methods in the area of direction of arrival estimation. This is a non exhaustive list of methods, but it does provide a useful insight into some of the more prevalent and impactful methods in this area.

3.2.1 Beam Scanning

While beamforming itself is seldom used for DoA estimation in modern systems, it provides a foundation that is the basis for the methods used in practice. Consider a basic beamformer where the goal is to measure the variance (power) in a particular direction, θ. This can be done by electronically steering the beam via a multiplication of the steering vector $\boldsymbol{a}(\theta)$, which has the same structure as the steering vector in (3.4). To form a spatial spectrum, this steering vector can be scanned across a range of angles.

$$P_{BF}(\theta) = \boldsymbol{a}^H(\theta)\boldsymbol{R}_{xx}\boldsymbol{a}(\theta) \tag{3.9}$$

Clearly, the resolution of this method is limited by the Rayleigh criterion [52], and can thus only resolve one source within one beamwidth. The remaining methods discussed in this section are deemed as super-resolution owing to the fact that more than one signal can be estimated within one beam-width.

3.2.2 Capon's Minimum Variance

The idea behind Capon's method is to use the nulls of a beamformer as they are typically much sharper than the peaks. Thus, rather than maximising antenna factor

in the direction of the source, minimising output power while forcing the desired signal to remain constant optimises the SNIR. The array weights for the Capon beamformer can be calculated as [54]

$$\boldsymbol{w}(\theta) = \frac{\boldsymbol{R}_{xx}^{-1}\boldsymbol{a}(\theta)}{\boldsymbol{a}^H(\theta)\boldsymbol{R}_{xx}^{-1}\boldsymbol{a}(\theta)} \tag{3.10}$$

Similarly, the DoAs can be estimated through the following heuristic search, θ

$$P_{ca}(\theta) = \frac{1}{\boldsymbol{a}^H(\theta)\boldsymbol{R}_{xx}^{-1}\boldsymbol{a}(\theta)} \tag{3.11}$$

While the Capon beamformer and direction finder can produce impressive results in simulations, [55] noted that such a method is not robust and is sensitive to array imperfections. Another issue with this approach is that because computational complexity of a matrix inversion scales as $O(M^3)$, such an approach may not be feasible for larger arrays operating in real time. While Capon's direction of arrival estimation scheme has mostly been superseded by more advanced methods in recent years, their beamforming scheme still remains incredibly influential. One such extension can be seen in [56], whereby the authors present a method to improve the robustness of Capon's MVDR technique to further optimise the SNIR in the presence of array manifold imperfections, calibration and DoA errors.

3.2.3 MUSIC

The MUSIC (MUltiple SIgnal Classification) algorithm was originally published by Schmidt in 1986 [57], and has grown in popularity in recent years owing to the advancements in receiver and computing technology. The MUSIC idea is similar to Capon's method, but takes it a step further by finding steering vectors orthogonal to a noise subspace of a covariance matrix, rather than its inverse. Consider a scenario whereby a perfect estimate of the spatial covariance is found, it can be expressed as

$$\begin{aligned} \boldsymbol{R}_{xx} &= E[\boldsymbol{x}(n)\boldsymbol{x}^H(n)] \\ &= \boldsymbol{A}E[\boldsymbol{s}(n)\boldsymbol{s}^H(n)]\boldsymbol{A}^H + E[\boldsymbol{\nu}(n)\boldsymbol{\nu}^H(n)] \\ &= \boldsymbol{A}\boldsymbol{R}_{ss}\boldsymbol{A}^H + \sigma_\nu^2\boldsymbol{I} \end{aligned} \tag{3.12}$$

where $\boldsymbol{R}_{ss}$ is the source covariance matrix, and will be diagonal on the condition that all sources are uncorrelated. The eigenvalue decomposition of this spatial covariance matrix

$$\begin{aligned} \boldsymbol{R}_{xx}\boldsymbol{U} &= \boldsymbol{U}\boldsymbol{\Lambda} \\ \boldsymbol{R}_{xx} &= \boldsymbol{U}\boldsymbol{\Lambda}\boldsymbol{U}^H \end{aligned} \tag{3.13}$$

where $\boldsymbol{U}$ and $\boldsymbol{\Lambda}$ represent the eigenvectors and eigenvalues. As the covariance matrix is Hermitian by construction, its eigenvalue matrix will be real and diagonal. It is clear that the number of significant eigenvalues will be the rank of $\boldsymbol{R}_{ss}$ (which will be L providing sources are uncorrelated), and thus, there will be a signal subspace of dimension $\boldsymbol{U}_s \in C^{M\times L}$. As the steering vectors span the signal subspace, it would be intuitive to use the signal subspace to estimate the steering vectors. However, owing to the orthonormality of the eigenvectors, each column of the signal subspace will be orthonormal, while the steering vectors are unlikely to be orthogonal. The steering vectors will however be orthogonal to the noise subspace, $\boldsymbol{U}_n \in C^{M\times(M-L)}$. Thus, the spatial spectrum can be estimated as

$$P_{mu}(\theta) = \frac{1}{\boldsymbol{a}^H(\theta)\boldsymbol{U}_n\boldsymbol{U}_n^H\boldsymbol{a}(\theta)} \tag{3.14}$$

Of course, this method requires the knowledge of the number of signals, L, illuminating the array. This can be estimated from inspection of the eigenvalues. One disadvantage of the MUSIC algorithm is the computational cost of the heuristic search in (3.14). This cannot be overcome with a coarse search as there will be a high risk of completely missing a peak due to the sharpness. This leads to another disadvantage - estimation

accuracy and precision is limited by the search space.

It has been reported that the MUSIC DoA estimator is more robust than Capon's estimator in the case of a poor estimate of the covariance matrix due to insufficient samples and mildly correlated sources [53]. Studies have shown that the MUSIC algorithm is an efficient estimator that lies close to the Cramer Rao Lower Bound [58–60]. There have been many variations and improvements to the MUSIC algorithms since its original publication. Such improvements have mainly focussed on improving computational cost [61–65].

3.2.3.1 Root-MUSIC

The Root-MUSIC algorithm [61] is a popular modification to the MUSIC algorithm which removes the need for the heuristic search operator in (3.14). Recall the steering vector from (3.4) - by exploiting this Vandermonde structure, it can be expressed as

$$a = \left[\begin{array}{c} 1 \\ z \\ z^2 \\ \vdots \\ z^{(M-1)} \end{array}\right] \Bigg| z = e^{j\omega\tau} \tag{3.15}$$

here, τ is the time delay due to DoA, θ. Root-MUSIC reformulates the problem by generating the Laurent polynomial:

$$\begin{aligned} \Gamma &= \boldsymbol{a}^H \boldsymbol{U}_n \boldsymbol{U}_n^H \boldsymbol{a} = 0 \\ &= \boldsymbol{a}^H \boldsymbol{C} \boldsymbol{a} = 0 \\ &= \sum_{n=M-1}^{M+1} c_n z^n \end{aligned} \tag{3.16}$$

where c_n is the sum of the n^{th} diagonal of $\boldsymbol{C}$. Now, the problem is reformulated to finding the roots of Γ. While there are $2(M-1)$ roots of Γ, only the L distinct roots closest to the unit circle are of interest (since $|e^{j\omega\tau}| = 1$). These roots can be translated

into a DoA estimate as

$$\theta_l = \sin^{-1}\left(\frac{c\arg(q_l)}{\omega d}\right) \tag{3.17}$$

where q_l is the root denoting the l^{th} source. It is worth noting that the Root-MUSIC algorithm is an exact solution to the peaks of the MUSIC spectrum. The primary advantage of this method is the reduced computational cost, because finding the roots of a polynomial is less complex than heuristically estimating the spectrum in (3.14) [66]. Another advantage of the Root-MUSIC algorithm over the original MUSIC algorithm is that accuracy is not limited by the scanning granularity, so it can offer a greater degree of precision.

One drawback of the original method in [61] is that it was limited to ULAs. However, manifold separation techniques [67, 68] allow such a method to be used in arbitrary planer array geometries.

Recall that for an M element array, there are $2(M-1)$ roots to the polynomial in (3.17). These roots appear as conjugate reciprocal pairs, and thus, there is a redundancy of factor 2. In [69], the authors propose a method to factorise this polynomial to only produce $M-1$ roots to further improve computational cost in the DoA estimation.

3.2.4 ESPRIT

ESPRIT, originally published in [70] is another method which exploits the Vandermonde structure of a uniform linear array steering vector, and is a search-free estimator to reduce computational complexity. By splitting the ULA into two overlapping sub-arrays of equal size, each will have a Vandermonde structured steering matrix, and will be translational invariant, i.e.

$$\boldsymbol{A}_2 = \boldsymbol{A}_1\Phi \tag{3.18}$$

where $\Phi \in L \times L$ is a diagonal matrix, where the element $\phi_{ll} = e^{j\omega\tau_l}$. Since the steering vector spans the signal subspace, there exists some linear transform matrix, $\boldsymbol{T}$, such that $\boldsymbol{A}_k = \boldsymbol{U}_{sk}\boldsymbol{T}$, for the k^{th} sub-array. Thus,

$$\begin{aligned} \boldsymbol{U}_{s2}T &= \boldsymbol{U}_{s1}\boldsymbol{T}\Phi \\ \boldsymbol{U}_{s2} &= \boldsymbol{U}_{s1}\boldsymbol{T}\Phi\boldsymbol{T}^{-1} \\ \boldsymbol{U}_{s2} &= \boldsymbol{U}_{s1}\Psi \end{aligned} \tag{3.19}$$

where $\Psi = \boldsymbol{T}\Phi\boldsymbol{T}^{-1}$, and can be estimated using a total least squares approach [71]. As Ψ is the linear transform of Φ, they will share the same eigenvalues. Thus the eigenvalues of Ψ contain information of the source's DoA. In a similar fashion to (3.17), the DoAs can be estimated via

$$\theta_l = \sin^{-1}\left(\frac{c\arg(\lambda_l)}{\omega d}\right) \tag{3.20}$$

where λ_l is the l^{th} eigenvalue of Ψ.

3.2.5 DoA estimation of Correlated Sources

Recall that the dimensions of the signal subspace of $\boldsymbol{R}_{xx}$ is defined by the number of its significant eigenvalues, and the number of the significant eigenvalues is determined by the rank of $\boldsymbol{R}_{ss}$. In the case of coherent sources, $\boldsymbol{R}_{ss}$ will be singular. The resulting estimated signal subspace will contain a combination of the steering vectors for the coherent sources, and thus, the true steering vectors will no longer be orthogonal to the noise subspace [72].

One popular method in literature is spatial smoothing. This involves splitting the array manifold into subarrays, then generating covariance matrices for each subarray. Due to the translational invariance of the steering matrix, the averaging of the subarrays effectively shifts energy from the off-diagonals of $\boldsymbol{R}_{ss}$ onto the main diagonal, restoring the rank of $\boldsymbol{R}_{ss}$. This method was initially proposed in [73], and further developed in [72], and is often referred to as 'forward-only' spatial smoothing. While effective at finding the DoA of coherent narrowband sources, this technique is severely detrimental to the effective array aperture.

For P coherent sources illuminating the array, a minimum of 2P antenna elements

are required to find their DoA. This spatial averaging technique was further improved in [74] through averaging in both forward and backward directions. This is known as forward/backward spatial smoothing, whereby the backwards array is defined as the spatially reversed conjugate of the forward. Rather than in terms of DoA estimation performance, the benefits of this approach are in terms of required antenna aperture, with only 3P/2 minimum sensors required. This is further improved in [75], whereby the cross correlation between sub-array elements is taken into account.

3.2.6 Summary on DoA Methods

This section has explored some of the more popular direction of arrival estimation methods cited within the literature. A key element of the super-resolution methods is to form a spatial covariance matrix, under the assumption of a narrowband emitter. Generally, the better the estimate of the covariance matrix, the more accurate the direction of arrival estimate. The methods tend to differ in their computational cost and flexibility. Standard MUSIC and Capon's method can be used on arbitrary array geometries, while Root-MUSIC and ESPRIT are more computationally efficient; they were defined on the assumption of uniformly spaced array elements. Array manifold separation techniques can be applied to combat this, but this further increases computational cost. In the case of correlated sources, the covariance matrix becomes ill-conditioned and can cause these super resolution techniques to fail. However spatial smoothing can be applied to uniform arrays to essentially recondition the covariance matrix and improve performance. The following section will cover non-linear arrays, their importance in a wide band system and state-of-the-art techniques.

3.3 Sparse Arrays

Providing a good estimate of the spatial covariance matrix, $\boldsymbol{R}_{xx}$, the key limiting factor for resolution and accuracy of the DoA estimation is the electrical length of the array (i.e. length of the array in wavelengths). For a ULA, this simply translates into more elements, which may not be practical in many applications. Furthermore, the models

above assume the antenna elements behave in the same manner in an array as when they are in free space. In reality, this may not be the case, and the phenomenon is known as mutual coupling. This is a well studied effect and can be overcome practically through calibration [76–78]. This is, however, computationally expensive. Sparse arrays have been used in astrophysics applications for decades, with the minimum redundancy array proposed in [79, 80]. More recently, sparse arrays have been used in radar [81–83] and for sensing purposes [84, 85].

Consider a set of N sensors placed on a uniform grid of spacing $d = \lambda_{min}/2$, where λ_{min} is the source wavelength. The sensor x_n is physically located at nd from the first sensor in the array. Owing to the wide sense stationary assumption of the data model in (3.3), the spatial covariance, $\boldsymbol{R}_{xx}(i,j) = \boldsymbol{R}_{xx}(i-j,0)$, and is thus solely dependent on the difference between sensor locations i and j. It is intuitive to study the difference set of integers of antenna placement, which can be defined as

$$\mathcal{M} = \{x_i - x_j\}, \forall i,j = 0,1,\ldots,N-1 \tag{3.21}$$

Following the definition of the difference set from [86], repetition of elements is allowed, and will thus contain N^2 elements. The weight function $w(u)$ of an array is defined as the number of times the difference u occurs within its difference set. As an example, Figure 3.5 demonstrates the weight function for an 8 element ULA (displayed in Figure 3.4). If the same difference, u, occurs more than once, i.e. $w(u) > 1$, then it is said to be *redundant*.

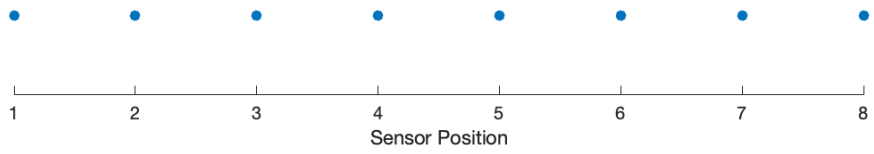

Figure 3.4: Uniform Linear Array - Sensor Positions

From this perspective, the ULA is particularly inefficient in terms of its sensor placement, owing to the redundancy. The remainder of this section discusses key advances in the area of sparse arrays.

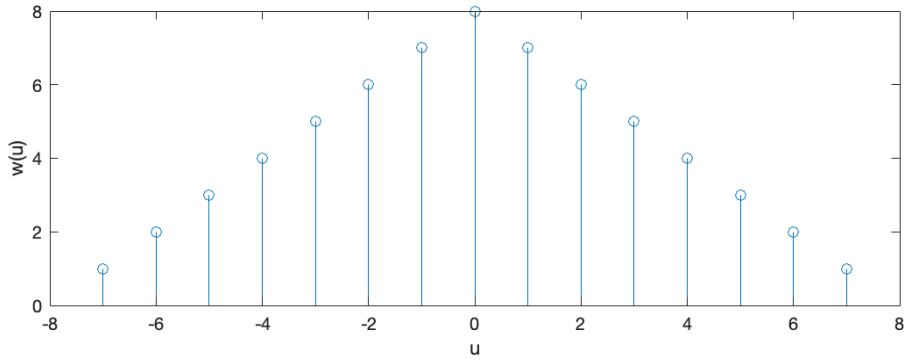

Figure 3.5: Uniform Linear Array - Weight function

3.3.1 Minimum Redundancy Array

A class of linear arrays was shown in [80], which achieves maximum spatial resolution for a given number of elements by minimising the redundancies in the difference set. The case of a zero redundancy array possess a weight function

$$w(u) = \begin{cases} N & \text{for } u = 0 \\ 1 & \text{otherwise} \end{cases} \tag{3.22}$$

While this is the goal of the minimum redundancy array (MRA), such an array does not exist for more than 4 elements [87]. Calculating the sensor locations of a minimum redundancy array is not a trivial task as closed form expressions for estimating sensor locations do not exist. However, look up tables and examples are provided in [80] and some methods can be found in [79]. There are also two subclasses of minimum redundancy arrays: unrestricted and restricted arrays. An example of an 8 element unrestricted and restricted minimum redundancy array can be seen in Figure 3.6, and their weight functions in Figure 3.7.

An unrestricted array optimises sensor placement to achieve the largest possible unbroken region of the weight function, but there are 'holes' past this region, resulting in broken regions in the weight function across the whole aperture. A restricted array on the other hand optimises sensor placement to achieve a hole free weight function across the entire aperture. The latter may be a more suitable option in applications

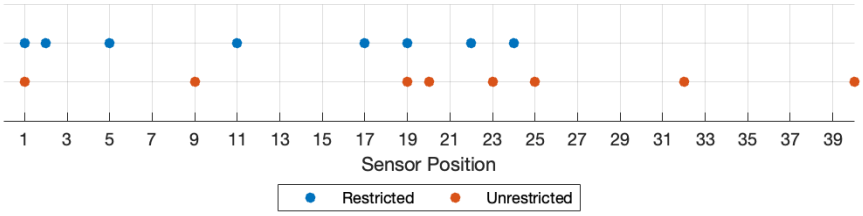

Figure 3.6: Minimum Redundancy Array - Sensor Positions

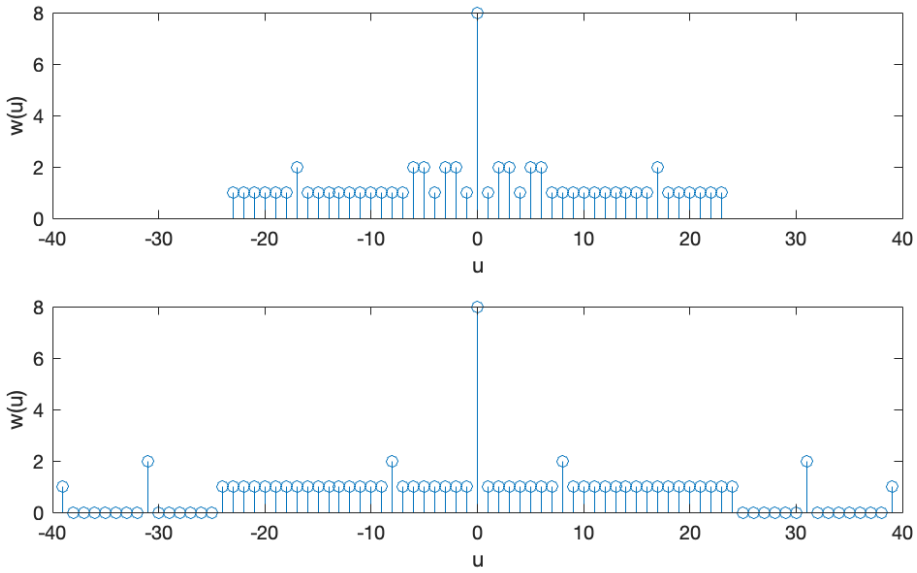

Figure 3.7: Weight functions of a restricted MRA (top), and unrestricted MRA (bottom)

where physical space is a scarce resource since it is more spatially efficient. In the presented 8 element example, the restricted MRA has an array length of $23d$, and a contiguous difference set of $23d$ - thus, all possible differences within the aperture length can be calculated. In contrast, the unrestricted MRA has a slightly larger contiguous difference set length of $24d$, however the physical size of the array is now $39d$, making it considerably larger than that of the restricted class.

3.3.2 Co-Prime Sampling

The temporal co-prime sampler [88] is the union of two uniform samplers, with periods of N_1T_s and N_2T_s, where N_1 and N_2 are co-prime integers and T_s is the Nyquist sampling rate for the system. Since this sampling method can be applied using two uniform ADCs, it is more attractive than sparse sampling methods that require difficult arbitrary clock generation.

The same theory can be applied to array signal processing [89], formed from the union of two uniform arrays; one with N_2 elements spaced at N_1d, and the other with N_1 elements at spacing N_2d. Owing to the co-primality of N_1 and N_2, the samplers only share element 0, and this results in a $N_1 + N_2 - 1$ length linear array. While good for minimising redundancy, this conventional co-prime approach contains holes early within the difference set, limiting its usefulness with certain types of processing, such as spatial smoothing.

The extended co-prime geometry presented in [90] yields an array with a much larger continuous region than the conventional co-prime array. The extended geometry extends the array to contain $2N_2$ elements at spacing N_1, and N_1 elements at spacing N_2. The weight function of an $N_1 = 5$, and $N_2 = 2$ with $N = 2N_2 + N_1 - 1 = 8$ overall elements can be seen in Figure 3.8 and its weight function can be seen in Figure 3.9.

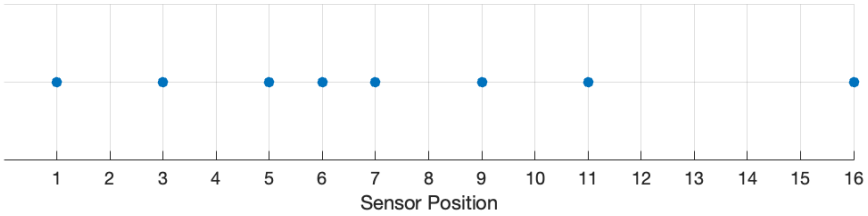

Figure 3.8: Extended Co-Prime Array - Sensor Positions

While efficient in terms of redundancy, the resulting weight function still contains holes and is only continuous in the region $-(N_1N_2 + N_2 - 1)$ to $(N_1N_2 + N_2 - 1)$, and thus, a maximum of $(N_1N_2 + N_2 - 2)$ sources can be resolved using subspace based DoA estimation methods.

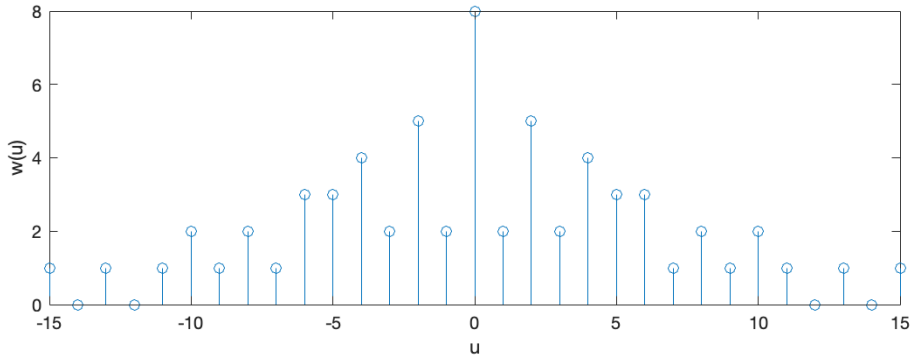

Figure 3.9: Extended Co-Prime Array - Weight function

3.3.3 Nested, and Super Nested Array

Similar to the co-prime array, it is relativity simple to calculate sensor positions for a set number of N sensors (due to the closed form expressions for sensor placement). Again, this array is the union of two ULAs; a Nyquist spaced (d) ULA with N_1 elements, and a sparse ULA of N_2 sensors spaced at $(N_1 + 1)d$, over an aperture of $N_2(N_1 + 1)d$. This yields a sparse array with $N_1 + N_2$ sensors overall, with the ability to resolve $N_2(N_1 + 1) - 1$ sources. An 8 element ($N_1 = N_2 = 4$) nested array is shown in Figure 3.10), and its weight function can be seen in Figure 3.11 (top). Unlike a co-prime array [90], this array yields a contiguous difference set, akin to the restricted class of MRAs. While such an array is easy to design, in general, its weight function contains more redundancies than an MRA. Another major drawback to the conventional nested array is the issue of mutual coupling between sensors of the dense Nyquist portion of the array.

Recently, the super-nested array was proposed in [86, 91]. The super nested array aims to reduce the effect of mutual coupling in the array by redistributing the dense portion of the array across the entire aperture. The goal of the second order super-nested array is to minimise the pairs spaced at Nyquist, i.e. the $w(1) = 1$, which will reduce the effect of mutual coupling substantially, while a third order also minimises the pairs spaced at 2 Nyquist.

Figure 3.10 also shows the sensor locations of an 8 element second order super nested array. It's weight function can also be seen in Figure 3.11 (bottom) and demonstrates

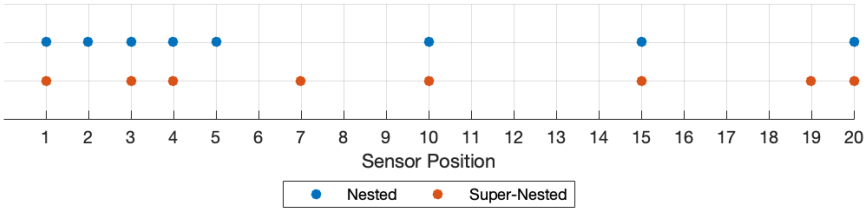

Figure 3.10: Array Element Positions for a Nested, and Second Order Super Nested Array

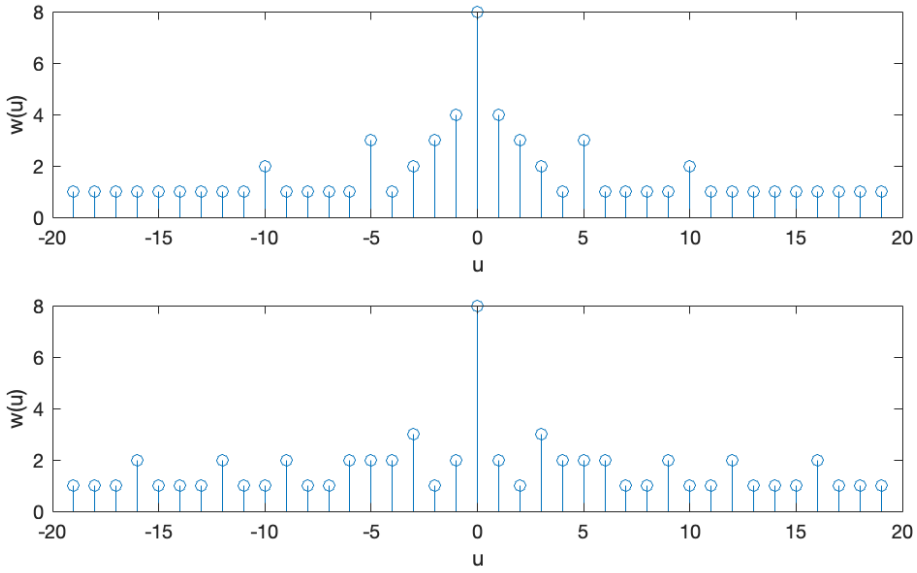

Figure 3.11: Weight functions of a Nested array (top), and a second order super-nested array (bottom)

that while there is the same total redundancy as the conventional nested array, the number of pairs spaced at Nyquist ($u = \pm 1$) is reduced from 4 to 2. Both the nested and second order super nested arrays have the same physical length of $19d$, and the same contiguous region of $19d$ due to the hole free difference set.

3.3.4 Sparse Array Summary

Sparse array geometries provide a wider distribution of sensor placements, increasing the electrical length of an array and offering improved resolution compared to a uniform array of the same number of elements. Figure 3.12 and Table 3.1 provides a comparison

Table 3.1: 8 Element Sparse Array Comparisons

Array	Physical Length	hole-free length
Uniform	$8d$	$8d$
Restricted MRA	$23d$	$23d$
Unrestricted MRA	$39d$	$24d$
Co-Prime	$15d$	$11d$
Nested	$19d$	$19d$
2nd Order Super-Nested	$19d$	$19d$

between the physical locations of the 8-element sparse arrays discussed within this section. x

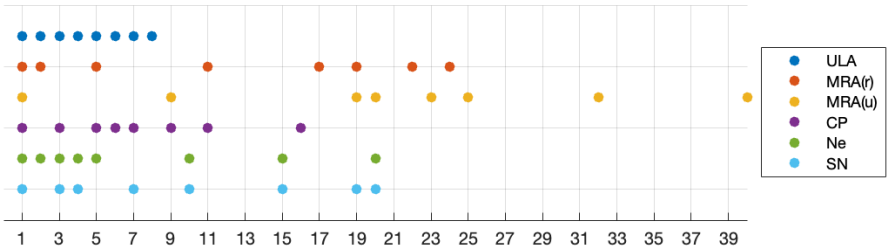

Figure 3.12: Summary of Sparse Array Geometries

Certain processes require a contiguous difference set of the array. Hence, the task of sparse array geometries is to maximise the overall aperture, while maximising the contiguous portion of the difference set, and hence, minimising difference redundancy.

The nested array is perhaps the more intuitive sparse array, as it is the union of a Nyquist sampled linear array (to avoid angle ambiguity), and an under sampled array (to achieve overall aperture). The downfall of such an approach is the significant amount of mutual coupling in the Nyquist section of the array. Super-nested arrays reduce the amount of mutual coupling through redistribution of the closely spaced elements. Co-prime arrays provide less overall redundancy compared to the nested array, but a shorter contiguous region - limiting its usefulness to techniques that do not require this. Finally, the minimum redundancy array is the oldest technique discussed within this review, and provides the greatest overall contiguous aperture. While it is a computationally difficult task of optimising the sensor positions, it is irrelevant from an application perspective as the array geometry stays constant throughout use. It is,

however, the least flexible in determining sensor positions.

3.4 Broadband Array Signal Processing

While the model in (3.1) is valid for a broadband signal, the narrowband approximation used in (3.3) is no longer valid, i.e. the time delay across the array manifold cannot be approximated as a simple phase shift at some centre frequency. Instead, a way to represent this as a linear phase shift across a range of frequencies is required. The obvious approach to this would be to perform a Fourier decomposition on the array signal:

$$\boldsymbol{X}(e^{j\omega}) = \sum_{l=1}^{L}[\boldsymbol{a}_l(e^{j\omega})S_l(e^{j\omega})] + \boldsymbol{\nu}(e^{j\omega}) \tag{3.23}$$

where $\boldsymbol{X}(e^{j\omega})$ and $S(e^{j\omega})$ are the frequency domain representations of the array vector and source signals at angular frequency ω, and $\boldsymbol{a}_l$ is the steering vector for the l^{th} source, and can be represented as

$$\boldsymbol{a}_l(e^{j\omega}) = \begin{bmatrix} 1 \\ e^{j\omega\tau_l} \\ e^{j\omega 2\tau_l} \\ \vdots \\ e^{j\omega(M-1)\tau_l} \end{bmatrix} \tag{3.24}$$

The spatial covariance matrix at frequency ω_k can be formed in (3.25)

$$\begin{aligned} \boldsymbol{R}_{xx}(e^{j\omega_k}) &= E[\boldsymbol{x}(e^{j\omega_k})\boldsymbol{x}^H(e^{j\omega)k})] \\ &= \boldsymbol{A}(e^{j\omega_k})\boldsymbol{R}_{ss}(e^{j\omega_k})\boldsymbol{A}^H(e^{j\omega_k}) + \sigma_\nu^2\boldsymbol{I} \end{aligned} \tag{3.25}$$

Note that the noise is assumed to be white, and is thus independent of frequency. In the case of coloured noise, the noise power term will also be a function of frequency, as is discussed in [92].

Since the covariance matrix at each frequency bin has a similar form to (3.12), all

DoA estimation methods from section 3.2 can be used independently on each frequency bin, and an average of these estimates can result in a final estimate. While simple, such a method has a number of drawbacks - the first being computational complexity. For M frequency bins containing sufficient energy for a signal detection, M parallel DoA estimations are required. On a similar note, if there is insufficient energy in each frequency bin, i.e. the SNR is below a threshold for reliable estimation, this prevents the final estimation from being effective. The effect of spectral leakage should also be considered for this method. Applying an appropriate window function will help mitigate this at the cost of decreased spectral resolution.

3.4.1 Coherent Signal Subspace Methods

One possible approach to overcome some of the issues highlighted above is to no longer process frequency bins independently. The coherent signal subspace method introduced in [92] coherently combines narrowband covariance matrices over a range of frequency bins into a single covariance matrix at some centre frequency, ω_0. The idea behind the coherent signal subspace method is the fact that some transform matrix, T, exists such that

$$\boldsymbol{T}(e^{j\omega_k})\boldsymbol{A}(e^{j\omega_k}) = \boldsymbol{A}(e^{j\omega_0}) \ \forall \ \omega \tag{3.26}$$

i.e. a matrix which focuses a steering vector at one frequency bin, ω_k, onto the chosen centre frequency bin ω_0. The transformed frequency domain data model can be defined as (3.27)

$$\boldsymbol{y}(e^{j\omega_k}) = \boldsymbol{T}(e^{j\omega_k})\boldsymbol{x}(e^{j\omega_k}) \tag{3.27}$$

and the coherently combined covariance matrix can be expressed as (3.28)

$$\hat{\boldsymbol{R}}_{xx}(e^{j\omega_0}) = \sum_{k=1}^{K} w_j E[\boldsymbol{y}(e^{j\omega_k})\boldsymbol{y}^H(e^{j\omega_k})] = \boldsymbol{A}(e^{j\omega_0})[\sum_{k=1}^{K} w_j \boldsymbol{R}_{ss}(e^{j\omega_k})]\boldsymbol{A}^H(e^{j\omega_0}) + \sigma_\nu^2 \sum_{k=1}^{K} w_j \boldsymbol{T}(e^{j\omega_k})\boldsymbol{T}^H(e^{j\omega_k}) \tag{3.28}$$

where w_j is normalised weight for SNR in the j^{th} frequency bin.

In [92], the authors prove that the combined focussed covariance matrix possesses the same eigenspace properties as the narrowband covariance matrix in (3.8). Thus methods presented in Section 3.2 can be used. The authors demonstrate how this 'spectral smoothing' process can resolve coherent sources.

The main difficulty of this method is the generation of the transform matrix, $T(e^{j\omega_k})$. In [92], the authors noted that the solution to satisfy (3.27) is non-unique. As such, many methods have been proposed, e.g. [93–95], to generate this matrix. However, these methods require knowledge of the source's DoA, and the overall performance is dictated by how accurate these initial estimates are. The suggestion from [92] was to perform a course DoA estimate to get this initial estimate, then a fine DoA estimate to super-resolve closely spaced sources.

The requirement of a preliminary estimate of the source's DoA in order to achieve a better estimate in either accuracy or resolution is an obvious downside. However, in [96], a new method was presented which did not require a preliminary DoA estimate, through the use of a set of auto-focussing matrices. The authors identified that the signal subspace eigenvectors span the same subspace as the steering vectors at each frequency. Rather than using a preliminary estimate of the steering vectors to form the focussing matrices, their eigenvectors can be used instead, i.e. the auto-focussing matrices can be generated as

$$\boldsymbol{T}(e^{j\omega_k}) = \frac{1}{\sqrt{K}}\boldsymbol{U}(e^{j\omega_0})\boldsymbol{U}^H(e^{j\omega_k}) \tag{3.29}$$

where K is the number of frequency bins to coherently combine covariance matrices.

This transform matrix can be used in (3.28) to form the combined covariance matrix.

However, such a method cannot resolve coherent, or strongly correlated sources even though the same 'spectral smoothing' process is used as in [92]. In the case of coherent sources, the source covariance matrix will be singular, and thus the signal eigenvectors will no longer share the same span as the steering vectors due to the same reasons mentioned in Section 3.2.5.

3.4.2 Polynomial Matrix Methods

Polynomial matrices are a fairly recent advancement in the area of broadband array signal processing, and have been applied for direction finding, beamforming, and MIMO systems [97–102]. One of the issues with the frequency domain methods is that each Fourier component is treated independently, and thus ignores small yet important correlations between spectral components. A key aspect of polynomial matrices is that rather than performing a Fourier decomposition on the array signal, (3.1) can be expressed as the following convolutive mixture model

$$\boldsymbol{x}(t) = \sum_{l=1}^{L} \begin{bmatrix} s_l(t) \\ s_l(t) \otimes \delta[t-\tau_l] \\ \vdots \\ s_l(t) \otimes \delta[t-(N-1)\tau_l] \end{bmatrix} + \boldsymbol{\nu}(t) \tag{3.30}$$

where $\delta(t)$ is the Dirac-delta function. Similar to (3.3), this can be decoupled to a convolution of a source and its steering vector

$$\begin{aligned} \boldsymbol{x}(t) =& \sum_{l=1}^{L} [a_l \otimes s_l(t)] + \boldsymbol{\nu}(t) \\ =& \boldsymbol{A} \otimes \boldsymbol{s}(t) + \boldsymbol{\nu}(t) \end{aligned} \tag{3.31}$$

where

$$a_l = \begin{bmatrix} 1 \\ \delta[t-\tau_l] \\ \delta[t-2\tau_l] \\ \vdots \\ \delta[t-(N-1)\tau_l] \end{bmatrix} \tag{3.32}$$

and $\boldsymbol{A} = [a_1, a_2, \ldots, a_L]$.

The motivation behind polynomial matrices lies within the convolutive mixture model in (3.31), i.e. unlike the narrowband scenario, it is now appropriate to consider a range of temporal correlations in addition to spatial correlations. The spatial covariance matrix at discrete temporal lag, k, is

$$\boldsymbol{R}_{xx}(k) = E[\boldsymbol{x}(n)\boldsymbol{x}^H(n-k)] \tag{3.33}$$

and thus the polynomial space-time covariance matrix is calculated as the power series

$$\boldsymbol{R}_{xx}(z) = \sum_{k=-W}^{W} \boldsymbol{R}_{xx}(k) z^{-k} \tag{3.34}$$

where W should be chosen such that $\boldsymbol{R}_{xx}(k)$ is a zero matrix beyond $k > |W|$, which can be determined experimentally.

The parahermitian operator (denoted by the superscript P) of a polynomial matrix is defined as the time-reversed conjugate transpose, and a matrix is said to possess the parahermitian property if the original matrix is equal to its parahermitian transpose. Likewise, a paraunitary matrix is a polynomial matrix which when multiplied with its parahermitian is an identity matrix.

Now, by construction, the space-time covariance matrix of (3.34) has this parahermitian property, i.e.

$$\boldsymbol{R}_{xx}(z) = \boldsymbol{R}_{xx}^P(z) = \boldsymbol{R}_{xx}^H(z^{-1}) \tag{3.35}$$

In a similar fashion to (3.12), this space-time covariance matrix may also be expressed as

$$\boldsymbol{R}_{xx}(z) = \boldsymbol{A}(z)\boldsymbol{R}_{ss}(z)\boldsymbol{A}^P(z) + \sigma_\nu^2\boldsymbol{I} \tag{3.36}$$

In [103], the authors proposed the sequential best rotation algorithm (SBR2) for the eigenvalue decomposition of parahermitian matrices. This is a generalisation of the Jacobi algorithm for eigenvalue decomposition of a Hermitian matrix and it provides a diagonalisation of a polynomial matrix via a paraunitary similarity transform. Since its publication, variants of the polynomial eigenvalue decomposition (PEVD) have been formed, such as sequential matrix diagonalisation (SMD) [104] methods, which provide a faster convergence, but at a greater overall computational cost. There have been several evolutions to this method such as the maximum energy SMD (ME-SMD) [105], where each iteration is optimised for shifting the most energy from the off-diagonals per iteration. While computationally expensive, this method formed part of the framework that other PEVD methods are compared against. In order to reduce the computational cost of this, the authors in [106, 107] propose a restricted update SMD (RU-SMD) algorithm, which reduces computational complexity with little effect on performance. Such algorithms have been further improved and matured for deployment on an FPGA for real time computation [108–111].

Using methods described above, it is possible to decouple the space-time covariance matrix into polynomial eigenvalues and paraunitary eigenvectors.

$$\boldsymbol{R}_{xx}(z) \approx \boldsymbol{U}(z)\boldsymbol{\Lambda}(z)\boldsymbol{U}^P(z) \tag{3.37}$$

whereby the polynomial eigenvectors possess the paraunitary property, $\boldsymbol{U}(z)\boldsymbol{U}^P(z) = \boldsymbol{U}^P(z)\boldsymbol{U}(z) = I$. The eigenvalues represent a power spectral density

$$\boldsymbol{\Lambda}(\omega) = \left.\begin{bmatrix} \lambda_1(z) & & & \\ & \lambda_2(z) & & \\ & & \ddots & \\ & & & \lambda_M(z) \end{bmatrix}\right|_{z=e^{j\omega}} \tag{3.38}$$

and are spectrally majorised such that $|\lambda_1(\omega)| > |\lambda_2(\omega)| > \ldots > |\lambda_M(\omega)|$. From (3.36),

it is clear that the number of significant eigenvalues, and thus the dimensions of the signal subspace will be the rank of $\boldsymbol{R}_{ss}$, which will be equal to the number of sources illuminating the array. This can thus be separated into signal and noise subspaces

$$\boldsymbol{R}_{xx}(z) \approx \begin{bmatrix} \boldsymbol{U}_s(z) & \boldsymbol{U}_n(z) \end{bmatrix} \begin{bmatrix} \boldsymbol{\Lambda}_s(z) & \\ & \boldsymbol{\Lambda}_\nu(z) \end{bmatrix} \begin{bmatrix} \boldsymbol{U}_s^P(z) \\ \boldsymbol{U}_n^P(z) \end{bmatrix} \tag{3.39}$$

It is clear that the eigenvectors related to the signal subspace, $\boldsymbol{U}_s$, contain information of the steering matrix, $\boldsymbol{A}$. However, the columns of $\boldsymbol{U}_s$ will be orthonormal, whereas the columns of the true steering matrix may not be. The columns of the true steering matrix, however, will be orthonormal to the noise subspace.

Using this rationale, the authors in [97] extended the MUSIC algorithm to broadband scenarios using these polynomial matrix methods, and thus the spatio-spectral Polynomial MUSIC (PMUSIC) algorithm (3.40)

$$P_{mu}(\theta, \omega) = \left. \frac{1}{\boldsymbol{a}^P(\theta, z)\boldsymbol{U}_n(z)\boldsymbol{U}_n^P(z)\boldsymbol{a}(\theta, z)} \right|_{z = e^{j\omega}} \tag{3.40}$$

where $\boldsymbol{a}(\theta, z)$ is the test polynomial steering vector for DoA, θ. The elements of model steering vectors in (3.32) are ideal fractional delay filters that can only be realised, for discretely sampled signals, by band limiting to the Nyquist frequency. Such limiting produces a sinc function as the closest approximation to the Dirac delta function. However, such a filter is both non-causal and of infinite length making direct implementation impractical. Methods on approximating such a fractional delay filter are discussed in Section 3.4.2.1

3.4.2.1 Fractional Delay Filters

The most basic implementation of the fractional delay filter is a simple truncated sinc,

$$a_i(n) = \text{sinc}(n - \hat{\tau}), \quad n \in [-N_s, N_s] \tag{3.41}$$

where $\hat{\tau}$ is the fractional delay in samples, and n is the sample index. Thus this FIR

filter contains $2N_s + 1$ elements. Two issues exist with this basic sinc based fractional delay filter the first being the ripples in the pass band, which can be overcome with appropriate windowing functions. The second issue is that the sinc filter becomes band limited if truncated, causing a sharp null towards the Nyquist frequency.

The Farrow structure is another well known method for inducing a fractional delay [112,113]. The main feature of the Farrow structure is that the sub-filter coefficients are fixed, while the fractional delay can be continuously tuned. This provides an attractive solution for a broadband steering vector for the PMUSIC algorithm in (3.40) as it eliminates the need for generating a new set of fractional delay filters for the steering vector at each scan of the spatio-spectrum. This method, however, still suffers from an increased approximation error at higher frequencies.

A novel method of inducing a fractional delay through the use of filter banks was introduced in [114], and provides a comparison between the three methods discussed so far. The idea behind this method is that the approximation error of the Farrow structure is proportional with increasing frequency. By decomposing a signal into P sub-bands, down-converting to a lower frequency, applying P parallel fractional delay FIR filters on each band, followed by a reconstruction, a nearly flat approximation error can be achieved throughout the entire band. Obviously, such an approach will increase computational cost P-fold.

3.5 Chapter Summary

This Chapter has provided a review of existing techniques, methods and literature surrounding spatial signal processing for antenna arrays. The concept of a digital antenna array has been introduced, and thus, a signal model for the narrowband scenario has been derived.

A common element of the DoA estimation algorithms discussed in Section 3.2 is to approximate the scenario using the narrowband assumption. This yields an instantaneous mixing model and therefore, direction information can be estimated purely from the spatial domain. Hence, a key processing stage is to form a covariance matrix of spatial only correlations. However, as discovered in Chapter 2, modern LPI emit-

ters utilise a broadband modulation scheme, invalidating the narrowband assumption conventional super-resolution algorithms are based upon.

Section 3.3 provided an overview of sparse array geometries and some techniques such as the virtual array to exploit the properties of sparse arrays. These techniques also rely on the narrowband assumption to work effectively. Most literature surrounding sparse arrays is primarily focussed on the narrowband case. It is apparent, however, that such geometries pose as attractive solutions for broadband scenarios. A wide band receiving system requires fine spacing for ambiguity free DoA estimates at higher frequencies, and a wide overall aperture for sufficient resolution at the lower frequencies. This is explored further in Chapter 6.

Finally, Section 3.4, presented a review of literature of broadband spatial signal processing techniques. Independent frequency bin processing is an intuitive approach to take. However by assuming all frequency bins are independent, important correlations between bins are ignored, making this technique suboptimal in terms of performance. Independent frequency bin techniques are also computationally expensive since parallel independent narrowband computations are required, e.g. if a signal spans N frequency bins, then N covariance matrices would need to be estimated, and then providing a final DoA estimate via averaging the extracted DoA from each of these matrices. In contrast, coherent signal subspace methods focus these N covariance matrices into a single covariance matrix, and then apply conventional DoA estimation techniques to this focussed matrix. However, in order to effectively focus these covariance matrices, some prior knowledge of DoA is required, adding a course, then fine DoA estimation stage. To combat this issue, a category of auto-focussing coherent signal processing methods was proposed, omitting the need for the coarse DoA estimation stage.

Polynomial matrices are a recent invention in the area of broadband signal processing. These do not require a DFT for the initial processing stages, and instead a space-time covariance is calculated containing all spatial and a range of temporal correlations. The significance of this is that there are no errors induced by the DFT, and a similar processing gain is induced via auto- and cross correlations. One of the key advances in this area are the Polynomial Eigenvalue Decomposition algorithms,

which allow the generation of signal and noise subspaces, thus enabling the existence of spatio-temporal algorithms like the Polynomial MUSIC algorithm.

Chapter 4

The Multi-Correlation Receiver & Polynomial Matrices

4.1 Introduction

The previous chapters have shown that traditional narrow-band approaches are inadequate for the separation and localisation of modern radar sources. However, recent development of polynomial matrix methods show promise as the basis for developing more appropriate approaches.

The novel contribution of this chapter is the exploitation of the spatial domain via polynomial matrix methods, as it explores how these methods can be used in a passive sensing scenario for the detection and direction estimation for LPI emissions. In this chapter (particularly in Section 4.2), the motivation behind the multi-correlation receiver will be explored. It will be identified that time and frequency domain based approaches alone are insufficient for the detection of low power LPI emissions in low SNR scenarios. This section will also discuss how such emissions can be detected by considering spatial and temporal correlations through the formation of a space-time covariance matrix with just 2 elements.

In Section 4.3, the idea from Section 4.2 is generalised to an arbitrary number of array elements, and a description is formed on a broadband steering vector. This model includes a down-conversion stage, which is typically not included in most literature.

This data model is used for all broadband analysis contained within this chapter and Chapter 6.

Section 4.4, discusses the space-time covariance matrix, including how it can be analytically modelled, or formed through data. This section also describes how polynomial eigenvalues can be exploited for detection purposes. In Section 4.5, a novel algorithm is introduced to significantly decrease the computational cost of the Polynomial MUSIC algorithm. Finally in Section 4.6, a series of simulations are presented to analyse the results of the algorithms presented throughout this chapter.

4.2 The Motivation Behind the Correlation Based Receiver

Before analysing complex polynomial matrices, in this section we explore the idea of using a cross correlation and subsequently a cross spectral density estimate to enhance detection of a broadband signal in a low SNR scenario.

First, consider the simple case of a two element receiver with only receiver noise present. The signal at the receiver can be modelled as

$$\boldsymbol{x}(n) = \begin{bmatrix} x_1(n) \\ x_2(n) \end{bmatrix} = \begin{bmatrix} \nu_1(n) \\ \nu_2(n) \end{bmatrix} \tag{4.1}$$

where ν_1 and ν_2 are uncorrelated i.i.d zero mean Gaussian noise terms. Assuming $\boldsymbol{x}(n)$ is a wide sense stationary signal the auto ($i = j$) and cross ($i \neq j$) correlation terms are defined as

$$r_{i,j}(\tau) = E[x_i(n)x_j^*(n-\tau)] = E[\nu_i(n)\nu_j^*(n-\tau)] \tag{4.2}$$

Since the noise is uncorrelated, the cross correlation sequence will be zeros

$$r_{ij}(\tau) = 0 \ \ \forall \ \ \tau, \ i \neq j \tag{4.3}$$

and the auto correlation will resemble a Kronecker-Delta function, where the peak is

the noise variance

$$r_{ii}(\tau) = \begin{cases} \sigma_\nu^2, & \tau = 0 \\ 0, & \text{otherwise} \end{cases} \tag{4.4}$$

In reality, these correlation terms will be estimated with a finite number of samples, and the signal bandwidth is assumed to be less than the sampling rate. Thus, the auto correlation term will not be a perfect Kronecker impulse, and the estimate of the cross correlation sequence will not be exactly zero. The premise behind the correlation based detector is that if there is a signal present:

1. The estimation of the cross correlation sequence will not be a sequence of approximately zeros, and will have a peak at some time lag index

2. The estimation of the autocorrelation function will not be a Dirac impulse, but instead a sinc function (unless the signal bandwidth exactly matches the sampling rate)

As a reference, consider the scenario of a two element receiver system with only receiver noise present. The noise power (σ_ν^2), and the noise at each receiver is i.i.d. and 600 samples are acquired.

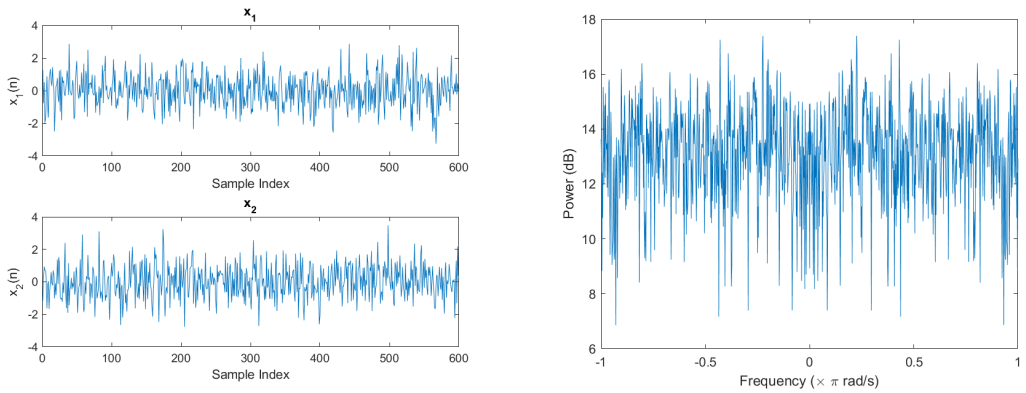

(a) Time domain plots of receiver noise on both channels

(b) Frequency domain plot of combined receiver noise

Figure 4.1: Receiver Noise Only Scenario

At this stage, a conventional approach to detect a signal would be to incoherently combine their FFT outputs. As expected, since these waveforms are simply uncorrelated noise, no obvious temporal or spectral structure can be seen in Figure 4.1.

$$X(\omega) = \frac{1}{N}(\text{FFT}(x_1(n)) + \text{FFT}(x_2(n))) \tag{4.5}$$

The autocorrelation of sensor 1 (r_{11}) and the cross correlation sequence (r_{12}) can be seen in Figure 4.2.

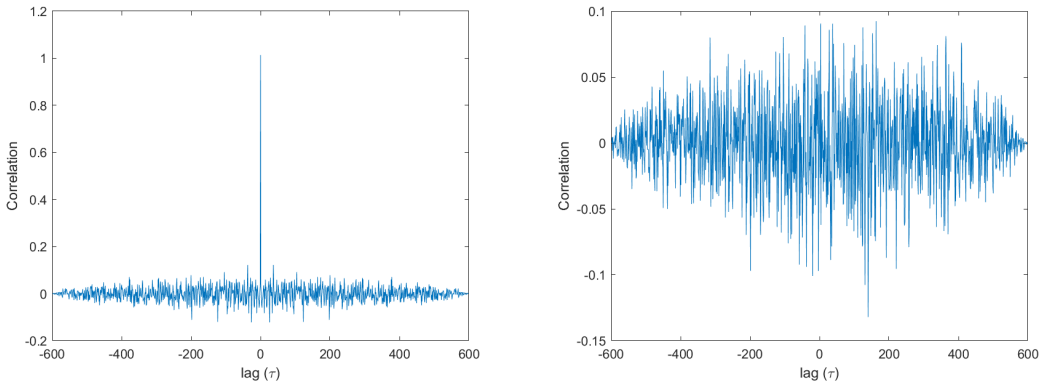

(a) Autocorrelation sequence of sensor 1 (b) Cross correlation sequence between sensors

Figure 4.2: Correlation Sequences of Receiver Noise

As expected from receiver noise only, there is a peak of approximately σ_ν^2 at the lag of $\tau = 0$, and no significant peaks can be seen in the cross-correlation term. This analysis combined with Figure 4.1 can conclude that there is no common signal illuminating both antennas simultaneously.

Now, consider a 200 sample long wideband pulse of bandwidth π rad/s. Here, the samples are randomly selected from a zero mean Gaussian pdf with variance of 1, and passed through a low pass FIR filter to force a normalised bandwidth to π rad/s. This signal is seen at both antennas, and there is a delay of four samples on the second channel. Thus the received signal can be modelled as

$$\boldsymbol{x}(n) = \begin{bmatrix} x_1(n) \\ x_2(n) \end{bmatrix} = \begin{bmatrix} s(n) \\ s(n-4) \end{bmatrix} \tag{4.6}$$

A time and frequency domain representation of this waveform can be seen in Figure 4.3.

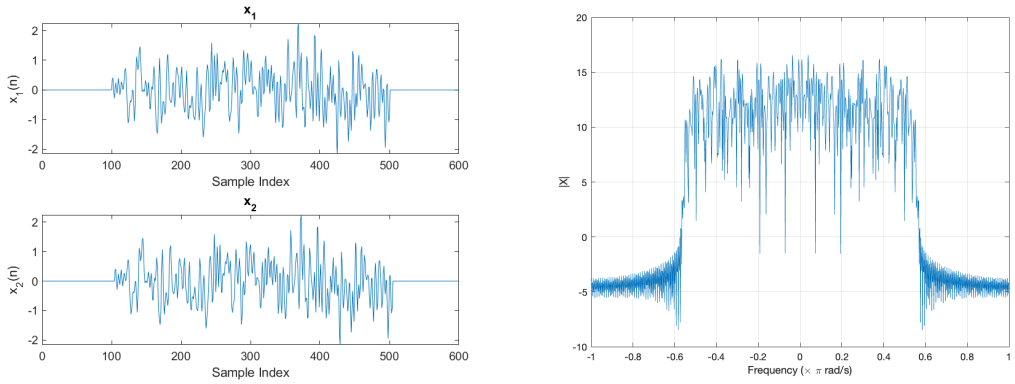

(a) Time domain plots of filtered Gaussian uncorrelated pulse

(b) Combined frequency domain plot of filtered Gaussian uncorrelated pulse

Figure 4.3: Time and Frequency Plots of the filtered Gaussian uncorrelated pulse

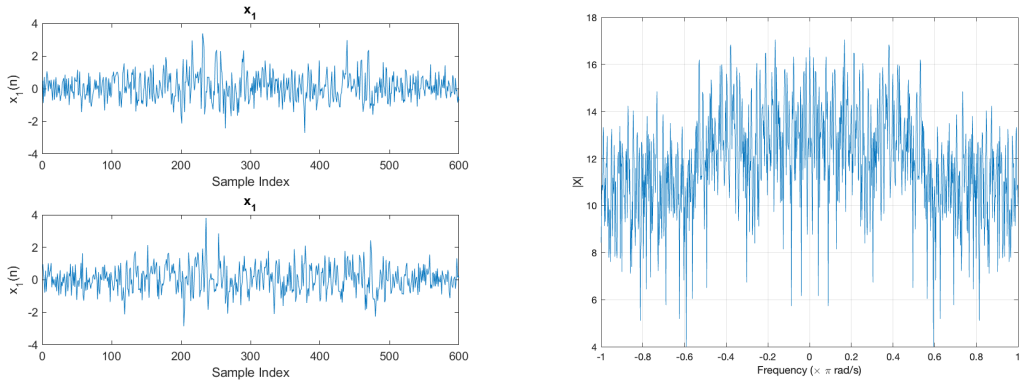

(a) Time domain plots of filtered Gaussian uncorrelated pulse plus receiver noise

(b) Combined frequency domain plot of filtered Gaussian uncorrelated pulse plus receiver noise

Figure 4.4: Time and Frequency Plots of Filtered Gaussian Uncorrelated Pulse plus receiver noise (0dB SNR)

White Gaussian noise is added, and in this scenario the SNR is set 0 dB (i.e. same signal and noise power). The noisy version of the signal in (4.6) is now defined in (4.7)

$$\boldsymbol{x}(n) = \begin{bmatrix} x_1(n) \\ x_2(n) \end{bmatrix} = \begin{bmatrix} s(n) \\ s(n-4) \end{bmatrix} + \begin{bmatrix} \nu_1(n) \\ \nu_2(n) \end{bmatrix} \tag{4.7}$$

and the time and frequency domain can be seen in Figure 4.4

In the time domain, there is no obvious rising edge of the pulse. Calculating the spectral representation in the same way as (4.5), a processing gain of $\sqrt{2}$ is expected since there are two channels. However, the resulting frequency estimation shows no rise in power at any particular frequencies. Thus, at this stage a conventional FFT style ES system would incorrectly determine that there is no emitter present in this dataset. However, when the auto- and cross correlation terms are considered in Figure 4.5, it does provide an indication of a common signal across both receivers.

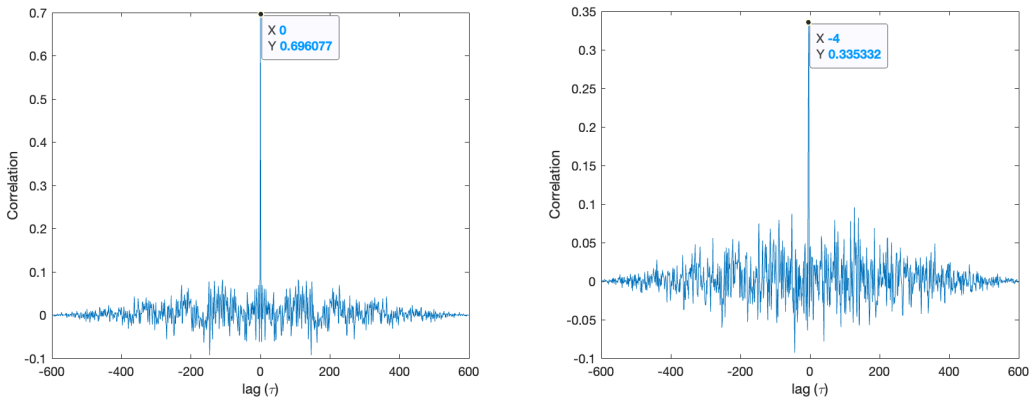

(a) Autocorrelation sequence of sensor 1 (b) Cross correlation between sensors

Figure 4.5: Correlation Sequences for the Noise Pulse plus Receiver Noise Scenario (0 dB SNR)

While the auto correlation looks similar to that in Figure 4.2, the cross correlation has a significant peak at $\tau = -4$, which is clearly indicative of some common signal present on both receivers.

The above example has only considered the auto correlation of sensor 1 ($r_{11}(\tau)$), and the cross correlation between sensors 1 and 2 ($r_{12}(\tau)$). The autocorrelation of sensor 2 ($r_{22}(\tau)$), and the cross correlation of 2 and 1 ($r_{21}(\tau)$) can also be considered. It is thus convenient to express this as a space-time covariance matrix (4.8)

$$\mathbf{R}_{\mathbf{xx}}(\tau) = E[\boldsymbol{x}(n)\boldsymbol{x}^H(n-\tau)], \tag{4.8}$$

and can be estimated over a finite number of samples via temporal averaging (under

the assumption that $\boldsymbol{x}(n)$ is WSS)

$$\mathbf{R}_{\mathbf{xx}}(\tau) \approx \frac{1}{N}\sum_{n=1}^{N} \boldsymbol{x}(n)\boldsymbol{x}^{H}(n-\tau) \tag{4.9}$$

This matrix is now plotted in Figure 4.6.

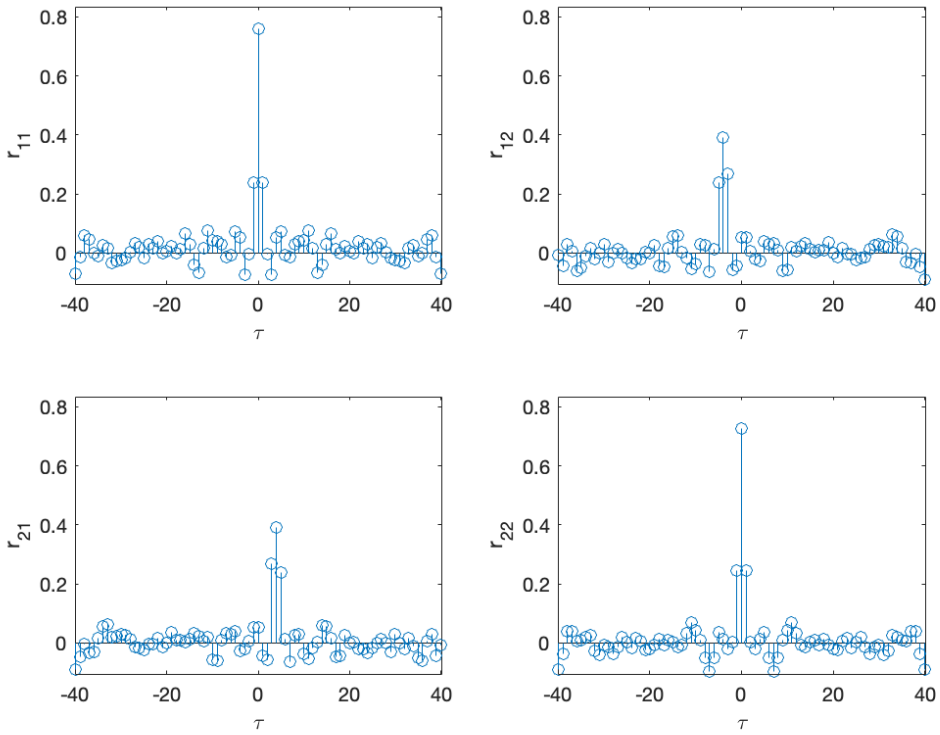

Figure 4.6: Space-Time Covariance Matrix

This can be analysed in the frequency domain to form a cross spectral density matrix by taking the z transform of the above matrix

$$\boldsymbol{R}_{xx}(z) = \sum_{\tau=-W}^{W} \mathbf{R}_{\mathbf{xx}}(\tau)z^{-\tau} \tag{4.10}$$

where W set such that $\mathbf{R}_{\mathbf{xx}}(\tau) \approx 0$ for $|\tau| > W$, and can be determined empirically. This is now a polynomial matrix, which is a fairly recent development and has been discussed in Chapter 3. From here, recent trends, such as the polynomial eigenvalue

decompositions can be exploited. As discussed in Chapter 3, a parahermitian matrix can be decoupled into its paraunitary eigenvectors and polynomial eigenvalues, and these polynomial eigenvalues are representative of a power spectral density, which can be used to enhance detection. The evaluated polynomial eigenvalues of the matrix in Figure 4.6 can be seen in Figure 4.7.

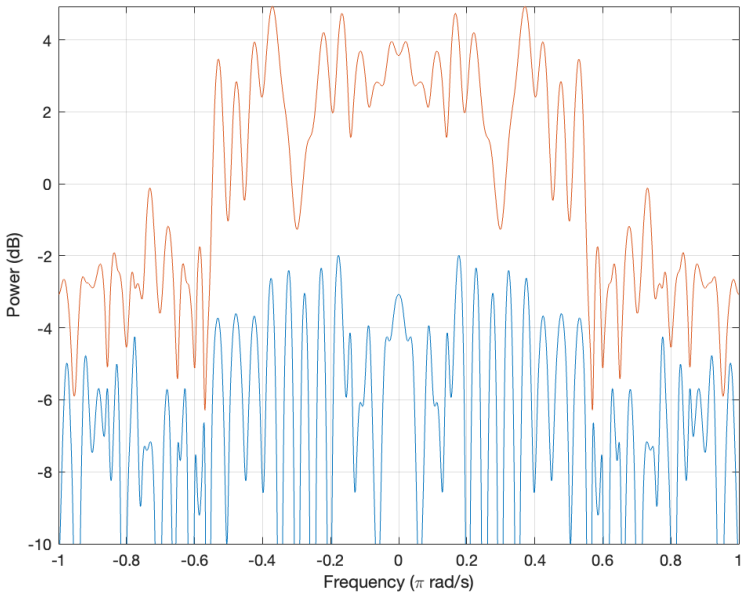

Figure 4.7: Frequency Domain Polynomial Eigenvalues

Since there are only two sensors, there are two eigenvalues. From Figure 4.7, the most significant eigenvalue has an increase in power in the $-0.5 - 0.5\ \pi$ rad/s region, which is a clear indication of a signal of this bandwidth illuminating both antennas.

To summarise, this section has discussed the motivation behind a correlation based receiver and through the use of a 'toy problem', demonstrated that the cross correlation between two sensors has some ability to indicate a weak emitter is present. Since the emitting waveform is unknown, this cross correlation somewhat acts as a pseudo matched filter. This idea is taken a step further in the next sections through the use of polynomial matrices and the PEVD, where the output includes a power spectral density estimate of an emitter buried in noise.

4.3 Signal Model

This section reviews the array signal model for an arbitrary source, $s(t)$, illuminating an M element antenna array in the case of a band limited receiver with an analog down conversion stage. Until now, all analysis of polynomial matrix methods have considered a direct digitisation architecture, which is not practical in many applications. One of the reasons this may be impractical is that the required sampling rate for directly digitised Radar and EW applications is of the order of 10's of Gigahertz.

For elegance of equations, noise is initially omitted. Consider the simple case of one source at a direction of θ illuminating an M element antenna array. The time delay of the complex envelope induced by the direction of arrival between the first and the m^{th} antennas spaced d_m meters apart is

$$\tau_m = \frac{d_m \sin\theta}{c} \tag{4.11}$$

The signal 'seen' at the antennas is

$$\boldsymbol{x}(t) = \begin{bmatrix} s(t) \\ s(t-\tau_2) \\ \vdots \\ s(t-\tau_M) \end{bmatrix} = \begin{bmatrix} \delta(t) \\ \delta(t-\tau_2) \\ \vdots \\ \delta(t-\tau_M) \end{bmatrix} \otimes s(t) \tag{4.12}$$

Omitting the amplifier gain (which is assumed to be purely real and calibrated), the continuous time signal post down-conversion is

$$\boldsymbol{x}(t) = \Big[\begin{bmatrix} \delta(t) \\ \delta(t-\tau_2) \\ \vdots \\ \delta(t-\tau_M) \end{bmatrix} \otimes s(t) \Big] e^{-j\omega_d t} \tag{4.13}$$

At this point it is desirable to form the equation in a similar manner to (4.12) to aid analysis. From Appendix A, it can be seen that

$$[\delta(t-\tau) \otimes s(t)]e^{-j\omega_d t} = [\delta(t-\tau)e^{-j\omega_d \tau}] \otimes [s(t)e^{-j\omega_d t}] \tag{4.14}$$

Thus, the signal seen after the down conversion stage is

$$\boldsymbol{x}(t) = \begin{bmatrix} \delta(t) \\ \delta(t-\tau_2)e^{-j\omega_d \tau_2} \\ \vdots \\ \delta(t-\tau_M)e^{-j\omega_d \tau_M} \end{bmatrix} \otimes s(t)e^{-j\omega_d t} \tag{4.15}$$

and finally the model of the digitised and down converted signal is

$$\begin{aligned} \boldsymbol{x}(n) &= \begin{bmatrix} \tilde{\delta}(n) \\ \tilde{\delta}(n-\tilde{\tau}_2)e^{-j\omega_d \tau_2} \\ \vdots \\ \tilde{\delta}(n-\tilde{\tau}_M)e^{-j\omega_d \tau_M} \end{bmatrix} \otimes s(n)e^{-j\omega_d n T_s} + \boldsymbol{\nu}(n) \\ \boldsymbol{x}(n) &= \boldsymbol{a} \otimes \tilde{s}(n) + \boldsymbol{\nu}(n) \end{aligned} \tag{4.16}$$

here, $\tilde{\boldsymbol{s}}(n)$ is the down converted source signal, and $\boldsymbol{\nu}(n)$ represents the overall additive noise vector, which is assumed to be spatially and temporally uncorrelated, Gaussian and white. $\tilde{\delta}(n-\tilde{\tau})$ represents an ideal fractional delay filter with fractional delay $\tilde{\tau} = \tau/T_s$. The general case of L sources illuminating the array is simply the superposition of all L steered sources and can be expressed as:

$$\begin{aligned} \boldsymbol{x}(n) &= \sum_{l=1}^{L} [\boldsymbol{a}_l \otimes \tilde{s}_l(n)] + \boldsymbol{\nu}(n) \\ &= \boldsymbol{A} \otimes \tilde{\boldsymbol{s}}(n) + \boldsymbol{\nu}(n) \end{aligned} \tag{4.17}$$

Thus far, this section has discussed and derived a general data model for broadband array signal analysis. The next section provides further analysis and insight into the steering vector aspect of the array.

4.3.1 Steering Vector Analysis

Consider the case of a source illuminating an M element ULA, the steering vector is

$$\boldsymbol{a} = \begin{bmatrix} \tilde{\delta}(n) \\ \tilde{\delta}(n-\tilde{\tau})e^{-j\omega_d\tau} \\ \vdots \\ \tilde{\delta}(n-(M-1)\tilde{\tau})e^{-j\omega_d(M-1)\tau} \end{bmatrix} \tag{4.18}$$

let

$$\psi(n) = \tilde{\delta}(n-\tilde{\tau})e^{-j\omega_d\tau} \tag{4.19}$$

and thus its z transform

$$\psi(z) = \sum_{n=-\infty}^{\infty} \psi(n)z^{-n} \tag{4.20}$$

where $\psi(z)$ is representative of an FIR filter to induce a time delay and carrier phase shift between adjacent elements. Thus, the steering vector can now be modelled as

$$\boldsymbol{a}(z) = \begin{bmatrix} \psi^0(z) \\ \psi^1(z) \\ \vdots \\ \psi^{(M-1)}(z) \end{bmatrix} \tag{4.21}$$

Here it is important to note the Vandermonde structure of this steering vector, in the case of a uniform array, as this is used for analysis throughout the remainder of this thesis, and provides an opportunity to explore new algorithms.

4.4 Space-Time Covariance and Source Order

This section explores a model for the polynomial space-time covariance matrix and describes how this can be used for detection and estimation of the number of sources illuminating this array. Following on from the analysis in Chapter 3, if a source is

broadband, then both temporal and spatial correlations need to be considered. The space-time covariance matrix of a stationary signal is:

$$\begin{aligned} \boldsymbol{R}_{xx}(z) &= \sum_{k=-\infty}^{\infty} \boldsymbol{R}_{xx}(k) z^{-k} \\ &= \boldsymbol{A}(z) \tilde{\boldsymbol{R}}_{ss}(z) \boldsymbol{A}^{P}(z) + \sigma_{\nu}^{2} \boldsymbol{I} \end{aligned} \tag{4.22}$$

where the polynomial source covariance matrix, $\tilde{\boldsymbol{R}}_{ss}(z)$ can be modelled as

$$\tilde{\boldsymbol{R}}_{ss}(z) = \begin{bmatrix} \sigma_{11}^{2}(z) & \sigma_{12}^{2}(z) & \dots & \sigma_{1L}^{2}(z) \\ \sigma_{21}^{2}(z) & \sigma_{22}^{2}(z) & \dots & \sigma_{2L}^{2}(z) \\ \vdots & \vdots & \ddots & \vdots \\ \sigma_{L1}^{2}(z) & \sigma_{L2}^{2}(z) & \dots & \sigma_{LL}^{2}(z) \end{bmatrix} \tag{4.23}$$

Decomposing the space-time covariance matrix into polynomial eigenvalues ($\Lambda(z)$) and paraunitary eigenvectors ($\boldsymbol{U}(z)$), this matrix can now take the form

$$\boldsymbol{R}_{xx}(z) \approx \boldsymbol{U}(z) \boldsymbol{\Lambda}(z) \boldsymbol{U}^{P}(z) \tag{4.24}$$

Since the space-time covariance is parahermitian by construction, the eigenvalues matrix will be diagonal with real polynomial coefficients,

$$\boldsymbol{\Lambda}(z) = \begin{bmatrix} \lambda_1(z) & & & \\ & \lambda_2(z) & & \\ & & \ddots & \\ & & & \lambda_M(z) \end{bmatrix} \tag{4.25}$$

and is spectrally majorised such that $\lambda_1(e^{j\omega}) > \lambda_2(e^{j\omega})$. Due to the Vandermonde structure of the polynomial steering vector, $\boldsymbol{A}(z)$, the number of significant eigenvalues of $\boldsymbol{R}_{xx}(z)$ is determined by the rank of the source covariance matrix. Assuming all L sources illuminating the array are uncorrelated, the source covariance matrix will be diagonal. Thus, the number of sources illuminating the array can be estimated through the number of significant eigenvalues.

The eigenvalues can be analysed in two ways:

1. The polynomial can be evaluated for $z = e^{j\omega}$, to estimate the power spectral density
2. The sum of the magnitude of the polynomial eigenvalue coefficients, i.e, $\sum_\tau \mathbf{\Lambda}(\tau)$

and the number of significant eigenvalues can be determined by a simple threshold. While 2. is computationally cheaper and provides a more traditional eigenvalue plot, 1. provides additional spectral information.

4.5 Polynomial Root-MUSIC

Recall the polynomial MUSIC algorithm introduced in Chapter 3

$$P_{mu}(\theta,\omega) = \left. \frac{1}{\boldsymbol{a}^P(\theta,z)\boldsymbol{U}_n(z)\boldsymbol{U}_n^P(z)\boldsymbol{a}(\theta,z)} \right|_{z=e^{j\omega}} \tag{4.26}$$

that produces a spatio-spectrum through a two dimensional heuristic search, and the calculation of each pixel of the resulting spatio-spectrum requires many polynomial multiplications. This results in a computationally expensive estimator. By extending the idea behind the original narrowband Root-MUSIC algorithm [61] to polynomial matrices, in this section a novel, computationally cheaper spatio-spectrum estimator is introduced. The peaks of (4.25) are determined by the (near) zeros of the denominator. Thus, the task is to solve

$$\begin{aligned} \Gamma(z) &= \boldsymbol{a}^P(z)\boldsymbol{U}_n(z)\boldsymbol{U}_n^P(z)\boldsymbol{a}(z) = 0 \\ &= \boldsymbol{a}^P(z)\boldsymbol{C}(z)\boldsymbol{a}(z) = 0 \end{aligned} \tag{4.27}$$

where $\boldsymbol{C}(z) = \boldsymbol{U}_n(z)\boldsymbol{U}_n^P(z)$. Recall that $\boldsymbol{a}(z)$ is a Vandermonde structured vector, where the i^{th} element is $\langle \boldsymbol{a}(z) \rangle_i = \psi^{(i-1)}(z)$, and $\psi(z)$ is representative of an ideal all pass fractional delay filter of delay $\tilde{\tau}$. Its time-reversed conjugate, $\psi^*(z^{-1})$, will have a fractional delay of $-\tilde{\tau}$, thus $\psi(z)\psi^*(z^{-1}) = 1$. Thus, the polynomial $\Gamma(\psi(z))$ can be

formed as a Laurent polynomial containing $2M-1$ coefficients, which are the sums of the sub-diagionals of $\boldsymbol{C}(z)$, i.e.

$$\Gamma(\psi(z)) = \sum_{m-(M-1)}^{M-1} b_m(z)\psi^m(z) \tag{4.28}$$

where $b_m(z)$ is the sum of the m^{th} diagonal of $\boldsymbol{C}(z)$.

Interestingly, $\Gamma(\psi(z))$ is now a 'nested' polynomial that we need to solve for both $\psi(z)$ (direction information) and z (spectral information). Since the polynomial eigenvalues can determine the number of signals overlapping at each frequency bin, this information can be used to evaluate (4.28) for $z = e^{j\omega}$ to estimate the coefficients of a more conventional Laurent polynomial of $\psi(e^{j\omega})$.

$$\Gamma(\psi(e^{j\omega})) = \sum_{l=-(M-1)}^{M-1} b_l(e^{j\omega})\psi^l(e^{j\omega}) \tag{4.29}$$

The problem, now, is to find the roots of several independent polynomials for each frequency containing signal energy. Since $\psi(z)$ is a fractional delay filter with delay $\tilde{\tau}$, at a single frequency this can be expressed simply as a phase shift $e^{j\omega\tau}$. Thus, the L roots closest to the unit circle can be found and reformulated into a direction of arrival estimate:

$$\hat{\theta}_l(e^{j\omega}) = \sin^{-1}\left[\frac{c\arg(q_l(e^{j\omega}))}{\omega d}\right] \tag{4.30}$$

where $\hat{\theta}_l(e^{j\omega})$ is the DoA estimate of the l^{th} source at frequency ω, and $q_l(e^{j\omega})$ represents the root of (4.28) relating to the l^{th} source.

While this technique is computationally cheaper than conventional polynomial MUSIC, it is not without its limitations. Since a Vandermonde structured steering vector is required, this technique is limited to uniform linear arrays. In addition, for large arrays this equates to find the roots of high order polynomials - which is a numerically difficult task.

4.6 Simulations and Analysis

In section 4.2, a toy problem was presented to demonstrate the motivation behind the multi-correlation receiver architecture and polynomial matrix methods. An expansion of this problem is presented in this section through the use a more realistic signal model and a uniform-linear antenna array. In this section a challenging example is presented, whereby using the above method it is possible to detect and separate two temporally overlapping FMCW signals in a low SNR scenario. In section 4.6.3, the accuracy and resolution of the presented methods are derived empirically through Monte Carlo analysis.

4.6.1 Detecting and Locating an LPI Radar - A Challenging Example

In this example, there are two low power, uncorrelated temporally overlapping broadband signals illuminating an antenna array. Both emitters are variants of LFM waveforms, one being a 'sawtooth' linear chirp, and the other being a triangular linear chirp. The sawtooth waveform has an incident power 6 dB less than the triangular waveform. The full signal parameters can be seen in table 4.1.

Table 4.1: Received Signal Parameters

	Emitter#1	Emitter#2
Modulation	Triangular LFM	Sawtooth LFM
Centre Frequency (GHz)	10	10
Pulse Width (μs)	25	55
Bandwidth (GHz)	1	1
SNR (dB)	-5	-11
DoA (deg)	-15	30

The receiver system consists of an $N = 8$ element ULA of isotropic antennas, with an inter-element spacing set to 1.25 cm (spatial Nyquist period for a 12 GHz signal). The RF down converter is set to 10 GHz and the IF signal is sampled at a rate of 4 GS/s (both I and Q channels). A 2000 sample window of data is used for this example. Note that this receiver is an arbitrary example, and not based existing products.

4.6.2 LFM Synthesis

The triangular LFM waveform at the i^{th} antenna is synthesised as

$$p_i(n) = \alpha \cos\Big((\omega_c - \omega_d)(nT_s - \hat{\tau}_i) + \pi\frac{B}{\tau_c}(nT_s)^2\Big), \ -\frac{\tau_c}{2} \leq nT_s \leq \frac{\tau_c}{2} \tag{4.31}$$

and the linear LFM waveform at the i^{th} antenna is synthesised as

$$q_i(n) = \alpha \cos\Big((\omega_c - \omega_d)(nT_s - \hat{\tau}_i) + \pi\frac{B}{\tau_c}(nT_s)^2\Big), \ 0 \leq nT_s \leq \tau_c \tag{4.32}$$

where n is the sample index, α is the signal amplitude, ω_c and ω_d are the carrier and down converter angular frequencies, B is the signal bandwidth, $\hat{\tau}$ is the time delay due to DoA, and τ_c is the chirp duration. When expressed in vector format such that $\boldsymbol{p} = [p_1, p_2, \dots p_N]^T$ and $\boldsymbol{q} = [q_1, q_2, \dots q_N]^T$, the synthesised array signal can be modelled as

$$\boldsymbol{x}(n) = \boldsymbol{p}(n) + \boldsymbol{q}(n) + \boldsymbol{\nu}(n) \tag{4.33}$$

where $\boldsymbol{\nu}(n)$ is the additive white Gaussian noise.

4.6.2.1 Analysis

Since the DoA is unknown, a conventional approach to detecting a signal would be to incoherently combine the frequency spectra of the array signals. The time and frequency domain of the incoherently combined signals can be seen in Figure 4.8

The significant rise in power between 9.5 and 10.5 GHz in Figure 4.8 is suggestive of an emitter being present. However, this analysis cannot estimate the number of sources, their modulation types or pulse width. In Chapter 2, it was noted that a Wigner-Ville distribution could be used to gain this information from an LPI emitter. This is demonstrated in Figure 4.9. As discussed in Chapter 2, the WVD will contain cross terms and this can be seen in Figure 4.9 where the waveforms begin to intersect.

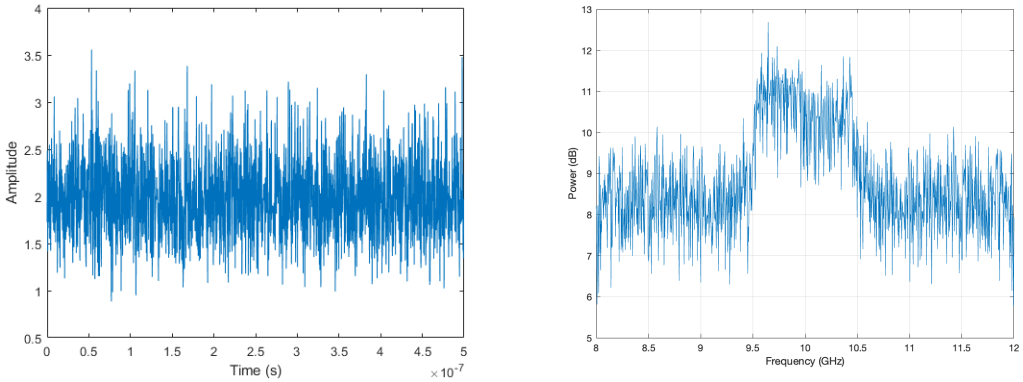

(a) Time Domain Signal (b) Frequency Domain Signal

Figure 4.8: Time and Frequency Signals

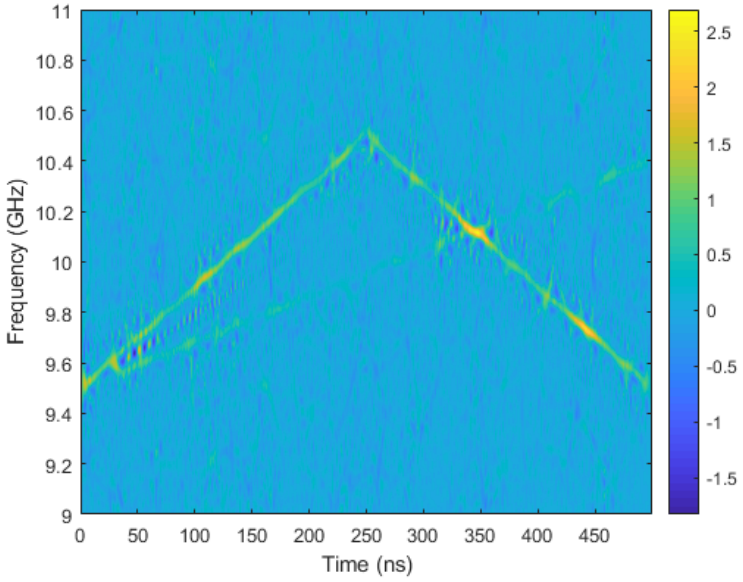

Figure 4.9: Wigner Ville Distribution of the Signal

While this is a significant improvement over the information provided by Figure 4.8, owing to the low SNR of each emitter, and the 6 dB difference in signal powers, the peaks in this Wigner-Ville distribution are fairly weak. While the triangular waveform can be seen, the sawtooth signal is very faint.

To compliment the above approach, polynomial matrices can be used. A space-time covariance matrix is constructed using (4.9) and (4.10), where the time domain correlation limits (W) are set to ± 40, since there is near zero correlation past this point. The space-time covariance matrix can be seen in Figure 4.10.

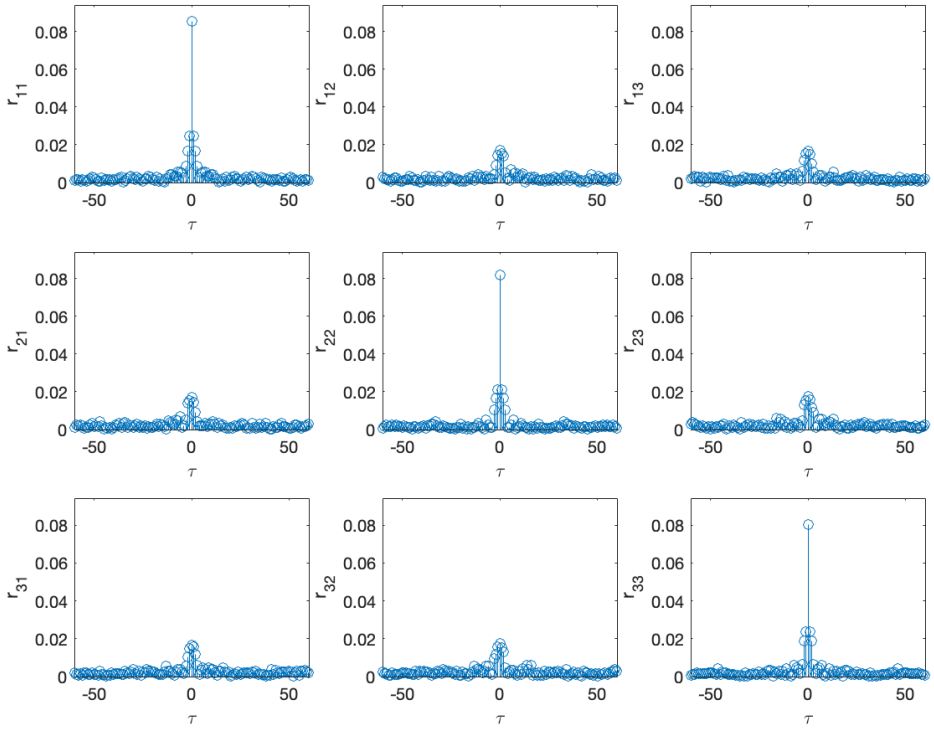

Figure 4.10: Space-Time Covariance Matrix

While this provides fairly little information in isolation, the non zero cross correlation terms (off-diagonals) suggest some signal is present. To extract more information, this can be decomposed into its polynomial eigenvectors and eigenvalues. Recall that the polynomial eigenvalues are now representative of a power spectral density, so these

polynomials can be evaluated to estimate the number of signals illuminating the array, as well as an estimate of their frequencies. This can be seen in Figure 4.11

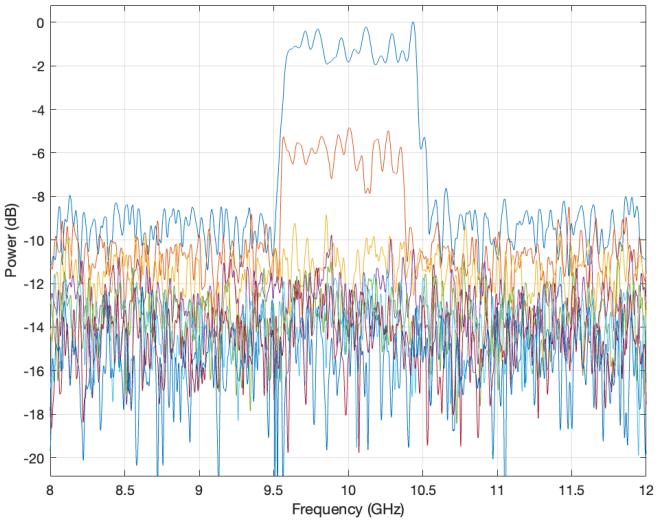

Figure 4.11: Frequency Domain Plot of the Polynomial Eigenvalues of Figure 4.10

Figure 4.11 shows that there are two significant eigenvalues with an overlapping frequency between 9.5 and 10.5 GHz. The paraunitary eigenvectors can now be partitioned into signal and noise subspaces, and subsequently perform SSP-MUSIC, or its computationally more efficient version presented earlier in this chapter, the Root SSP-MUSIC algorithm.

Both estimates in Figure 4.12 present the same information that between 9.5 and 10.5 GHz there are two emitters present at -15 degrees and 30 degrees. Since the Root SSP-MUSIC simply estimates the L peaks of the SSP-MUSIC algorithm at each frequency bin without the need to perform the heuristic scan, it makes this estimate significantly cheaper computationally. This will be discussed further in the following section. Now, since the directions of the signal have been estimated, a simple delay and sum beamformer can be applied to separate the signals.

In conjunction with the WVD, the individual signals and their modulations can easily be seen in Figure 4.13, with a much stronger amplitude than in Figure 4.9 due to the coherent combination from the beamforming stage. While the simple delay-

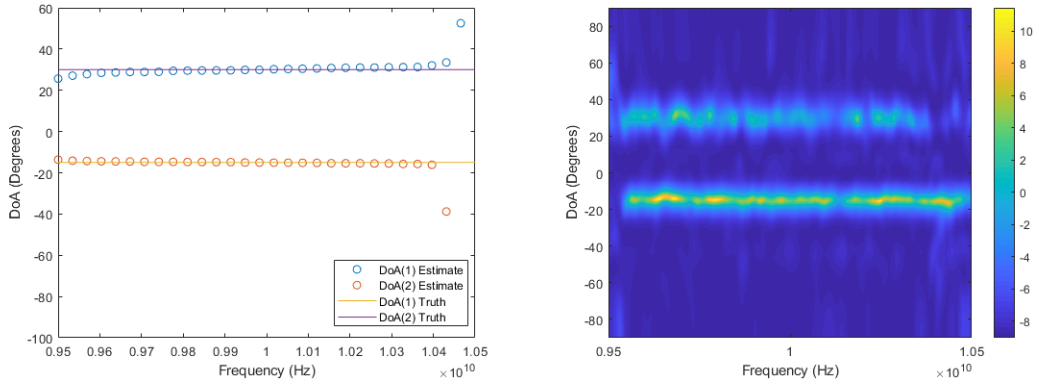

(a) (b)

Figure 4.12: Spatio Spectrum Estimation using (a) Polynomial Root MUSIC (b) Conventional Polynomial MUSIC

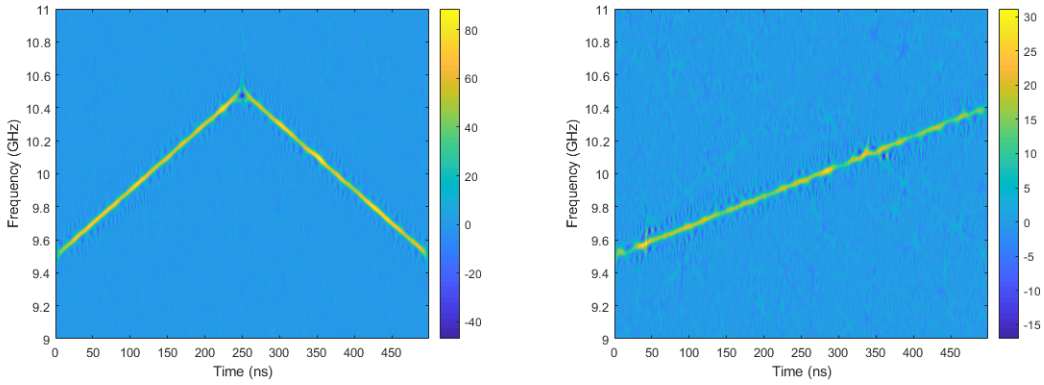

(a) (b)

Figure 4.13: Beamformed estimates of (a) Emitter 1 (b) Emitter 2

sum beamformer is the optimal SNR solution, results could further be improved using an adaptive broadband MVDR beamformer [99] to optimise SINR in effort to fully separate the sources, i.e. further attenuating the triangular chirp from Figure 4.13(b). However, this is outside the scope of this thesis.

4.6.3 Accuracy and Computational Cost Analysis

A Monte-Carlo simulation was performed to analyse the performance of both the SSP-MUSIC and Root SSP-MUSIC algorithms under different SNRs. For each run, the DoA of the source was chosen at random from a uniformly distributed set of possible

DoAs, $\theta_p \in [-50°, 50°]$. For each SNR point, 100 Monte Carlo runs were performed. Figure 4.14 displays the mean squared error of the estimators and it is easy to see that both the SSP-MUSIC and Root SSP-MUSIC algorithms exhibit a very similar performance. This is expected since the Root SSP-MUSIC algorithm finds the L peaks of the angular spectra for each frequency point of the Polynomial MUSIC algorithm. The small differences observed are likely to be because of the difference in precision of the estimators as Polynomial MUSIC was performed with an angular search grid spacing of 1 degree, whereas the DoA estimates from the Root Polynomial MUSIC estimator were calculated using double precision floating point numbers.

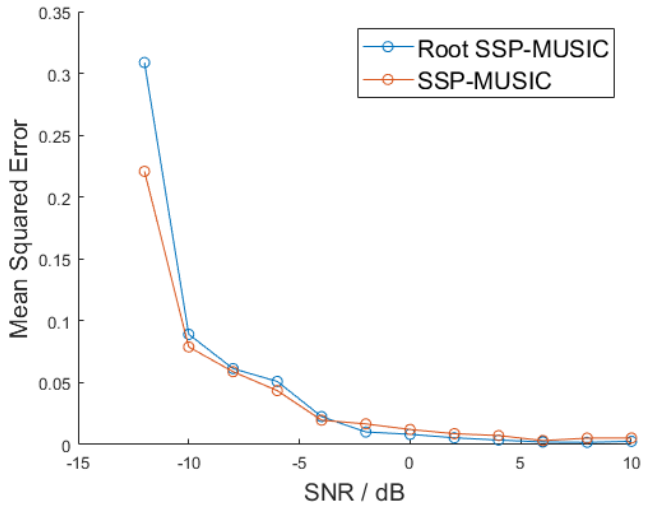

Figure 4.14: MSE for Monte Carlo simulation at specific SNRs

The heuristic angular search of the SSP-MUSIC algorithm is an expensive computational task. This is due to the polynomial matrix multiplications when calculating $\Gamma(\theta, z)$. The Root SSP-MUSIC algorithm replaces the heuristic search with finding the roots of a polynomial. Both algorithms, however, still require polynomial eigenvalue analysis to estimate the spatio-spectrum.

The computer performing this simulation utilised the following hardware and software: Intel core i7-6700 quad-core processor, 16 Gb DDR4 RAM, 256 Gb SSD, Windows 7 64 bit, MATLAB R2016b.

Table 4.2: Normalised Mean Computation time for SSP-MUSIC and Root SSP-MUSIC algorithm

N_{bins}	30	60	120	240
Mean Norm. SSP-MUSIC Comp Time	1	1.04	1.124	1.268
Mean Norm. Root SSP-MUSIC Comp Time	0.039	0.054	0.079	0.131

The mean normalised simulation time from 100 runs of both algorithms is displayed in Table 4.2. All values are normalised to the SSP-MUSIC computation time for 30 frequency bins. These results show that the Root SSP-MUSIC algorithm is considerably faster in computation time, but has a stronger scaling with the number of frequency bins evaluated. Thus for a large number of bins, both algorithms will have similar complexity. However, in general, the novel Root SSP MUSIC estimator offers equal performance to the conventional SSP-MUSIC estimation, but in a fraction of the computation time.

4.7 Conclusion

In this chapter, a multi-correlation receiver was proposed. In Section 4.2, a toy problem was discussed to highlight the motivation behind this technology. The statistical and correlation properties of noise between two receivers was explored, and an example was presented where the two receivers measured the same source at a low SNR. This example demonstrated that the sources could be detected through these correlation techniques, where time and frequency domain techniques alone could not produce anything that would result in an obvious detection. This concept was further explored in Section 4.3, where a representative model was derived. This model included a frequency down-conversion stage.

The polynomial space-time covariance matrix was discussed in further detail within Section 4.4. This section highlighted how the polynomial eigenvalues could be exploited for signal detection purposes, and for the estimation of the number of sources illuminating the array.

Section 4.5 introduced a novel algorithm proposing a significant reduction in computation time over the standard Polynomial MUSIC algorithm. This reduction in computation time was demonstrated in Section 4.6 with a significant effect, while still maintaining the high accuracy and fine resolution of the conventional Polynomial MUSIC algorithm. This section also demonstrated a challenging scenario of detecting and estimating the directions of two low power FMCW LPI emitters, as well as separating the two emitters via standard delay-sum techniques. Wigner-Ville time frequency analysis techniques discussed in Chapter 2 aided this demonstration, highlighting that the methods presented in this thesis might not replace conventional LPI detection algorithms, but they do provide enhanced performance.

Chapter 5

Super-Resolution DoA Estimation of Coherent Broadband Sources

5.1 Introduction

The focus of this chapter is the development of novel direction of arrival estimation methods for correlated broadband signals. While broadband sources are naturally resilient to multipath fading, there may be scenarios where strongly correlated waveforms arrive from different directions, such as scatters closely located to the main emitter, or from a decoy [115]. In effort to solve this problem, two novel methods are proposed and analysed. Section 5.2 extends the analysis of the well known spatial smoothing algorithm to broadband scenarios through the use of polynomial matrices. In Section 5.3 analysis is provided to demonstrate that the spatial smoothing effect is naturally present when estimating a covariance matrix from an array in motion. Finally, conclusions are presented in Section 5.4

5.2 Broadband Spatial Smoothing

For the broadband angular super resolution algorithms presented in Chapters 2 & 4, one of the key assumptions made was that the sources illuminating the array are uncorrelated. Recall that the polynomial space-time covariance matrix can be expressed as

$$\boldsymbol{R_{xx}}(z) = \boldsymbol{A}(z)\boldsymbol{R_{ss}}(z)\boldsymbol{A}^P(z) + \sigma_\nu^2\boldsymbol{I} \tag{5.1}$$

Where $\boldsymbol{A}(z) \in \mathbb{C}^{M\times L}(z)$ is an array of steering vectors

$$\boldsymbol{A}(z) = [\boldsymbol{a_1}(z), \boldsymbol{a_2}(z), \ldots, \boldsymbol{a_L}(z)] \tag{5.2}$$

and each column possesses a Vandermonde structure. The source correlation matrix is defined as

$$\boldsymbol{R}_{ss}(\tau) = E[\boldsymbol{s}(n)\boldsymbol{s}^H(n-\tau)] \tag{5.3}$$

Where $\boldsymbol{R}_{ss}(z) = \sum_\tau \boldsymbol{R}_{ss}(\tau)z^{-\tau}$. Recall that in Chapter 4, the number of significant eigenvalues were used to determine the dimensions of the signal and noise subspaces, and to provide an estimate of the number of sources illuminating the array. This quantity is dependent on the rank of the term $\boldsymbol{A}(z)\boldsymbol{R}_{ss}(z)\boldsymbol{A}^P(z)$, which will be of rank $\min(\text{rank}(\boldsymbol{A}(z)), \text{rank}(\boldsymbol{R}_{ss}(z)))$. Since the steering vectors possess a Vandermonde structure, this steering matrix will be full rank (rank L). The source cross spectral density matrix is structured as:

$$\boldsymbol{R}_{ss}(z) = \begin{bmatrix} r_{11}(z) & \ldots & r_{L1}(z) \\ \vdots & \ddots & \vdots \\ r_{1L}(z) & \ldots & r_{LL}(z) \end{bmatrix} \tag{5.4}$$

When the sources illuminating the array are completely uncorrelated, $\boldsymbol{R}_{ss}(z)$ will be diagonal and be of rank L, and the dimensions of the signal subspace of $\boldsymbol{R}_{xx}(z)$ will be L. However, if the sources are coherent, then $\boldsymbol{R}_{ss}(z)$ will have rank $< L$ (or even rank 1 in the case of coherent sources).

The impact of this is that when sources are coherent, the size of the signal subspace is smaller than the number of spectrally overlapping signals, and the resulting signal subspace will contain some combination of the steering vectors. However, owing to the Vandermonde structure of the steering vectors, no linear combination of steering vectors can result in another valid (Vandermonde) steering vector. The true steering vectors will no longer be orthogonal to the noise subspace and this results in loss of the super-resolution property in the polynomial subspace based estimators.

To overcome this issue, the spatial smoothing technique can be applied to polynomial space-time covariance matrices. The underlying method is to separate the ULA into $K-1$ overlapping subarrays (which are also ULAs) of length $M-(K-1)$, where K is the number of coherent sources. Then, a space-time covariance matrix is calculated for each subarray. The subarrays are then averaged to form the 'spatially smoothed' space-time covariance matrix. Recall the time domain signal model of an M element array:

$$\boldsymbol{x}(n) = \boldsymbol{A}(n) \otimes \boldsymbol{s}(n) + \boldsymbol{\nu}(n) \tag{5.5}$$

This can be partitioned into $(K-1)$ subarrays using appropriate selection matrices. Thus the k^{th} subarray is

$$\begin{aligned} \boldsymbol{x}_k(n) = \boldsymbol{T}_k \boldsymbol{x}(n) &= \boldsymbol{T}_k \boldsymbol{A}(n) \otimes \boldsymbol{s}(n) + \boldsymbol{T}_k \boldsymbol{\nu}(n) \\ &= \boldsymbol{A}_k(n) \otimes \boldsymbol{s}(n) + \boldsymbol{\nu}_k(n) \end{aligned} \tag{5.6}$$

where

$$\begin{aligned} \boldsymbol{A}_k(n) &= \boldsymbol{T}_k \boldsymbol{A}(n) \\ \boldsymbol{\nu}_k(n) &= \boldsymbol{T}_k \boldsymbol{\nu}(n) \end{aligned} \tag{5.7}$$

and T_k is an $M-(K-1) \times M$ selection matrix. It is defined by the following block matrix:

$$\boldsymbol{T}_k = \begin{bmatrix} O_{(M-(K-1))\times(k-1)} & \mathcal{I}_{(M-(K-1))} & O_{(M-(K-1))\times(K-k)} \end{bmatrix} \tag{5.8}$$

where $O_{p\times q}$ represents an $p \times q$ zero matrix, and $\mathcal{I}_p$ is a $p \times p$ identity matrix. For a ULA, the Vandermonde structured steering vector gives translational invariance across the array. Thus the steering vector for each subarray can be expressed as

$$\boldsymbol{A}_k(z) = \boldsymbol{T}_k \boldsymbol{A}(z) = \boldsymbol{A}_0(z)\boldsymbol{D}^{(k-1)}(z) \tag{5.9}$$

where $\boldsymbol{D}(z)$ is a diagonal polynomial matrix to induce an integer multiple of additional unit delays for each source in the fundamental subarray steering matrix $\boldsymbol{A}_0(z)$

$$\boldsymbol{D}(z) = \begin{bmatrix} \psi_1(z) & & \\ & \ddots & \\ & & \psi_L(z) \end{bmatrix} \tag{5.10}$$

and the fundamental sub array steering matrix

$$\boldsymbol{A}_0(z) = \begin{bmatrix} \psi_1^0(z) & \psi_2^0(z) & \dots & \psi_L^0(z) \\ \psi_1^1(z) & \psi_2^1(z) & \dots & \psi_L^1(z) \\ \vdots & \vdots & \ddots & \vdots \\ \psi_1^{(M-L)}(z) & \psi_2^{(M-L)}(z) & \dots & \psi_L^{(M-L)}(z) \end{bmatrix} \tag{5.11}$$

The time domain signal from (5.6) can now be described as

$$\boldsymbol{x}_k(n) = [\boldsymbol{A}_0(n) \otimes \boldsymbol{D}^{(k-1)}(n)] \otimes \boldsymbol{s}(n) + \boldsymbol{\nu}_k(n) \tag{5.12}$$

The space-time covariance of the k^{th} subarray can be described as

$$\begin{aligned} \boldsymbol{R}_{xx_k}(z) &= \sum_{\tau=-\infty}^{\infty} \mathbf{R}_{\mathbf{xx_k}}(\tau) z^{-\tau} = \sum_{\tau=-\infty}^{\infty} E[\boldsymbol{x}_k(n)\boldsymbol{x}_k^H(n-\tau)] z^{-\tau} \\ &= \boldsymbol{A}_0(z)\boldsymbol{D}^{(k-1)}(z)\boldsymbol{R}_{ss}(z)\boldsymbol{D}^{P(k-1)}(z)\boldsymbol{A}_0^P(z) + \sigma_\nu^2 \mathcal{I} \end{aligned} \tag{5.13}$$

The spatially smoothed space-time covariance matrix, $\hat{\boldsymbol{R}}_{xx}(z)$ is calculated via the mean

of all K sub-arrays, and takes the form of

$$\begin{aligned}\hat{\boldsymbol{R}}_{xx}(z) &= \frac{1}{K}\sum_{k=1}^{K}\boldsymbol{R}_{xx_k} = \boldsymbol{A}_0(z)\Big[\frac{1}{K}\sum_{k=1}^{K}\boldsymbol{D}^{(k-1)}(z)\boldsymbol{R}_{ss}(z)\boldsymbol{D}^{P(k-1)}(z)\Big]\boldsymbol{A}_0^P(z) + \sigma_\nu^2\boldsymbol{I} \\ &= \boldsymbol{A}_0(z)\hat{\boldsymbol{R}}_{ss}(z)\boldsymbol{A}_0^P(z) + \sigma_\nu^2\boldsymbol{I}\end{aligned} \tag{5.14}$$

where $\hat{\boldsymbol{R}}_{ss}(z)$ is the modified source cross spectral density matrix

$$\hat{\boldsymbol{R}}_{ss}(z) = \frac{1}{K}\sum_{k=1}^{K}\boldsymbol{D}^{(k-1)}(z)\boldsymbol{R}_{ss}(z)\boldsymbol{D}^{P(k-1)}(z) \tag{5.15}$$

This process has the effect of transferring energy from the off-diagonal to the diagonal elements of the source covariance matrix. The following proof is an extension of the proof presented in [74] and [72] on spatial smoothing techniques for narrowband scenarios.

5.2.1 Proof

In this section, a proof is presented to demonstrate that the spatial smoothing technique restores the rank of the source covariance matrix if the condition of the number of subarrays is at least the number of coherent sources. For simplicity, consider the worst case scenario where all L sources are coherent, as this provides a good model for the strongly correlated case. Since the non-modified source covariance matrix is parahermitian, this can be decomposed into the following vector product

$$\boldsymbol{R}_{ss}(z) = \boldsymbol{\gamma}(z)\boldsymbol{\gamma}^P(z) \tag{5.16}$$

Thus, the modified source cross spectral density can be rewritten as:

$$\hat{\boldsymbol{R}}_{ss}(z) = \frac{1}{K}\sum_{k=1}^{K}\boldsymbol{D}^{(K-1)}(z)\boldsymbol{\gamma}(z)\boldsymbol{\gamma}^P(z)\boldsymbol{D}^{P(K-1)}(z) \tag{5.17}$$

This summation can be expressed in matrix form and factored as

$$\hat{\boldsymbol{R}}_{ss}(z) = \frac{1}{K}\boldsymbol{B}(z)\boldsymbol{B}^{P}(z) \tag{5.18}$$

where

$$\boldsymbol{B}(z) = [\boldsymbol{D}^{0}(z)\boldsymbol{\gamma}(z), \boldsymbol{D}^{1}(z)\boldsymbol{\gamma}(z), \ldots, \boldsymbol{D}^{K-1}(z)\boldsymbol{\gamma}(z)] \tag{5.19}$$

It can be noted that the rank of the modified source cross spectral density matrix, $\hat{\boldsymbol{R}}_{ss}(z)$, is the same as that of $\boldsymbol{B}(z)$. Hence the task, now, is to prove that when $K \geq L$, the rank of $\boldsymbol{B}(z)$ is L. This matrix can be rewritten as a product of a polynomial diagonal, and Vandermonde matrix, as

$$\boldsymbol{B}(z) = \begin{bmatrix} \gamma_1(z) & & \\ & \ddots & \\ & & \gamma_P(z) \end{bmatrix} \begin{bmatrix} \psi_1^0(z) & \ldots & \psi_1^{K-1}(z) \\ \vdots & \ldots & \vdots \\ \psi_P^0(z) & \ldots & \psi_P^{K-1}(z) \end{bmatrix} \tag{5.20}$$

The rank of $\boldsymbol{B}(z)$ will be entirely dependent on the rank of the Vandermonde matrix, providing the diagonal matrix is at full rank, i.e. $\boldsymbol{\gamma}(z)$ contains only non-zero elements. The latter point is guaranteed due to the sources being present and correlated with themselves.

The resulting rank of $\boldsymbol{B}(z)$ will be $\min((M-(K-1)), K)$. Thus, the modified source covariance density matrix will be of full rank, providing $K \geq L$, i.e. there are at least as many sub-arrays as there are coherent sources.

This spatial averaging technique does, however, lead to an overall reduction in the effective array aperture. The general requirement of more sensors than sources still holds true for the sub-array length, i.e. $(M-(K-1)) > L$. Thus, for a situation where there are L coherent sources present, the minimum overall array length must be $M \geq 2L$.

5.2.2 Simulations

In addition to the above proof, simulation results provided in this section aid in verifying that spatial smoothing combined with the polynomial MUSIC algorithm can indeed provide an improved spatial resolution of correlated sources.

To assess the performance of the spatially smoothed polynomial MUSIC algorithm for strongly correlated sources, the SMD PEVD algorithm [104] was performed on both, the non-spatially smoothed space-time covariance matrix and on the spatially smoothed version. The SSP-MUSIC algorithm was subsequently used for spatio-spectral estimation. Comparisons between the spatio-spectral estimations were made via the resulting peak-height and peak-width in the spatio-spectrum as this is indicative of the algorithm's angular resolution.

Both simulations were performed using the same synthetic data (where ideal anechoic conditions are assumed), wherein two, 10,000 sample long, coherent CW noise/ OFDM-like sources were present. The source signals were synthesised as $I = 1000$ linearly spaced sub-carriers within the normalised frequency region $\Omega \in [0.3\pi, 0.8\pi]$. This can be expressed as

$$s(n) = \sum_{i=1}^{I} e^{j\Omega(i)n} e^{j\phi(i)} \tag{5.21}$$

where $\Omega(i)$ and $\phi(i)$ represent the normalised frequency and phase of the i^{th} sub-carrier.

The two identical synthesised signals were steered to directions of -40° and 30°. The received SNR was set to 5dB, whereby the noise was Gaussian, spectrally white, and uncorrelated with itself and the sources present. The overall antenna array length was the same for both algorithms ($M = 7$).

The previous section found that when coherent sources are present, the dimensions of the signal subspace do not coincide with the number of sources present. Given the above analysis and the fact that both sources are coherent in this scenario, only a one dimensional signal subspace was expected. Figure 5.1 shows the eigenvalue power spectral density of the non-smoothed space-time covariance matrix, which agrees with

this expectation as there is only one eigenvalue with significant magnitude, in spite of there being two sources.

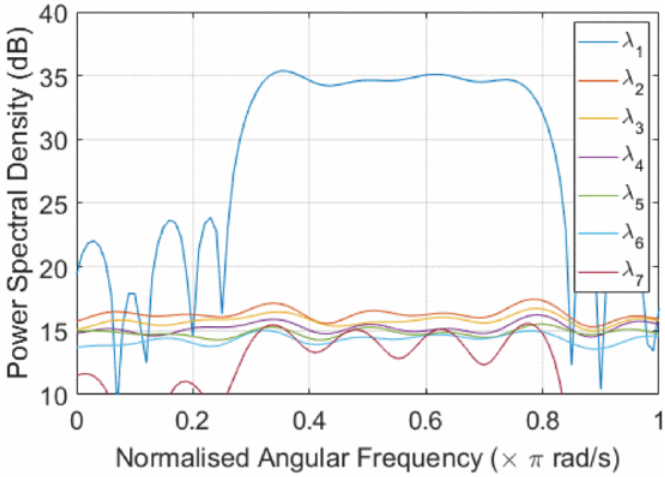

Figure 5.1: Frequency Domain Plot of Polynomial Eigenvalues without Spatial Smoothing

The assumption that steering vectors are part of the signal subspace is still valid. However, as there are more sources than signal eigenvectors, the latter contains a combination of the source's steering vectors. Due to the Vandermonde structure of the steering vectors, no linear combination of these could result in a legitimate steering vector. This means that the true steering vectors will no longer be orthogonal to the noise subspace. This is severely detrimental to the angular resolution of the polynomial MUSIC algorithm. This loss of resolution can have a knock-on effect when it is part of a larger system, such as a decreased probability of detection in passive applications. Figure 5.2 shows the spatio-spectral estimation for the non-spatially smoothed case. While there are noticeable spatial peaks around $-40°$ and $30°$, the peaks are wide ($\sim 20°$ 1 dB width) and less than 5 dB in magnitude (relative to the floor).

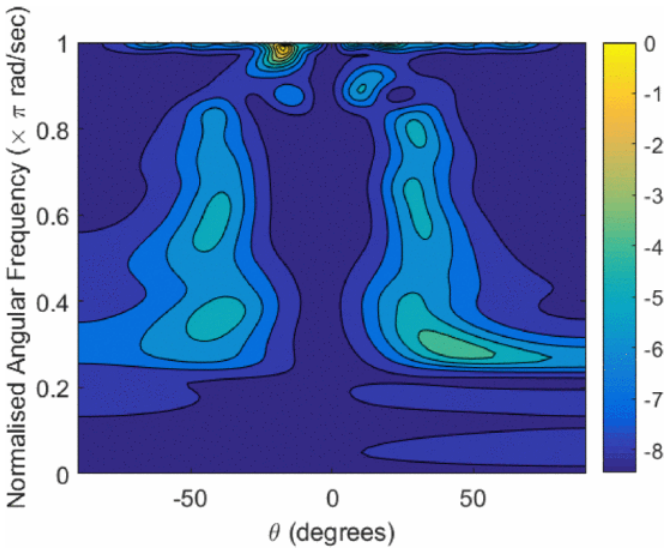

Figure 5.2: SSP-MUSIC of coherent sources without spatial smoothing

As mentioned in the previous section, spatial smoothing will restore the rank of the source cross spectral density matrix, providing the conditions $K \geq P$ and $L > P$ are met. In this particular scenario, the 7 element antenna array is split into 3 overlapping sub-arrays and is shown in Figure 5.3. This yields an effective array length of 5 - satisfying the above condition. Figure 5.4 shows the power spectral density (PSD) of the polynomial eigenvalues, two of which have significant magnitudes over the same wide bandwidth. This is suggestive of two sources illuminating the array.

The resulting estimate of the signal subspace will contain the true steering vectors associated with each source. When scanning the null space of the noise subspace, the

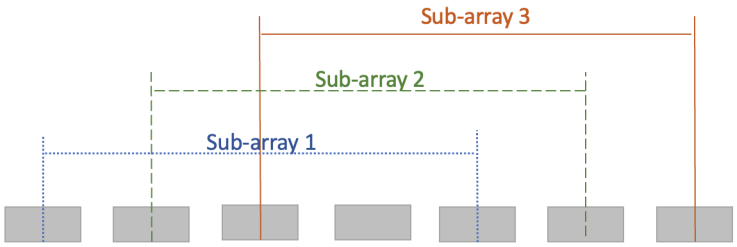

Figure 5.3: Splitting the 7 element ULA into 5 overlapping subarrays

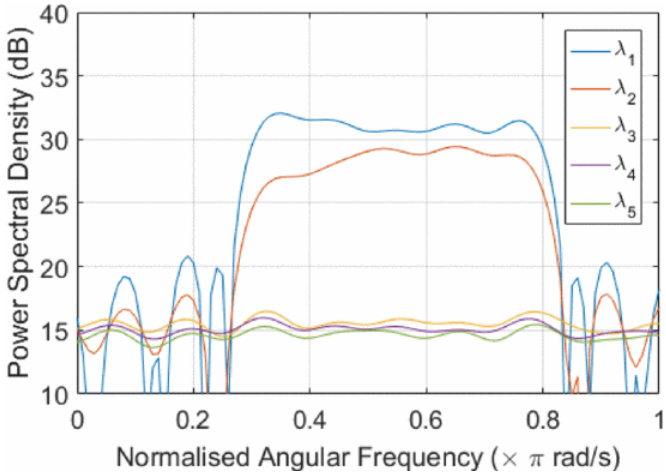

Figure 5.4: Frequency Domain Plot of Polynomial Eigenvalues with Spatial Smoothing

true steering vectors will be orthogonal to this, leading to very tall and sharp peaks in the spatial spectrum. This will have a similar performance to the uncorrelated case of the SSP-MUSIC algorithm, as can be seen in Figure 5.5.

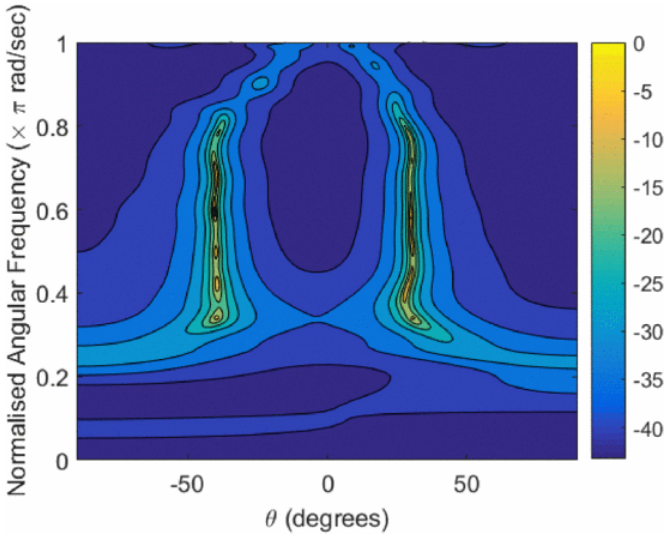

Figure 5.5: SSP-MUSIC of coherent sources with spatial smoothing

The spatially smoothed SSP-MUSIC algorithm produces a spatio-spectrum with a much higher angular resolution, and a 1 dB peak width of $\sim 1°$. The spatial only characteristics of the spatially smoothed and standalone versions of the SSP-MUSIC algorithm are displayed in Figure 5.6. This spatial only representation is determined

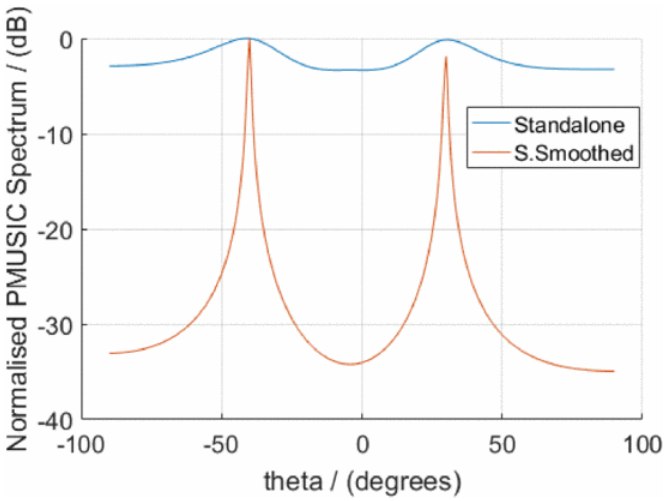

Figure 5.6: Spatial Only Polynomial MUSIC comparison between standalone, and spatially smoothed covariance matrices

via spectral averaging over the bandwidth of sources.

5.2.3 A Remark on the Selection of Subarray Size

The broadband spatial smoothing scheme requires at least as many subarrays as coherent sources in order to restore the rank of the source covariance matrix. However, this does imply that the number of coherent sources are known a priori, which is an unlikely scenario. While a method to estimate the number of coherent sources is outside the scope of this thesis, one possible method would be perform a iterative method of increasing the number of subarrays until no further significant eigenvalues are present, effectively indicating the number of coherent sources. Such a method would however be computationally expensive, and improved methods would be subject to further research in this area.

5.2.4 Summary

Through the extension of a popular narrowband technique, this section has introduced an improved variation of the polynomial MUSIC algorithm, providing a potential solution to the problem of broadband direction of arrival estimation in an environment with strongly correlated sources. Simulation results were presented to assess the perfor-

mance gain of using this spatial smoothing technique for coherent broadband direction of arrival estimation, in conjunction with the use of polynomial MUSIC algorithm. The non-smoothed polynomial MUSIC algorithm encounters serious difficulties that are manifested as a loss of resolution in the presence of strongly correlated, or coherent sources. When the spatial smoothing technique is applied to the polynomial covariance matrix, the polynomial MUSIC algorithm produces similar results to the case of uncorrelated sources, with a relatively modest loss of aperture.

5.3 Doppler Induced Spatial Smoothing

The previous section concluded that spatial smoothing can effectively decorrelate sources by truncating the full aperture into subarrays, reducing the effective aperture of the system. This in turn has negative consequences for spatial resolution. This section presents analysis to demonstrate that the effect of spatial smoothing can occur naturally if data is acquired while the array is in motion, removing the need to reduce effective aperture to decorrelate sources.

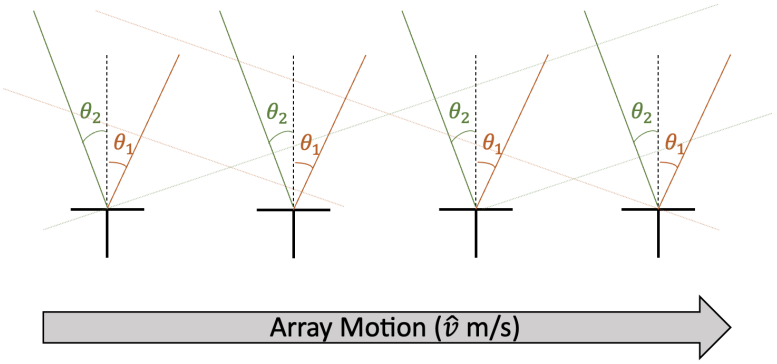

Figure 5.7: Array in Motion Illuminated by two Emitters

Consider an array travelling with lateral motion at a constant speed of $\hat{v}$ m/s, as illustrated in Figure 5.7. The receiver system has a sampling period of T_s, and thus the distance travelled between individual samples is $\hat{v}T_s$, and more generally, the distance the array travelled at sample point n is

$$\hat{d}(n) = n\hat{v}T_s \tag{5.22}$$

The data model for an array in such a motion is similar to (5.5). However, the steering vector is now time varying, i.e.

$$\boldsymbol{x}(n) = \sum_{\tau}[\hat{\boldsymbol{A}}(\tau, n)\boldsymbol{s}(n-\tau)] + \boldsymbol{\nu}(n) \tag{5.23}$$

Under the assumption that the source is sufficiently far such that its DoA remains approximately constant throughout the acquisition, the time-varying steering vector can be modelled as a stationary steering vector, multiplied by some time-dependent translational factor, $\boldsymbol{Q}(n)$

$$\hat{\boldsymbol{A}}(\tau, n) = \sum_{\tau} \boldsymbol{A}(n-\nu)\boldsymbol{Q}(\tau, \nu) \tag{5.24}$$

where $\boldsymbol{A}(\tau)$ is the same steering matrix as in (5.2). The translational factor $\boldsymbol{Q}(\tau, n)$ is an L dimensional diagonal time-dependent matrix,

$$\boldsymbol{Q}(\tau, n) = \begin{bmatrix} \phi_1(\tau, n) & & & \\ & \phi_2(\tau, n) & & \\ & & \ddots & \\ & & & \phi_L(\tau, n) \end{bmatrix} \tag{5.25}$$

and each element is an ideal fractional delay filter. The delay is due to the additional wavefront distance travelled compared to the initial position at acquisition at time index $n = 1$, i.e.

$$\phi_i(\tau, n) = \hat{\delta}(n - \hat{v}\tau\sin(\theta_i)/c) \tag{5.26}$$

where $\hat{\delta}(n - \hat{v}\tau\sin(\theta_i)/c)$ denotes a fractional delay filter of delay $\hat{v}\tau\sin(\theta_i)/c$. In effect, this describes the rate of change of linear phase shift across all frequencies. While not immediately obvious from the above equation, this can be expressed in the frequency domain as

$$\phi_i(e^{j\omega}) = e^{j\omega\hat{v}n\sin(\theta_i)/c} \tag{5.27}$$

The phase component of this is simply $\omega\hat{v}n\sin(\theta_i)/c$. Since this phase varies linearly with time, this can be translated into a frequency by taking the derivative of the phase with respect to time

$$\Delta\omega = \omega\hat{v}\sin(\theta_i)/c \tag{5.28}$$

which is a familiar formula as it is simply the Doppler shift induced through the motion of an array. Now, the task is to analyse how the induced Doppler shift can decorrelate sources.

Through substituting (5.24) into (5.1), the polynomial space-time covariance matrix can now be expressed as

$$\boldsymbol{R}_{xx}(z) = \boldsymbol{A}(z)\hat{\boldsymbol{R}}_{ss}(z)\boldsymbol{A}^P(z) + \sigma_\nu^2\mathcal{I} \tag{5.29}$$

where $\hat{\boldsymbol{R}}_{ss}(z)$ is the modified source covariance matrix and can be expressed as

$$\hat{\boldsymbol{R}}_{ss}(z) = \frac{1}{N}\sum_{n=1}^{N}\boldsymbol{Q}^{(n-1)}(z)\boldsymbol{R}_{ss}(z)\boldsymbol{Q}^{P(n-1)}(z) \tag{5.30}$$

Similar to the proof presented in Section 5.2, this stage can be proved to restore the rank of the source covariance matrix, providing there is some amount of translational array motion during the acquisition. While this rank restoration demonstrates at least some amount of decorrelation, it does not guarantee a similar performance to the case of uncorrelated sources as there could still be significant power in the off-diagonal terms of this matrix. Thus, the next objective is to measure the quality of decorrelation.

One method to determine the amount of decorrelation due to the Doppler induced spatial smoothing is to quantify the amount of energy that has been shifted from the off-diagonals to the main diagonal of the source covariance matrix. Consider the case of two identical white noise sources with equal power and a bandwidth identical to the system's sampling frequency. Their auto and cross correlation functions will be a

Dirac-delta function with a peak equal to the source power. For simplicity, assume this power is 1. Thus, in this case, the source covariance matrix can be expressed as

$$\boldsymbol{R}_{ss}(z) = \begin{bmatrix} 1 & 1 \\ 1 & 1 \end{bmatrix} \tag{5.31}$$

Thus, the modified source covariance matrix

$$\hat{\boldsymbol{R}}_{ss}(z) = \frac{1}{N}\sum_{n=1}^{N} \begin{bmatrix} \phi_1^{(n)}(z) & 0 \\ 0 & \phi_2^{(n)}(z) \end{bmatrix} \begin{bmatrix} 1 & 1 \\ 1 & 1 \end{bmatrix} \begin{bmatrix} \phi_1^{P(n)}(z) & 0 \\ 0 & \phi_2^{P(n)}(z) \end{bmatrix} \tag{5.32}$$

which simplifies to

$$\begin{aligned} \hat{\boldsymbol{R}}_{ss}(z) =& \frac{1}{N}\sum_{n=0}^{N-1} \begin{bmatrix} \phi_1^{(n)}(z)\phi_1^{P(n)}(z) & \phi_1^{(n)}(z)\phi_2^{P(n)}(z) \\ \phi_1^{P(n)}(z)\phi_2^{(n)}(z) & \phi_2^{(n)}(z)\phi_2^{P(n)}(z) \end{bmatrix} \\ =& \frac{1}{N}\sum_{n=1}^{N} \begin{bmatrix} 1 & \phi_1^{(n)}(z)\phi_2^{P(n)}(z) \\ \phi_1^{P(n)}(z)\phi_2^{(n)}(z) & 1 \end{bmatrix} \end{aligned} \tag{5.33}$$

In effort to simplify analysis, the covariance matrix at the frequency, ω_c can be considered. Recall that the polynomial $\phi_i(z)$ is a fractional delay filter with delay $\hat{v}n\sin(\theta_i)/c$, which can be translated into a phase shift at the carrier frequency as $\omega_c\hat{v}n\sin(\theta_i)/c$. Thus, equation (5.33) can now take the form

$$\hat{\boldsymbol{R}}_{ss}(\omega_c) = \frac{1}{N}\sum_{n=0}^{N-1} \begin{bmatrix} 1 & e^{j\omega_c\hat{v}nT_s(\sin(\theta_1)-\sin(\theta_2))/c} \\ e^{-j\omega_c\hat{v}nT_s(\sin(\theta_1)-\sin(\theta_2))/c} & 1 \end{bmatrix} \tag{5.34}$$

A simple measure of decorrelation (γ) is the ratio of the combined off-diagonal power in comparison to the power on the main diagonal. This can be expressed as a function of the total number of samples as

$$\begin{aligned}\gamma_1(N) &= \frac{1}{2N}\sum_{n=0}^{N-1}\left[e^{j\omega_c\hat{v}nT_s(\sin(\theta_1)-\sin(\theta_2))/c} + e^{-j\omega_c\hat{v}nT_s(\sin(\theta_1)-\sin(\theta_2))/c}\right] \\ &= \frac{1}{2N}\sum_{n=0}^{N-1} 2\cos\left(\omega_c\hat{v}nT_s(\sin(\theta_1)-\sin(\theta_2))/c\right)\end{aligned} \tag{5.35}$$

This can be further simplified as

$$\begin{aligned}\gamma_1(N) &= \frac{1}{2N}\frac{2\sin(\omega_c\hat{v}(N-1)T_s(\sin(\theta_1)-\sin(\theta_2))/c)}{\omega_c\hat{v}T_s(\sin(\theta_1)-\sin(\theta_2))/c} \\ &= \frac{\sin(\omega_c\hat{v}(N-1)T_s(\sin(\theta_1)-\sin(\theta_2))/c)}{NT_s\omega_c\hat{v}(\sin(\theta_1)-\sin(\theta_2))/c}\end{aligned} \tag{5.36}$$

Assuming N is sufficiently large that $N-1 \approx N$, then (5.36) can be simplified rather elegantly as a sinc function

$$\gamma(N) \approx \text{sinc}(NT_s\omega_c\hat{v}(\sin(\theta_1)-\sin(\theta_2))/c) \tag{5.37}$$

This closed form expression can now be used to analyse the minimum number of samples, integration time or overall distance to achieve a certain level of decorrelation for specific scenarios. To illustrate this, Figure 5.8 uses an example of a scenario whereby the sampling rate of the receiver is set to 1 GHz and the array is moving in a lateral motion at a velocity of 340 m/s.

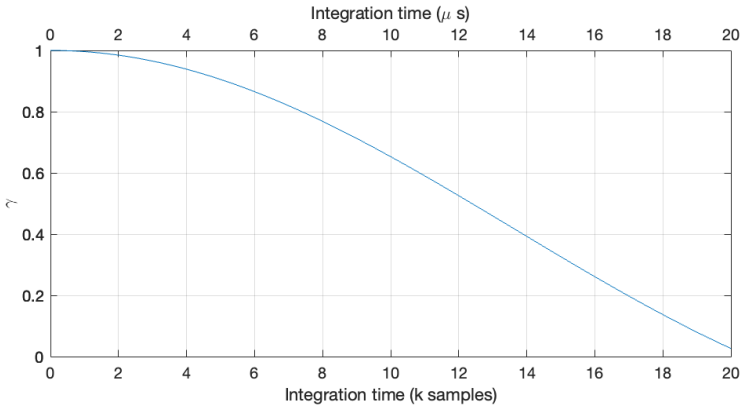

Figure 5.8: Decorrelation Factor as a function of Integration time

Figure 5.8 shows the sinc function approaching its first zero crossing after an integration time of 20 k samples or 20 μs. 50% decorrelation of emitters is achieved after about 12uS. In spite of this being a relatively long integration time, decorrelation of the emitter pulses can be achieved, providing that the emitter pulse length is at least this integration time. However, the pulse length of the emitter may not be known before the measurement. Thus, it is useful to understand the minimum pulse length that can be decorrelated through this Doppler smoothing scheme.

An important metric to consider is the first crossing of the sinc function in (5.37), as this will guarantee at least 79% source decorrelation because the magnitude of the sinc function remains below 0.21 past this point. The first zero crossing point appears at

$$N_0 = \frac{c}{NT_s\omega_c\hat{v}|\sin(\theta_1) - \sin(\theta_2)|} \tag{5.38}$$

If the minimum integration time is defined at the first zero crossing point, then the minimum integration time can be expressed as a function of angular separation. If the emitters lie on either side of the array boresight, then the minimum integration time (in samples) can be expressed as

$$N_0(\delta\theta) = \frac{c}{NT_s\omega_c\hat{v}2\sin(\delta\theta/2)} \tag{5.39}$$

Figure 5.9 shows the minimum integration time as a function of angular separation for two coherent sources at a carrier frequency of 10 GHz, a receiving platform velocity of 340 m/s and a sampling frequency of 1 GHz. As expected, closely spaced sources will have similar Doppler shifts, and thus, will require a much longer integration time than well-separated emitters. [1]

[1]The analysis in this section assumes a constant velocity. This is an appropriate assumption for the time scales discussed here. In the example presented, the array would have travelled a total of 6.8 mm over $20\mu s$ during the acquisition

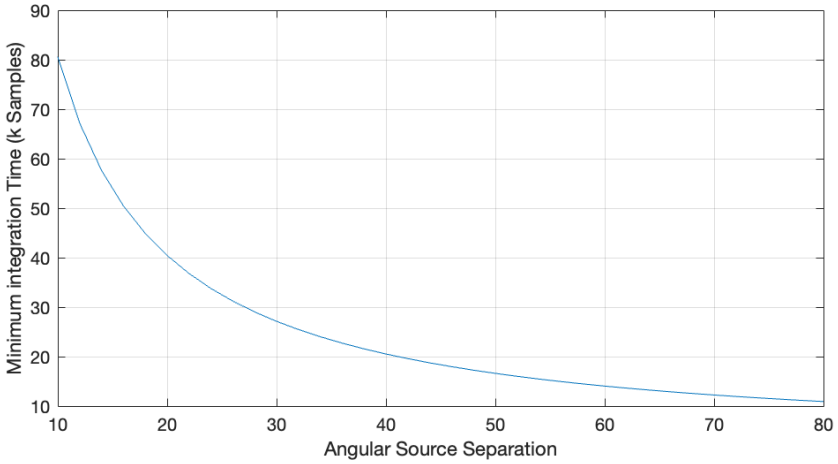

Figure 5.9: Minimum Integration Time as a Function of Angular Separation

5.3.1 Summary

In summary, an array in motion can induce angle dependent Doppler shifts in coherent emitters. Under certain circumstances, this is sufficient to completely decorrelate coherent sources by effectively performing spatial smoothing naturally while calculating a space-time covariance matrix. Through analysis of a basic scenario, it can be seen that integration times required are fairly long (in the order of 10's of microseconds). This implies that the pulse width needs to be at least the required integration time if the emitter is pulsed. However, as discussed in Chapter 2, LPI waveforms tend to be spread in time and this translates into long pulses, or even into CW waveforms. Thus, for the waveforms of interest, the minimum pulse length becomes less of an issue.

5.4 Conclusion

This Chapter has explored the problem of estimating the direction of arrival of strongly correlated sources, and presented novel methods to effectively decorrelate sources. For a linear array, the conventional spatial smoothing method can be applied to polynomial space-time covariance matrices as an effective means for the decorrelation broadband sources. A proof was provided demonstrating the minimum number of subarrays require to decorrelate emitters. While effective, such a method does come at the cost of a

reduced effective aperture, reducing the maximum number of emitters that can be resolved.

In order to avoid aperture reduction to decorrelate emitters, an analytical study was performed to determine whether the motion of a fast moving platform could be exploited to decorrelate the emitters. Results determined that such an approach is possible when considering very long integration times, and is thus, unsuitable for short pulses. However, this is less of an issue for broadband CW LPI emitters.

Chapter 6

DoA Estimation of LPI Sources via Advanced Array Geometries and Polynomial Matrix Methods

6.1 Introduction

In order to detect and locate sources over a wide operating bandwidth, wide-band antennas and subsequent analog and digital signal processing circuitry is required. Such components are expensive in both monetary and power costs. Thus, physical size, weight, cost and power requirements of the receivers may be a limiting factor in the number of array elements within an aperture. Setting the element spacing to half the wavelength of the highest operating frequency for an unambiguous angle resolution at all frequencies could result in an electrically small aperture, which in turn could cause a relativity poor angular resolution. Moreover, close element spacing will result in greater mutual coupling in the array, degrading performance. Both these issues are exacerbated at the lower operating frequencies. In summary, fine element spacing is required for unambiguous angular resolution at the higher end of the frequency range, and a large overall aperture is required for sufficient resolution at lower frequencies.

In this chapter, sparse array geometries are explored and novel signal processing methods are presented in an effort to form hole-free para-hermitian polynomial space-

time covariance matrices from sparse arrays. The advanced array signal processing methods developed in Chapters 4 and 5 are leveraged in this chapter to form novel techniques. Simulations are presented to demonstrate the enhanced performance of these sparse arrays in terms of accuracy and resolution for DoA estimation of broadband LPI sources.

6.2 Sparse Linear Arrays

When designing a linear antenna array, one of the key considerations is the spatial resolution, which is determined by the electrical size of the aperture. Another important aspect is the number of elements and their location within the aperture. For example, one could design an array of two elements spaced several wavelengths apart. This would provide good spatial resolution, however, this would also produce many 'spatial aliases' as this is essentially undersampling in the spatial domain. Alternatively, populating the array in a uniform manner, where the elements are spaced at the spatial Nyquist sampling distance ($\lambda/2$), would produce the same fine spatial resolution with no spatial aliases - but would require a significant increase in array elements. The next logical step would be to populate the array in a non-uniform or 'sparsely populated' fashion. Thus, a significant amount of research has been undertaken in the last few decades to form frameworks and methods to optimise sensor placement. Previous work in this area is discussed in more detail in Chapter 3. This section does not propose new sparse array geometries, but instead focuses on novel signal processing techniques for such geometries.

Consider a set of N sensors placed on a uniform grid of spacing $d = \lambda_{min}/2$, where λ_{min} is the wavelength of the highest frequency source anticipated - satisfying the spatial Nyquist sampling criterion and ensuring unambiguous DoA estimation. The sensor x_n is physically located at nd from the first sensor in the array. The difference set contains all $2N-1$ differences of the element pairs in the array, and is defined as

$$\mathcal{M} = \{x_i - x_j\}, \forall i, j = 0, 1, \ldots, N-1 \tag{6.1}$$

The significance of this difference set is that it defines the spatial lag, for which second order statistics can be estimated under wide sense stationary conditions. This arises naturally when estimating a spatial covariance matrix:

$$\begin{aligned}\boldsymbol{R}_{xx}(\tau) &= E[\boldsymbol{x}(n)\boldsymbol{x}^H(n-\tau)] \\ &= \begin{bmatrix} \sigma_{11}^2(\tau) & \sigma_{21}^2(\tau) & \sigma_{31}^2(\tau) & \dots & \sigma_{N1}^2(\tau) \\ \sigma_{12}^2(\tau) & \sigma_{22}^2(\tau) & \sigma_{32}^2(\tau) & \dots & \vdots \\ \sigma_{13}^2(\tau) & \sigma_{23}^2(\tau) & \sigma_{33}^2(\tau) & \dots & \sigma_{NN}^2(\tau) \end{bmatrix}\end{aligned} \tag{6.2}$$

where n is the discrete time index, and τ is the discrete lag parameter.

As an example, consider a 3 element sparse array, where the elements are located at $0, 1$ and 3 times d. This array geometry can be seen in Figure 6.1.

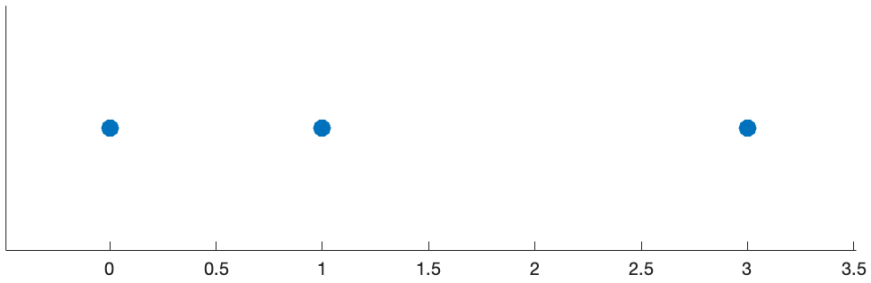

Figure 6.1: Example Sparse Array

The difference set of this array is

$$\mathcal{M} = \{-3, -2, -1, 0, 0, 0, 1, 2, 3\} \tag{6.3}$$

An important aspect of the difference set is the weight function $w(u)$. The weight function of a sparse array is defined as the number of times the difference u occurs within its difference set. If the same difference, u, occurs more than once, i.e. $w(u) > 1$, then it is said to be *redundant*. From 6.3, there are 3 occurrences of 0, thus $w(0) = 3$, and there are no redundancies elsewhere, i.e. $w(u) = 1$ for $u \neq 0$. This can be seen graphically in Figure 6.2. Note that, for any N element array geometry, $w(0) = N$. The example array is actually a special case of a zero redundancy array, as there is only one combination by which each non-zero point can be achieved in the difference set.

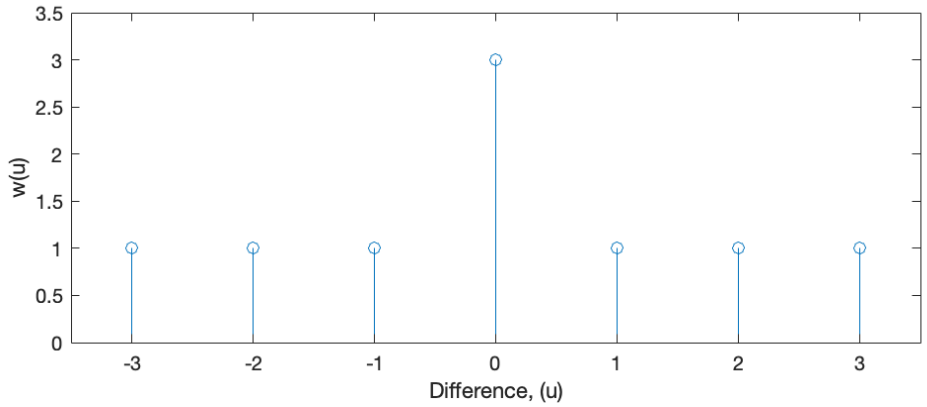

Figure 6.2: Weight function of the example sparse array

In section 6.3, the redundancies within the weight function will be further explored and exploited to improve the performance of the algorithms discussed in this chapter.

6.2.1 Minimum Redundancy Array

A class of linear arrays were shown in [80], where they achieve maximum spatial resolution for a given number of elements by minimizing the redundancies in the difference set. Whilst the original scope of [80] is for radio astronomy, the aim of detecting and locating faint distant sources is very similar to an ES problem.

It is worth noting that the case of the zero redundancy array is the goal of a minimum redundancy array (MRA). However, such an array does not exist for more than 4 elements [87]. Calculating the sensor locations of an MRA is not a trivial task as closed form expressions for estimating sensor locations do not exist. However, look up tables and examples are provided in [80] and some methods can be found in [79]. This chapter only considers the case of a restricted array, in which the difference set fills the holes in the entire array aperture. An example of an 8 element minimum redundancy array is provided in Figure 6.3 and its weight function in Figure 6.4b. There is also no closed form expression for the maximum number of sources such an array can resolve with subspace methods. However, in the example provided, it is shown that the 8 element restricted minimum redundancy array can resolve a maximum of 23 sources since a 24 element virtual uniform linear array is generated in later processing stages.

6.2.2 Nested, and Super Nested Array

In comparison to the minimum redundancy array, it is trivial to calculate the sensor positions for a nested array. It is the union of two uniform linear arrays; a Nyquist spaced (d) array with N_1 elements, and a sparse uniform linear array of N_2 sensors spaced at $(N_1 + 1)d$, over an aperture of $N_2(N_1 + 1)d$, yielding a sparse array with $N_1 + N_2$ sensors overall, with the ability to resolve $N_2(N_1 + 1) - 1$ sources. An 8 element ($N_1 = N_2 = 4$) nested array is shown in Figure 6.3, and its weight function in Figure 6.4c. Unlike a co-prime array [90], a nested array yields a contiguous difference set, akin to the restricted class of MRAs [116]. While such an array is easy to design, in general, its weight function contains more redundancies than an MRA. Another major drawback to the conventional nested array is the issue of mutual coupling between sensors of the dense Nyquist portion of the array.

Recently, the super-nested array was proposed in [86, 91], which aims to reduce the effect of mutual coupling in the array by redistributing the dense portion of the array across the entire aperture. The goal of the second order super-nested array is to minimise the pairs spaced at Nyquist, i.e. the $w(1) = 1$, which will reduce the effect of mutual coupling substantially. A third order super nested array also minimises the pairs spaced at 2 Nyquist. The weight function of an 8 element second order super nested array is shown in Figure 6.4d, and demonstrates that while there is the same redundancy as the conventional nested array, the number of pairs spaced at Nyquist ($u = \pm 1$) is reduced from 4 to 2.

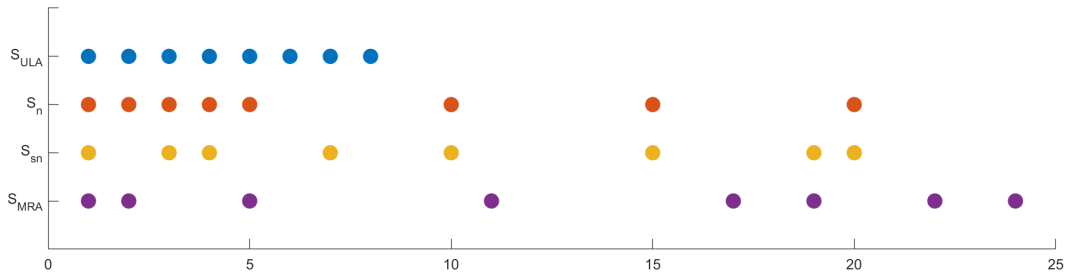

Figure 6.3: Physical Array Geometries for the uniform linear-, nested-, super nested- and minimum redundancy arrays

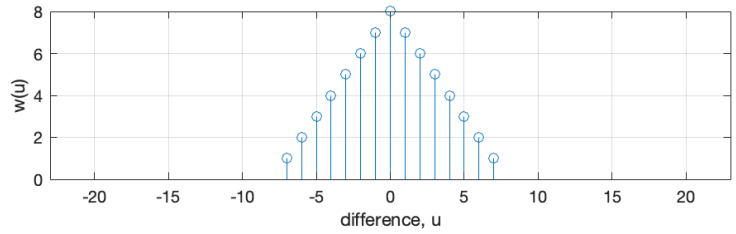

(a) Weight function for an 8 element ULA

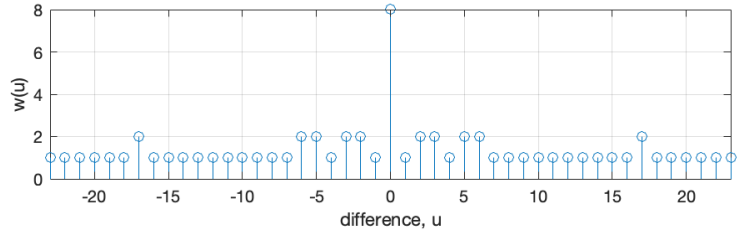

(b) Weight function for an 8 Element Minimum Redundancy Array

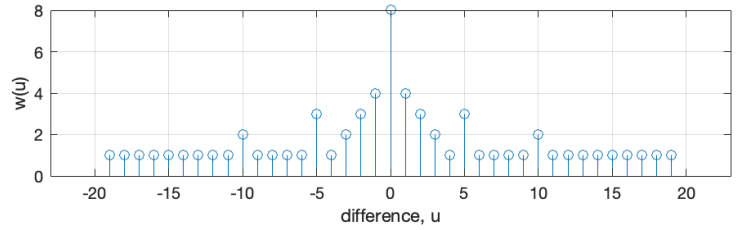

(c) Weight function for a $N_1 = N_2 = 4$ Nested Array

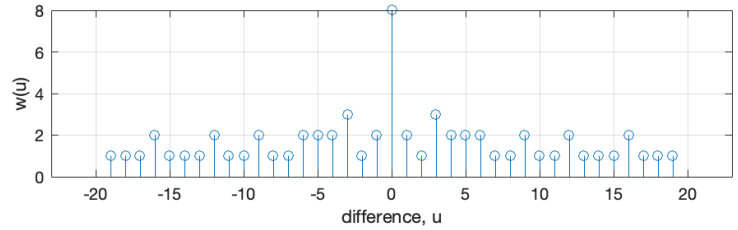

(d) Weight function for a $N_1 = N_2 = 4$ Second Order Super-Nested Array

Figure 6.4: Array Weight Functions

6.3 Formation of Virtual Covariance Matrices

Recall the analytical model for the polynomial space-time covariance matrix:

$$\boldsymbol{R}_{xx}(z) = \boldsymbol{A}(z)\tilde{\boldsymbol{R}}_{ss}(z)\boldsymbol{A}^{P}(z) + \sigma_{\nu}^{2}\boldsymbol{I} \tag{6.4}$$

It can be rewritten in summation form as:

$$\boldsymbol{R}_{xx}(z) = \sum_{L}^{l=1}[\sigma_l^2(z)a_l(z)a_l^P(z)] + \sigma_\nu^2\boldsymbol{I} \tag{6.5}$$

Following the definition of the difference set that was given in (6.1), it is important to note the elements of the polynomial covariance matrix contain all spatial differences from this set. Thus, the component $\langle \boldsymbol{R}_{xx}(z)\rangle_{ij}$ represents the spatial auto- (for $i = j$) and cross-(for $i \neq j$) correlations for spatial difference $i-j$. By vectorising this matrix, a virtual array is generated with positions contained in the difference set:

$$\boldsymbol{\gamma}(z) = \text{vec}(\boldsymbol{R}_{xx}(z)) \tag{6.6}$$

A worked example of this is presented in Appendix B. Using the summation form from (6.5), this can be rewritten as

$$\boldsymbol{\gamma}(z) = \text{vec}\left[\sum_{l=1}^{L}[\sigma_l^2(z)\boldsymbol{a}_l(z)\boldsymbol{a}_l^P(z)]\right] + \sigma_\nu^2\tilde{\mathbf{1}} \tag{6.7}$$

Here, $\tilde{\mathbf{1}}$ is the vectorised identity matrix that is a vector of zeros with ones at $N+1$ intervals, corresponding to the diagonal, auto-correlation components of $\boldsymbol{R}_{xx}(z)$. Clearly, the first term can be rewritten in matrix form to give something analogous to the original sensor model of (4.16):

$$\boldsymbol{\gamma}(z) = \boldsymbol{B}(z)\boldsymbol{\sigma}^2(z) + \sigma_\nu^2\tilde{\mathbf{1}} \tag{6.8}$$

where $\boldsymbol{\sigma}^2(z)$ is a vector of source autocorrelation functions, and

$$\boldsymbol{B}(z) = [\boldsymbol{a}_1(z) \odot \boldsymbol{a}_1^*(z^{-1}), \ldots, \boldsymbol{a}_L(z) \odot \boldsymbol{a}_L^*(z^{-1})] \tag{6.9}$$

represents the steering vector for the much larger virtual array of sensor data pairs, covering all the sensor displacement in the difference set $\mathcal{M}$, and $\odot$ represents the Kronecker product. This representation contains redundancies as spelt out in the weight functions of the difference set, as introduced in section (2). In particular, for all the sparse arrays of section (2) there is an N-fold redundancy of the zero displacement

auto-correlation terms.

The arrays in (6.8) can be truncated to eliminate the redundancies. Assuming each element is corrupted by some zero mean i.i.d. noise process, then instead of simply removing the redundant elements, they can be averaged to enhance the estimate of the virtual ULA and in the process reducing the N^2 size of $\boldsymbol{\gamma}(z)$ to the $(2M-1)$ element ULA:

$$\boldsymbol{\gamma}_1(z) = \boldsymbol{A}_1(z)\boldsymbol{\sigma}^2(z) + \sigma_\nu^2\tilde{\boldsymbol{e}} \tag{6.10}$$

Here, $\tilde{\boldsymbol{e}}$ is a vector of zeros, except a 1 at the array position zero. From Chapter 4, it was noted that

- The rows of the steering vectors are just powers of the primitive (Nyquist) steering element, i.e. $a_{nl}(z)$, the n^{th} row of the l^{th} source steering vector is:

$$a_{nl}(z) = a_{1l}(z)^{m_n} \tag{6.11}$$

- The parahermitian conjugate of a steering vector is just the inverse of a steering vector:

$$a_{nl}^*(z^{-1}) = a_{nl}(z)^{-1} = a_{1l}(z)^{-m_n} \tag{6.12}$$

Reordering the rows of $\boldsymbol{B}(z)$ so that the differences are in order of increasing sensor displacement and then, using the known steering vector structure summarised in (6.11) and (6.12), it is possible to obtain the virtual array steering vector in the rationalised form characterised by the Vandermonde structure:

$$\boldsymbol{A}_1(z) = \begin{bmatrix} a_{11}^{-M+1}(z) & a_{12}^{-M+1}(z) & \dots & a_{1L}^{-M+1}(z) \\ a_{11}^{-M+2}(z) & a_{12}^{-M+2}(z) & \dots & a_{1L}^{-M+2}(z) \\ \vdots & \vdots & \ddots & \vdots \\ 1 & 1 & \dots & 1 \\ \vdots & \vdots & \ddots & \vdots \\ a_{11}^{M-2}(z) & a_{12}^{M-2}(z) & \dots & a_{1L}^{M-2}(z) \\ a_{11}^{M-1}(z) & a_{12}^{M-1}(z) & \dots & a_{1L}^{M-1}(z) \end{bmatrix} \tag{6.13}$$

Having condensed and reordered (6.8), $\boldsymbol{A}_1(z)$ now has precisely the structure of a conventional ULA steering vector. Additionally, the model expressed in (6.10) is almost identical in structure to that of the ULA summarised in (4.16). With that in mind, the next step is to construct the quadratic form:

$$\boldsymbol{\gamma}_1(z)\boldsymbol{\gamma}_1^P(z) = \boldsymbol{A}_1(z)\boldsymbol{\sigma}^2(z)\boldsymbol{\sigma}^{2\ P}(z)\boldsymbol{A}_1^P(z) + \sigma_\nu^4\tilde{\boldsymbol{e}}\tilde{\boldsymbol{e}}^P \tag{6.14}$$

Not surprisingly, this has a similar form as the covariance in (6.4). However, it can be noted that since the source matrix is simply the outer product of two vectors, the source matrix $(\boldsymbol{\sigma}^2(z)\boldsymbol{\sigma}^{2\ P}(z))$ is seriously rank deficient; being rank 1, irrespective of the number of sources. Moreover, the noise term is also of rank 1, since $\tilde{\boldsymbol{e}}$ and $\tilde{\boldsymbol{e}}^P$ are also just column and row vectors respectively, each being zero except for a single 1 at the zero displacement element. Thus, despite the familiar form, (6.14) is not a representation that enables the usual forms of quadratic signal analysis. Nevertheless, the situation can be recovered as described in the next section.

6.3.1 Rank Recovery by Spatial Smoothing

In Chapter 5, a novel broadband decorrelation technique was introduced through the spatial averaging of polynomial space-time covariance matrices. In this approach, applicable to uniform linear arrays, a new array is constructed by taking a shortened sub-array and forming the average of this array with the translations of it. In general, averaging over just L such subarrays is sufficient to increase the rank to L, allowing L sources to be resolved.

In [117], it was demonstrated that forming M overlapping subarrays of M elements could restore the rank of (6.14). It was also suggested that this step was required in order to restore the rank of the source covariance matrix. While this is true, the spatial smoothing theory states that the above requires only L subarrays to restore the rank of this matrix, rather than M subarrays. However, in reality, it is true that M subarrays are required to achieve a valid space-time covariance matrix. Consequently, (6.14) not only exhibits a singular source matrix, but the noise is also singular. Since more sensors than sources are assumed ($L < M$), it is necessary to form an M-dimensional subarray, obtained as the average of its M possible translations in order to remove both singularities.

Starting with the shortened array defined by the M-dimensional steering vector, $\boldsymbol{A}_0(z)$ is given as the lowest M rows of $\boldsymbol{A}_1(z)$ in (6.13). The M translations of this uniform linear array are:

$$\boldsymbol{\gamma}_i(z) = \boldsymbol{A}_0(z)\boldsymbol{Q}^{-i+1}(z)\boldsymbol{\sigma}^2(z) + \sigma_\nu^2 \tilde{\boldsymbol{e}}_i \tag{6.15}$$

where $\boldsymbol{Q}(z)$ is the diagonal matrix,

$$\boldsymbol{Q}(z) = \begin{bmatrix} a_{11}(z) & & & \\ & a_{12}(z) & & \\ & & \ddots & \\ & & & a_{1L}(z) \end{bmatrix} \tag{6.16}$$

and $\tilde{\boldsymbol{e}}_i$ is a vector of zeros apart from a single 1 at array index i.

Finally, the covariance of this spatially-smoothed, M-dimensional, virtual uniform linear array can now be formed as:

$$\boldsymbol{R}_{xx}(z) = \frac{1}{M}\sum_{i=1}^{M} \boldsymbol{\gamma}_i(z)\boldsymbol{\gamma}_i^P(z) \tag{6.17}$$

Inserting (20), the full structure of this virtual array covariance is obtained:

$$\boldsymbol{R}_{xx}(z) = \boldsymbol{A}_0(z)\hat{\boldsymbol{R}}_{ss}(z)\boldsymbol{A}_0^P(z) + \frac{1}{M}\sigma_\nu^4\boldsymbol{I} \tag{6.18}$$

where

$$\hat{\boldsymbol{R}}_{ss}(z) = \frac{1}{M}\sum_{m=1}^{M}\boldsymbol{Q}^{-i+1}(z)\boldsymbol{\sigma}^2(z)\boldsymbol{\sigma}^{2\ P}(z)\boldsymbol{Q}^{-i+1\ P}(z) \tag{6.19}$$

The additional phase terms in the vector outer-product terms ensure incoherent summation that restores the source covariance matrix rank, as can be proved, just as in [118]. It is also easy to see that the translational shift in the summation, steps the single 1 along the noise matrix diagonal; restoring it to full rank as well. Thus $\boldsymbol{I}$ in (6.18) is just the M-dimensional identity matrix.

6.4 Performance Analysis

In this section, combined with the novel techniques presented in Chapters 4 and 5, the performance of the above methods is demonstrated and analysed. In all the simulation scenarios, the case of uncorrelated sources and a perfectly calibrated 8 element array is considered. The PEVD algorithm used is the SMD method [104]. Section 6.4.1 demonstrates the powerful ability of estimating a spatio-spectrum of several spectrally overlapping, spatially close broadband sources using uniform linear-, super-nested, and minimum redundancy arrays. Section 6.4.2 analyses the accuracy of the Root spatio-spectrum estimator when used in conjunction with the array geometries discussed; and demonstrates the benefit of redundancy averaging. Finally, Section 6.4.3 shows the empirical resolution of the three array geometries.

6.4.1 Detection & Spatio-Spectrum Estimation

Six temporally overlapping triangular FMCW waveforms of varying carrier frequencies and bandwidths, linearly spaced between $-35°$ and $35°$ are present, with an acquisition period of $N_s = 20000$ samples. Table 6.1 shows the ground truth for all simulated sources, and Table 6.2 shows the receiver properties.

Table 6.1: Source Parameters

Source No.	Carrier Frequency (GHz)	Bandwidth (GHz)	DoA (°)
1	10	2	$\theta = -35$
2	9.5	2	$\theta = -21$
3	9.5	2.5	$\theta = -7$
4	10.5	1.3	$\theta = 7$
5	10	2.1	$\theta = 21$
6	9.9	1.9	$\theta = 35$

Table 6.2: Receiver Parameters

Sampling Frequency	4 GS/s
Instantaneous Bandwidth	4 GHz
Centre Frequency	10 GHz
Acquisition Period	5 μs
Acquisition Samples	20000
SNR	10 dB
Number of Channels	8

Recall that the polynomial eigenvalues are representative of a power spectral density, and this is used to determine the dimensions of the signal and noise subspaces. Figure 6.5 shows the eigenvalue power spectral densities (PSD) for this simulation. Note only the first 8 eigenvalues are displayed for the minimum redundancy array and super nested array. From these figures, it can be seen that there are 6 significant eigenvalues, and thus 6 uncorrelated spectrally overlapping sources present. Separating the noise subspace, the spatio-spectrum polynomial MUSIC algorithm from Chapter 4 is used to estimate the spatio-spectrum. Figure 6.6 shows the estimated spatio-spectrum via uniform linear, super nested, and minimum redundancy arrays. A normalised 1D projection (spatial) of these can be seen in Figure 6.6d. It is easy to see that all array geometries correctly estimate both, the frequency/bandwidth and direction of arrival of all sources present. However, results are clearer in the case of sparse arrays due to the increased resolution offered by the much larger aperture. While these examples give a vague idea on performance, the subsequent simulations analyse the statistical performance in terms of both estimator variance, and resolution.

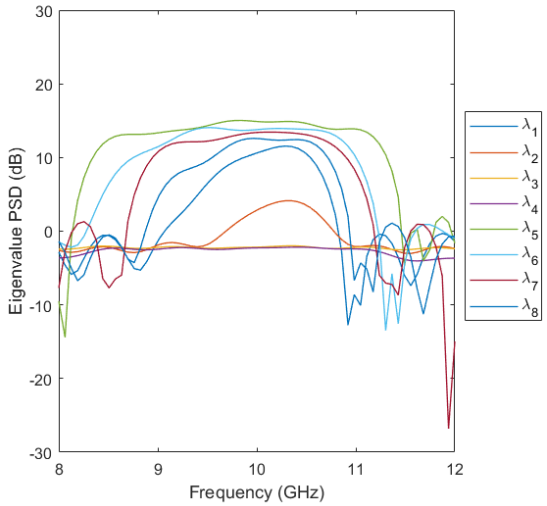

(a) Uniform Linear Array

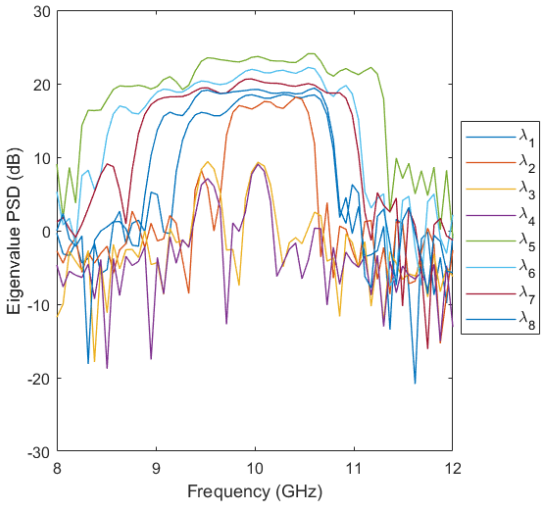

(b) Super Nested array (First 8/20 eigenvalues displayed)

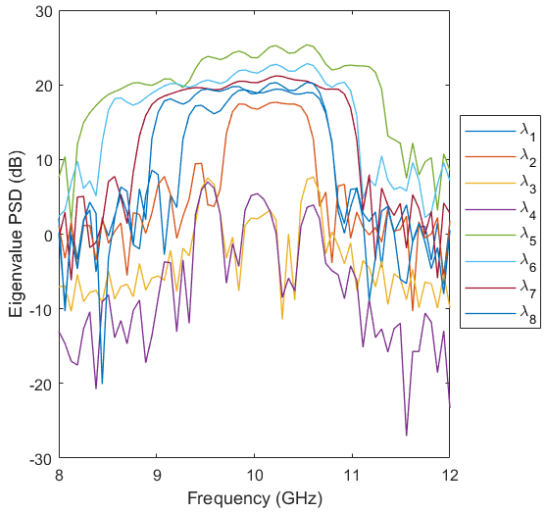

(c) Minimum Redundancy array (First 8/24 eigenvalues displayed)

Figure 6.5: Frequency domain representation of the polynomial eigenvalues in the case of the three array geometries

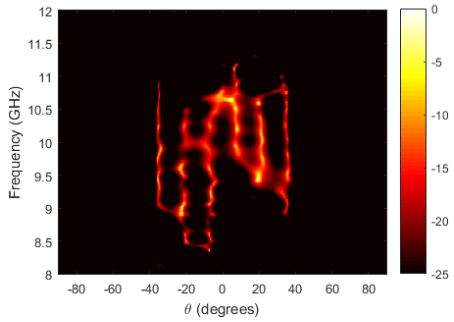

(a) An 8 element Uniform Linear array

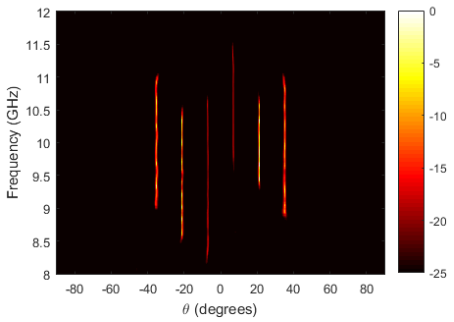

(b) An 8 element Minimum Redundancy Array

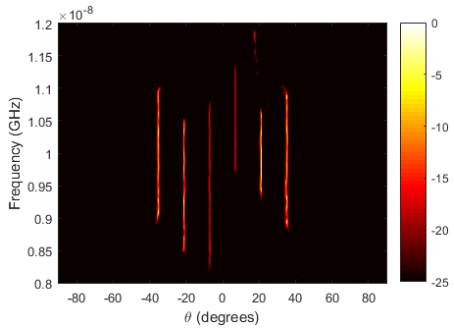

(c) Spatio-Spectrum Estimation of 6 broadband FMCW sources using an 8 element Super Nested Array

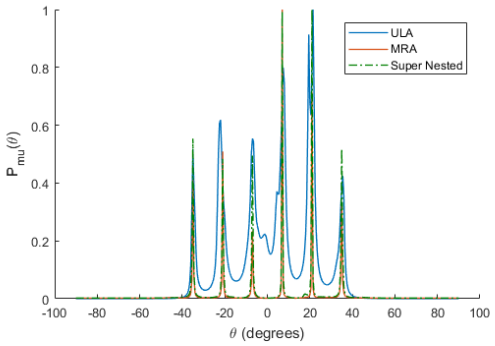

(d) A spatial only comparison of the polynomial MUSIC algorithm when used in conjunction with the three array geometries

Figure 6.6: Spatio-Spectrum Estimation of 6 broadband FMCW sources

6.4.2 Accuracy

In this section, simulation results are presented to compare the direction of arrival estimation variance across a range of signal to noise ratios. A Monte-Carlo simulation was performed, using $I = 500$ runs for each SNR, with fixed bandwidths and randomised DoAs for each run. The novel Root Polynomial MUSIC algorithm (introduced in Chapter 4) is used for improved computation times. In [118], it was noted that the statistical performance was largely the same as the heuristic searching method in Section 6.4.1. Since this is an unbiased estimator, the estimator variance, σ_E^2 is simply calculated as the mean squared error, i.e.

$$\sigma_E^2 = \frac{1}{I}\sum_{i=1}^{I}[\tilde{\theta}_i - \theta]^2 \tag{6.20}$$

where $\tilde{\theta}_i$ is the estimated DoA, and θ is the ground truth. Figure 6.7 shows the simulated performance of root polynomial MUSIC algorithms for the three array geometries without redundancy averaging. Results demonstrate that for a fixed number of antenna elements, the sparse array geometries have an improved performance over a uniform linear array. It is to be expected that the Minimum Redundancy array should perform better than the super nested array due to the greater degrees of freedom offered, and this is verified in Figure 6.7. The effect of redundancy averaging on the variance can be seen in Figure 6.8. This averaging has a clear improvement in estimator accuracy, and intuitively, this has a greater effect on the super nested array as this array geometry has more redundancies in its weight function.

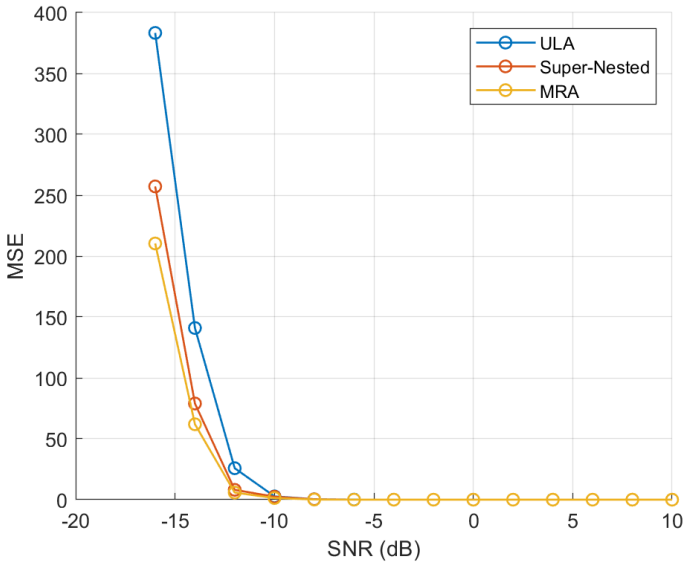

Figure 6.7: Root PMUSIC estimator variance for the three array geometries in the case of the three array geometries: Redundancies are discarded

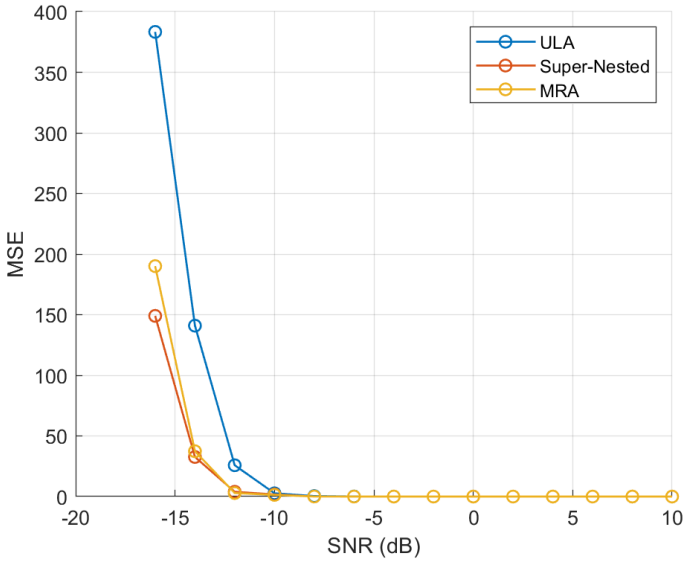

Figure 6.8: Root PMUSIC estimator variance for the three array geometries in the case of the three array geometries: With redundancy averaging

6.4.3 Probability of Resolution

Since the methods proposed in section 6.4.1 are super-resolution, the resolution is not bound by the Rayleigh criterion. In this section, a Monte-Carlo simulation of 100 runs is performed to analyse the empirical probability of resolving two sources spaced at $\Delta\theta = \theta_1 - \theta_2$ by using the spatial only function of the Polynomial MUSIC algorithm [119]

$$P_{mu}(\theta) = \sum_{i=N_{\omega L}}^{N_{\omega H}} P_{SSP}(\theta, e^{j\omega_i}) \tag{6.21}$$

where $N_{\omega L}$ and $N_{\omega H}$ are the indexes of the frequency bins containing sufficient energy and can be determined experimentally. Rather than considering the full shape of this spatial-only spectrum, in this separability issue, the following inequality is used to determine whether a pair of sources are resolved:

$$P_{mu}\left(\frac{\theta_1 + \theta_2}{2}\right) \leq \frac{1}{2}[P_{mu}(\theta_1) + P_{mu}(\theta_2)] \tag{6.22}$$

At the point $P_{mu}(\frac{\theta_1+\theta_2}{2}) = 0$, the peaks merge into one, and the DoAs will not be resolved. The probability of a single run is calculated as

$$P_r(\Delta\theta) = \begin{cases} 1 & \text{if } P_{mu}(\frac{\theta_1+\theta_2}{2}) \leq \frac{1}{2}[P_{mu}(\theta_1) + P_{mu}(\theta_2)] \\ 0 & \text{otherwise} \end{cases} \tag{6.23}$$

Resolution analysis was performed with two FMCW sources centred at 10 GHz, with 2 GHz bandwidth. Two scenarios are simulated - one where the received signals have equal power, and another where there is a 10 dB difference. The received SNR was set to 15 dB and the redundancy averaging method was used for the formation of the space-time covariance matrices.

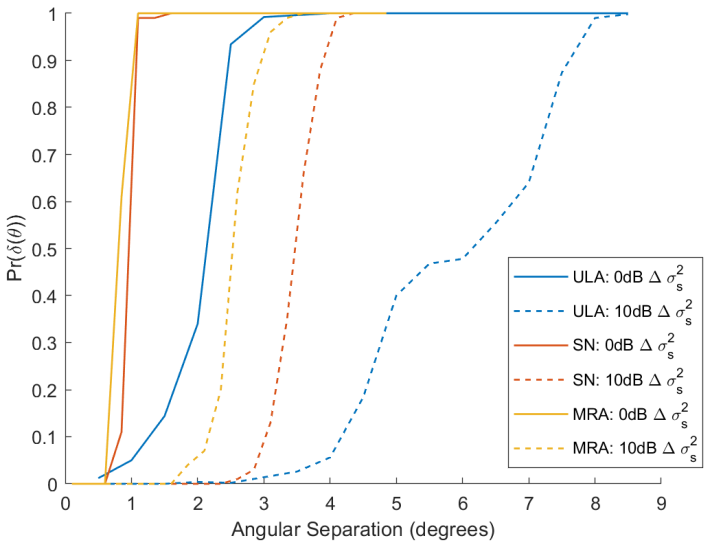

Figure 6.9: Probability of resolution for the three array geometries. Solid lines represent equal power of the two sources. Dashed represents a 10 dB difference in source power

Figure 6.9 shows the simulated probability of resolution over a range of angular separations. It can be noted that the sparse methods perform considerably better in both scenarios. In the case of equal power sources, both the minimum redundancy, and super nested arrays demonstrate sub 1 degree resolution, as opposed to the 2 degrees seen from the ULA. In the case of a 10 dB power difference between the sources, the resolution improvement using sparse arrays is further improved over the ULA. More interestingly, there is now a greater difference between the minimum redundancy and super-nested arrays, demonstrating how the increased degrees of freedom translates into a greater angular resolving power. While all of the arrays have an equal number of elements, it is expected that the sparse methods improve upon performance not only due to the increased aperture, but also due to the increased degrees of freedom. Since the minimum redundancy array has greater freedoms compared to the super nested array, this increase in performance is expected.

6.5 Summary

In this Chapter, the polynomial matrix approach to spatio-temporal array signal processing developed in Chapters 3 and 4 were applied to modern sparse array theory. Analysis demonstrated that the generated virtual array polynomial covariance matrix would be singular due to the singular noise covariance matrix. This problem was overcome via the polynomial spatial smoothing method presented in Chapter 5. Results demonstrated that sparse arrays used in conjunction with polynomial matrix methods provide an elegant and promising solution for DoA estimation of broadband LPI emitters.

To demonstrate the presented methods, a simulated scenario of several LPI FMCW emitters was generated. While all the methods correctly estimated the frequency and angle of arrival of the emitters, it was clear from Figure 6.6 that the sparse arrays offered a considerable benefit in terms of resolution. To formally compare the accuracy and resolution for each of the array topologies for LPI FMCW emitters, Monte-Carlo simulations were performed to calculate estimator variance and probability of resolution. It was also demonstrated that by using the older method of generating a restricted sparse array, the minimum redundancy array generally out performs the more modern super-nested array due to the larger electrical length of the array and thus greater degrees of freedom generated. The effect of redundancy averaging further improves accuracy of the estimators by enhancing the estimate of the polynomial space-time covariance matrices.

Chapter 7

Conclusions

With the electromagnetic spectrum becoming evermore congested, and the emerging radar technology actively reducing its probability of being intercepted, the detection and characterisation of radar signals is becoming evermore difficult. Due to advances in solid state RF technology, modern emitters are agile in both, the time and frequency domains. Thus, it is now important to continue to discover new techniques and algorithms to deal with these issues. Upon studying existing literature, it was found that methods based on time-frequency analysis could achieve a significant processing gain. However, given the fact that modern emitters can be agile, time and frequency estimations alone may be insufficient to resolve different emitters. One domain where an emitter cannot be agile (within a pulse duration) is the spatial domain.

In this thesis, there is a strong focus on novel spatial processing techniques to develop an enabling technology for electronic surveillance systems to cope with a congested electromagnetic environment as well as aid in the detection and localisation of low probability of intercept radars. Popular literature on spatial processing, however, focuses on narrowband scenarios, which are incompatible with broadband LPI emitters. Existing literature on broadband array signal processing problems is limited in comparison to the narrowband super-resolution techniques. However, recent advances such as polynomial matrices and the polynomial eigenvalue decomposition provide an attractive solution for broadband array processing problems, and these have been leveraged throughout Chapters 4 through 6 in this thesis.

In Chapter 4, a novel multi-correlation receiver was proposed. Through analysis and a series of example problems, it was demonstrated that a multi-correlation receiver concept is capable of outperforming conventional Fourier analysis for LPI waveforms. In addition, a novel algorithm to estimate a spatio-spectrum with a significantly reduced computational cost was proposed, and Monte-Carlo simulations demonstrated a reduction in computation time with no sacrifice to performance.

Chapter 5 focussed on novel solutions for the direction of arrival estimation of strongly correlated, or even coherent sources. One novel solution included the spatial averaging technique, which demonstrated a significant improvement in spatial resolution in the extreme case of coherent sources. Chapter 5 also provided a novel analysis of exploiting the Doppler effect to decorrelate emitters, which is a naturally arising phenomenon for an array in motion. It was concluded that for a fast-moving array (around 340 m/s), the aforementioned spatial smoothing effect happens while estimating a covariance matrix, and thus no further processing was required to decorrelate the emitters. The caveat, however, is that relatively long integration times were required to effectively decorrelate emitters.

Chapter 6 studied the problem of optimal sensor placement for wideband antenna arrays. When designing a wideband antenna array, closely spaced sensors are required to achieve ambiguity-free DoA estimates of the higher frequency emitters, while a long overall aperture is required for sufficient resolution at lower frequencies. For a uniform linear array, this would result in an array with many elements, making such an array a particularly inefficient design. Chapter 6 also introduced novel signal processing techniques to exploit sparse array geometries for broadband scenarios via polynomial matrices. Simulation results demonstrated a significant improvement in DoA resolution and accuracy, compared to a ULA of the same number of elements.

The techniques presented throughout this thesis have the potential for real-world use. Although the material developed was for application in passive sensing of the electromagnetic spectrum, other domains could also exploit the presented techniques. For example, passive sonar arrays, microphone arrays and arrays of ultrasonic transducers, which typically deal with broadband signals, can also find the techniques described in

this thesis useful to enhance DoA estimation.

While the simulation results presented demonstrate an enhanced performance over conventional methods, there is a significant amount of work required to mature the techniques, to be able to leverage them for real-world applications. It could be argued that the largest obstacle to implementing polynomial matrix techniques in real-time is the computational cost associated with it. Reducing the computational cost is not a simple task, but there are now a plethora of options available for optimising and deploying algorithms onto hardware, such as GPUs, FPGAs, SoCs, and CPUs. Other future work in this area could involve closer coupling between the spatio-spectral techniques presented in this thesis, and the time-frequency distributions presented in the existing literature. Such a technique could be used to provide unique time-frequency-space distributions for enhanced 'imaging' of the emitters.

To conclude, this thesis has made a significant contribution to the knowledge in areas of broadband array signal processing and low probability of intercept radar detection and localisation. Novel techniques were presented and backed up by analytical techniques and numerical simulations.

Appendix A

Down Converted Array Signal Model Derivation

Given a signal, $s(t)$, where we expect it to have spectral content around some carrier (angular) frequency close to ω_d, we will generally want to remove this high frequency content prior to digitisation. This is just to reduce the signal bandwidth to allow the sampling to rate to be reduced to a value not much more than Nyquist for the underlying signal bandwidth, stripping of its carrier.

Thus if we imagine the signal captured with both I and Q components then the down-converted signal will be $x(t)$, where:

$$x(t) = s(t)e^{-j\omega_d t} \tag{A.1}$$

For any sensor array intercepting such a signal, the arrival times with be element-dependent but a common down-conversion will be used. Indeed it will be important to ensure a phase coherent local oscillator is used across the array.
Thus, for an array with elements 'i, we will have the down-converted components:

$$x_i(t) = s(t - \tau_i)e^{-j\omega_d t} \tag{A.2}$$

For signal processing of such signals it is convenient to express the separate elements all in terms of a common reference (that will invariably be a particular element chosen

in that array). Therefore we write:

$$x_i(t) = [\delta(t - \tau_i) \otimes s(t)]e^{-j\omega_d t} \tag{A.3}$$

where δ is the Dirac 'delta-function' and $\otimes$ is the convolution operator so that:

$$\delta(t) \otimes s(t) \equiv \int_{-\infty}^{\infty} \delta(t - t')s(t')dt' \tag{A.4}$$

Thus, we can write:

$$\begin{aligned}
[\delta(t - \tau_i) \otimes s(t)]e^{-j\omega_d t} &= \int_{-\infty}^{\infty} \delta(t - t' - \tau_i)s(t')dt'e^{-j\omega_d t} \\
&= \int_{-\infty}^{\infty} \delta(t - t' - \tau_i)e^{j\omega_d t'}s(t')e^{-j\omega_d t'}dt'e^{-j\omega_d t} \\
&= \int_{-\infty}^{\infty} \delta(t - t' - \tau_i)e^{j\omega_d t'}e^{-j\omega_d t}e^{j\omega_d \tau_i}s(t')e^{-j\omega_d t'}dt'e^{-j\omega_d \tau_i} \\
&= \int_{-\infty}^{\infty} \delta(t - t' - \tau_i)e^{-j\omega_d (t-t'-\tau_i)}e^{-j\omega_d \tau_i}s(t')e^{-j\omega_d t'}dt'
\end{aligned} \tag{A.5}$$

Now $\delta(t - t' - \tau_i)$ is zero everywhere other than where $t - t' - \tau_i = 0$, while:

$$e^{-j\omega_d (t-t'-\tau_i)}|_{t-t'-\tau_i=0} = 1 \tag{A.6}$$

Thus, the down-converted array elements can be rewritten as:

$$\begin{aligned}
x_i(t) &= [\delta(t - \tau_i) \otimes s(t)]e^{-j\omega_d t} \\
&= \int_{-\infty}^{\infty} \delta(t - t' - \tau_i)e^{-j\omega_d \tau_i}s(t')e^{-j\omega_d t'}dt' \\
&= [\delta(t - \tau_i)e^{-j\omega_d \tau_i}] \otimes [s(t)e^{-j\omega_d t}]
\end{aligned} \tag{A.7}$$

Appendix B

Worked Example of the Virtual ULA Generation Step

Consider a 3 element MRA, with sensors located at positions $0, 1, 3$. The weight function of such an array is $[-3, -2, -1, 0, 0, 0, 1, 2, 3]$. The steering vector for such an array takes the form of

$$\boldsymbol{a}(z) = \begin{bmatrix} \psi^0(z) \\ \psi^1(z) \\ \psi^3(z) \end{bmatrix} \tag{B.1}$$

where $\psi(z)$ is a fractional delay filter of delay τ_d, where this delay is induced due to the direction of arrival (as explored in Chapter 4). The space time covariance matrix for a single source can be expressed as

$$\boldsymbol{R}_{xx}(z) = \sigma_s^2(z)\boldsymbol{a}(z)\boldsymbol{a}^P(z) + \sigma_\nu^2\boldsymbol{I} \tag{B.2}$$

Thus, the structure of the space time covariance matrix of the 3 element MRA is

$$\begin{aligned}\boldsymbol{R}_{xx}(z) &= \sigma_s^2(z)\begin{bmatrix}\psi^0(z)\psi^0(z) & \psi^1(z)\psi^0(z) & \psi^3(z)\psi^0(z)\\ \psi^0(z)\psi^{-1}(z) & \psi^1(z)\psi^{-1}(z) & \psi^3(z)\psi^{-1}(z)\\ \psi^0(z)\psi^{-3}(z) & \psi^1(z)\psi^{-3}(z) & \psi^3(z)\psi^{-3}(z)\end{bmatrix} + \sigma_\nu^2\boldsymbol{I}\\ &= \sigma_s^2(z)\begin{bmatrix}\psi^0 & \psi^1(z) & \psi^3(z)\\ \psi^{-1}(z) & \psi^0(z) & \psi^2(z)\\ \psi^{-3}(z) & \psi^{-2}(z) & \psi^0(z)\end{bmatrix} + \sigma_\nu^2\begin{bmatrix}1 & 0 & 0\\ 0 & 1 & 0\\ 0 & 0 & 1\end{bmatrix}\end{aligned} \tag{B.3}$$

Note that in (6.11) and (6.12) it was identified that the time reversed conjugate of a fractional delay filter is simply its inverse, (i.e. ψ^1(z) is a fractional delay filter of τ_d, and ψ^{-1}(z) is a fractional delay filter of $-\tau_d$). Vectorising (B.3) yields:

$$\begin{aligned}\boldsymbol{\gamma}(z) &= \text{vec}(\boldsymbol{R}_{xx}(z))\\ &= \sigma_s^2(z)\begin{bmatrix}\psi^0\\ \psi^1(z)\\ \psi^3(z)\\ \psi^{-1}(z)\\ \psi^0(z)\\ \psi^2(z)\\ \psi^{-3}(z)\\ \psi^{-2}(z)\\ \psi^0(z)\end{bmatrix} + \sigma_\nu^2\begin{bmatrix}1\\0\\0\\0\\1\\0\\0\\0\\1\end{bmatrix}\end{aligned} \tag{B.4}$$

Note the above quantity is similar to that in (6.10). Following the same logic as Chapter 6, this vector can be rearranged and redundancies can be removed to produce virtual array:

$$\boldsymbol{\gamma}_1(z) = \sigma_s^2(z) \begin{bmatrix} \psi^{-3} \\ \psi^{-2}(z) \\ \psi^{-1}(z) \\ \psi^{0}(z) \\ \psi^{1}(z) \\ \psi^{2}(z) \\ \psi^{3}(z) \end{bmatrix} + \sigma_\nu^2 \begin{bmatrix} 0 \\ 0 \\ 0 \\ 1 \\ 0 \\ 0 \\ 0 \end{bmatrix} \tag{B.5}$$

This equation is now similar to that of a 7-element uniform linear array with a vandermonde structured steering vector. The next step is to perform the spatial smoothing step outlined in 6.3.1.

Bibliography

[1] J.-C. Souyris, *The Physics of Radar Measurement.* John Wiley Sons, Ltd, 2014, ch. 4, pp. 83–122. [Online]. Available: https://onlinelibrary.wiley.com/doi/abs/10.1002/9781118899106.ch4

[2] M. A. Richards, W. A. Holm, and J. A. Scheer, *Principles of Modern Radar, Basic Principles.* Scitech Publishing, 2010.

[3] W. L. Melvin and J. A. Scheer, *Principles of Modern Radar, Advanced Techniques.* Scitech Publishing, 2013.

[4] "Aveillant," Oct 2020. [Online]. Available: https://www.aveillant.com/

[5] R. A. Poisel, *Electronic Warfare Receivers and Receiving Systems.* Artech House, 2014.

[6] M. Khalaf-Allah, "Emitter location with azimuth and elevation measurements using a single aerial platform for electronic support missions," *Sensors*, vol. 21, no. 12, 2021. [Online]. Available: https://www.mdpi.com/1424-8220/21/12/3946

[7] P. E. Pace, *Radar Range-Performance Analysis.* Artech House, 1986.

[8] P. E. Pace, *Detecting and Classifying Low Probability of Intercept Radar.* Artech House, 2008.

[9] M. R. Sarker, M. M. Islam, M. T. Alam, and M. Hossam-E-Haider, "Side lobe level reduction in antenna array using weighting function," in *2014 International Conference on Electrical Engineering and Information Communication Technology*, 2014, pp. 1–5.

[10] T. Taylor, "Design of line-source antennas for narrow beamwidth and low side lobes," *Transactions of the IRE Professional Group on Antennas and Propagation*, vol. 3, no. 1, pp. 16–28, 1955.

[11] T. Taylor, "Design of circular apertures for narrow beamwidth and low sidelobes," *IRE Transactions on Antennas and Propagation*, vol. 8, no. 1, pp. 17–22, 1960.

[12] R. Hansen, "A one-parameter circular aperture distribution with narrow beamwidth and low sidelobes," *IEEE Transactions on Antennas and Propagation*, vol. 24, no. 4, pp. 477–480, 1976.

[13] Y. Dai, Y. Liu, and Z. Zhang, "A design of low side-lobe slot array antenna at k-band," in *Proceedings of 2014 3rd Asia-Pacific Conference on Antennas and Propagation*, 2014, pp. 171–172.

[14] D. E. Lawrence, "Low probability of intercept antenna array beamforming," *IEEE Transactions on Antennas and Propagation*, vol. 58, no. 9, pp. 2858–2865, 2010.

[15] W.-Q. Wang, "Potential transmit beamforming schemes for active lpi radars," *IEEE Aerospace and Electronic Systems Magazine*, vol. 32, no. 5, pp. 46–52, 2017.

[16] K. Chen, S. Yang, Y. Chen, D. Yang, M. Huang, S.-W. Qu, and J. Hu, "Lpi beamforming based on 4-d antenna arrays with pseudorandom time modulation," *IEEE Transactions on Antennas and Propagation*, vol. 68, no. 3, pp. 2068–2077, 2020.

[17] H. Li, Y. Chen, and S. Yang, "Low probability of interception beamforming in single-sideband time-modulated antenna arrays," in *2021 International Applied Computational Electromagnetics Society (ACES-China) Symposium*, 2021, pp. 1–2.

[18] "Scout mk3 - medium range covert surveillance radar." [Online]. Available: https://www.thalesgroup.com/en/scout-mk3-medium-range-covert-surveillance-radar

[19] K. Kim and J.-A. Lee, "M-hop interception of fh/lpi signals using autocorrelation techniques," in *Fourth IEEE Region 10 International Conference TENCON*, 1989, pp. 266–269.

[20] T. Huynh-The, V.-S. Doan, C.-H. Hua, Q.-V. Pham, T.-V. Nguyen, and D.-S. Kim, "Accurate lpi radar waveform recognition with cwd-tfa for deep convolutional network," *IEEE Wireless Communications Letters*, vol. 10, no. 8, pp. 1638–1642, 2021.

[21] Y. Liu, P. Xiao, H. Wu, and W. Xiao, "Lpi radar signal detection based on radial integration of choi-williams time-frequency image," *Journal of Systems Engineering and Electronics*, vol. 26, no. 5, pp. 973–981, 2015.

[22] T. Wan, K. li Jiang, H. Ji, and B. Tang, "Deep learning-based lpi radar signals analysis and identification using a nyquist folding receiver architecture," *Defence Technology*, 2021. [Online]. Available: https://www.sciencedirect.com/science/article/pii/S2214914721001835

[23] M. A. Govoni, H. Li, and J. A. Kosinski, "Low probability of interception of an advanced noise radar waveform with linear-fm," *IEEE Transactions on Aerospace and Electronic Systems*, vol. 49, no. 2, pp. 1351–1356, 2013.

[24] Q. Yang, Y. Zhang, and X. Gu, "Design of ultralow sidelobe chaotic radar signal by modulating group delay method," *IEEE Transactions on Aerospace and Electronic Systems*, vol. 51, no. 4, pp. 3023–3035, 2015.

[25] K. Olsen, T. Johnsen, S. Johnsrud, R. Gundersen, H. Bjordal, I. Tansem, and P. Sornes, "Results from an experimental continuous wave low probability of intercept bistatic radar - the first steps toward multistatic radar," in *2003 Proceedings of the International Conference on Radar (IEEE Cat. No.03EX695)*, 2003, pp. 288–292.

[26] H. Godrich, A. P. Petropulu, and H. V. Poor, "Power allocation strategies for target localization in distributed multiple-radar architectures," *IEEE Transactions on Signal Processing*, vol. 59, no. 7, pp. 3226–3240, 2011.

[27] P. Chavali and A. Nehorai, "Scheduling and power allocation in a cognitive radar network for multiple-target tracking," *IEEE Transactions on Signal Processing*, vol. 60, no. 2, pp. 715–729, 2012.

[28] H. Gao, J. Wang, and X. Zhang, "Resource allocation in mimo radar with widely separated antennas for multi-target detection," in *2014 International Radar Conference*, 2014, pp. 1–6.

[29] V. Krishnamurthy, "Emission management for low probability intercept sensors in network centric warfare," *IEEE Transactions on Aerospace and Electronic Systems*, vol. 41, no. 1, pp. 133–151, 2005.

[30] D. Liu, F. Wang, C. Shi, and J. Zhang, "Lpi based optimal power and dwell time allocation for radar network system," in *2016 CIE International Conference on Radar (RADAR)*, 2016, pp. 1–5.

[31] Tezel and Ozkazanc, "Methods for analysis of lpi radar signals," in *2006 IEEE 14th Signal Processing and Communications Applications*, 2006, pp. 1–4.

[32] W. Pei and T. Bin, "Detection and estimation of non-cooperative uniform pulse position modulated radar signals at low snr," in *2013 International Conference on Communications, Circuits and Systems (ICCCAS)*, vol. 2, 2013, pp. 214–217.

[33] W. Tao, J. Kaili, L. Jingyi, J. Tingting, and T. Bin, "Research on lpi radar signal detection and parameter estimation technology," *Journal of Systems Engineering and Electronics*, vol. 32, no. 3, pp. 566–572, 2021.

[34] S. Xiong and Y. Wu, "The detection of transient signals based on gabor transform," in *2006 8th international Conference on Signal Processing*, vol. 1, 2006.

[35] P. R. Milne and P. E. Pace, "Wigner distribution detection and analysis of fmcw and p-4 polyphase lpi waveforms," in *2002 IEEE International Conference on Acoustics, Speech, and Signal Processing*, vol. 4, 2002, pp. IV–3944–IV–3947.

[36] B. Hamschin, J. Clancy, M. Grabbe, M. Fortier, and J. Novak, "Passive detection, characterization, and localization of multiple lfmcw lpi signals," in *2014 IEEE Radar Conference*, 2014, pp. 0537–0543.

[37] Y. Wu and X. Li, "Elimination of cross-terms in the wigner–ville distribution of multi-component lfm signals," *IET Signal Processing*, vol. 11, no. 6, pp. 657–662, 2017. [Online]. Available: https://ietresearch.onlinelibrary.wiley.com/doi/abs/10.1049/iet-spr.2016.0358

[38] D. Ping, P. Zhao, and B. Deng, "Cross-terms suppression in wigner-ville distribution based on image processing," in *The 2010 IEEE International Conference on Information and Automation*, 2010, pp. 2168–2171.

[39] C. J. Gaikwad and P. Sircar, "Bispectrum-based technique to remove cross-terms in quadratic systems and wigner–ville distribution," *Signal, Image and Video Processing*, vol. 12, no. 4, pp. 703–710, 2018. [Online]. Available: https://doi.org/10.1007/s11760-017-1211-7

[40] S. Barbarossa and A. Zanalda, "A combined wigner-ville and hough transform for cross-terms suppression and optimal detection and parameter estimation," in *[Proceedings] ICASSP-92: 1992 IEEE International Conference on Acoustics, Speech, and Signal Processing*, vol. 5, 1992, pp. 173–176 vol.5.

[41] F. G. Geroleo and M. Brandt-Pearce, "Detection and estimation of lfmcw radar signals," *IEEE Transactions on Aerospace and Electronic Systems*, vol. 48, no. 1, pp. 405–418, 2012.

[42] F. G. Geroleo, M. Brandt-Pearce, and C. L. Brown, "Detection and estimation of multi-pulse lfmcw radar signals," in *2010 IEEE Radar Conference*, 2010, pp. 1009–1013.

[43] T. O. Gulum, A. Erdogan, K. K. Guner, L. Durak-Ata, T. Yildirim, and P. E. Pace, "Pwvd resolution considerations for lfmcw signal detection by wht," in *2014 20th International Conference on Microwaves, Radar and Wireless Communications (MIKON)*, 2014, pp. 1–4.

[44] A. Erdogan, T. O. Gulum, L. Durak-Ata, T. Yildirim, and P. E. Pace, "Digital chirp rate adaptation for increased fmcw interception performance in hough based transforms," in *2014 International Radar Conference*, 2014, pp. 1–5.

[45] K. K. Guner, B. Erkmen, T. O. Gulum, A. Y. Erdogan, T. Yıldırım, and L. Durak Ata, "Implementation aspects of wigner-hough transform based detectors for lfmcw signals," in *2016 39th International Conference on Telecommunications and Signal Processing (TSP)*, 2016, pp. 441–444.

[46] K. K. Guner, T. O. Gulum, and B. Erkmen, "Fpga-based wigner–hough transform system for detection and parameter extraction of lpi radar lfmcw signals," *IEEE Transactions on Instrumentation and Measurement*, vol. 70, pp. 1–15, 2021.

[47] S. Li, D. Quan, X. Wang, and X. Jin, "Lpi radar signal modulation recognition with feature fusion based on time- frequency transforms," in *2021 13th International Conference on Wireless Communications and Signal Processing (WCSP)*, 2021, pp. 1–6.

[48] D. Stevens and S. Schuckers, "A novel approach for the characterization of fsk low probability of intercept radar signals via application of the reassignment method," in *2014 IEEE Military Communications Conference*, 2014, pp. 783–787.

[49] R. Ardoino and A. Megna, "Lpi radar detection: Snr performances for a dual channel cross-correlation based esm receiver," in *2009 European Radar Conference (EuRAD)*, 2009, pp. 113–116.

[50] X. Tang, B. Jiang, C. Zhang, and Y. He, "Detection and parameter estimiation of lpi signals in passive radar," in *2006 CIE International Conference on Radar*, 2006, pp. 1–4.

[51] F. Hejazi, Y. Norouzi, and M. M. Nayebi, "Sar processing to localize lpi radars," in *2014 International Radar Conference*, 2014, pp. 1–4.

[52] R. C. Hansen, *Phased Array Antennas*. Wiley, 2010.

[53] R. L. Haupt, *Antenna Arrays: A Computational Approach*. Wiley, 2010.

[54] J. Capon, "High-resolution frequency-wavenumber spectrum analysis," *Proceedings of the IEEE*, vol. 57, no. 8, pp. 1408–1418, Aug 1969.

[55] D. H. Johnson, *Array Signal Processing*. Pearson, 1993.

[56] C.-Y. Chen and P. P. Vaidyanathan, "Quadratically constrained beamforming robust against direction-of-arrival mismatch," *IEEE Transactions on Signal Processing*, vol. 55, no. 8, pp. 4139–4150, 2007.

[57] R. Schmidt, "Multiple emitter location and signal parameter estimation," *IEEE Trans. Antennas and Propagation*, vol. 34, no. 3, pp. 276–280, Mar 1986.

[58] P. Vallet, X. Mestre, and P. Loubaton, "Performance analysis of an improved music doa estimator," *IEEE Transactions on Signal Processing*, vol. 63, no. 23, pp. 6407–6422, Dec 2015.

[59] A. L. Swindlehurst and T. Kailath, "A performance analysis of subspace-based methods in the presence of model errors. i. the music algorithm," *IEEE Transactions on Signal Processing*, vol. 40, no. 7, pp. 1758–1774, July 1992.

[60] M. Kaveh and A. Barabell, "The statistical performance of the music and the minimum-norm algorithms in resolving plane waves in noise," *IEEE Transactions on Acoustics, Speech, and Signal Processing*, vol. 34, no. 2, pp. 331–341, April 1986.

[61] R. Kumaresan and D. W. Tufts, "Estimating the angles of arrival of multiple plane waves," *IEEE Transactions on Aerospace and Electronic Systems*, vol. AES-19, no. 1, pp. 134–139, Jan 1983.

[62] X. Jing and Z. C. Du, "An improved fast root-music algorithm for doa estimation," in *2012 International Conference on Image Analysis and Signal Processing*, Nov 2012, pp. 1–3.

[63] M. Pesavento, A. Gershman, and M. Haardt, "Unitary root-music with a real-valued eigendecomposition: a theoretical and experimental performance study," *IEEE Transactions on Signal Processing*, vol. 48, no. 5, pp. 1306–1314, 2000.

[64] M. V. Athi and S. A. Zekavat, "Real-time root-music doa estimation via a parallel polynomial rooting method," in *2014 IEEE 25th Annual International Symposium on Personal, Indoor, and Mobile Radio Communication (PIMRC)*, 2014, pp. 290–295.

[65] K. V. Rangarao and S. Venkatanarasimhan, "gold-music: A variation on music to accurately determine peaks of the spectrum," *IEEE Transactions on Antennas and Propagation*, vol. 61, no. 4, pp. 2263–2268, April 2013.

[66] B. D. Rao and K. V. S. Hari, "Performance analysis of root-music," *IEEE Transactions on Acoustics, Speech, and Signal Processing*, vol. 37, no. 12, pp. 1939–1949, Dec 1989.

[67] F. Belloni, A. Richter, and V. Koivunen, "Doa estimation via manifold separation for arbitrary array structures," *IEEE Transactions on Signal Processing*, vol. 55, no. 10, pp. 4800–4810, Oct 2007.

[68] M. Rubsamen and A. B. Gershman, "Direction-of-arrival estimation for nonuniform sensor arrays: From manifold separation to fourier domain music methods," *IEEE Transactions on Signal Processing*, vol. 57, no. 2, pp. 588–599, Feb 2009.

[69] Q. Liu, F. Yan, Y. Han, S. Liu, and M. Jin, "Reduced-order root-music based on schur spectral factorization," in *2016 IEEE International Conference on Ubiquitous Wireless Broadband (ICUWB)*, 2016, pp. 1–3.

[70] R. Roy and T. Kailath, "Esprit-estimation of signal parameters via rotational invariance techniques," *IEEE Transactions on Acoustics, Speech, and Signal Processing*, vol. 37, no. 7, pp. 984–995, Jul 1989.

[71] B. Ottersten, M. Viberg, and T. Kailath, "Performance analysis of the total least squares esprit algorithm," *IEEE Transactions on Signal Processing*, vol. 39, no. 5, pp. 1122–1135, 1991.

[72] T.-J. Shan, M. Wax, and T. Kailath, "On spatial smoothing for direction-of-arrival estimation of coherent signals," *IEEE Trans. Acoustics, Speech, and Signal Processing*, vol. 33, no. 4, pp. 806–811, Aug 1985.

[73] J. E. Evans, J. R. Johnson, and D. F. Sun, "Application of advanced signal processing techniques to angle of arrival estimation in atc navigation and surveillance system," *DTIC Document, Technical Report*, 1982.

[74] S. U. Pillai and B. H. Kwon, "Forward/backward spatial smoothing techniques for coherent signal identification," *IEEE Trans. Acoustics, Speech, and Signal Processing*, vol. 37, no. 1, pp. 8–15, Jan 1989.

[75] R. T. Williams, S. Prasad, A. K. Mahalanabis, and L. H. Sibul, "An improved spatial smoothing technique for bearing estimation in a multipath environment," *IEEE Trans. Acoustics, Speech, and Signal Processing*, vol. 36, no. 4, pp. 425–432, Apr 1988.

[76] T. T. Vo, L. Ouvry, A. Sibille, and S. Bories, "Mutual coupling modeling and calibration in antenna arrays for aoa estimation," in *2018 2nd URSI Atlantic Radio Science Meeting (AT-RASC)*, 2018, pp. 1–4.

[77] B. Yu, C. Yin, and Y. Huang, "Calibration method for mutual coupling between elements based on parallel genetic algorithm," in *2006 6th World Congress on Intelligent Control and Automation*, vol. 1, 2006, pp. 3490–3493.

[78] E. Langley, C. Fulton, and M. Yeary, "Analysis of mutual coupling algorithms for a dipole array," in *2021 IEEE International Conference on Microwaves, Antennas, Communications and Electronic Systems (COMCAS)*, 2021, pp. 326–329.

[79] J. Leech, "On the representation of 1, 2,..., n by differences," *Journal of the London Mathematical Society*, vol. s1-31, no. 2, pp. 160–169, 1956. [Online]. Available: https://londmathsoc.onlinelibrary.wiley.com/doi/abs/10.1112/jlms/s1-31.2.160

[80] A. Moffet, "Minimum-redundancy linear arrays," *IEEE Transactions on Antennas and Propagation*, vol. 16, no. 2, pp. 172–175, March 1968.

[81] R. Z. Syeda, T. G. Savelyev, M. C. van Beurden, and A. B. Smolders, "Sparse mimo array for improved 3d mm- wave imaging radar," in *2020 17th European Radar Conference (EuRAD)*, 2021, pp. 342–345.

[82] J. K. Schindler and H. Steyskal, "Transmit beamforming and waveforms for random, sparse array radar," in *2004 International Waveform Diversity Design Conference*, 2004, pp. 1–5.

[83] Y. Xu and Y. Lu, "Sparse composite array with enhanced angular resolution for automotive radar applications," in *2021 IEEE International Symposium on Antennas and Propagation and USNC-URSI Radio Science Meeting (APS/URSI)*, 2021, pp. 1947–1948.

[84] I. Prudyus and L. Lazko, "Sparse antenna array geometry synthesis for remote sensing systems," in *2008 International Conference on "Modern Problems of Radio Engineering, Telecommunications and Computer Science" (TCSET)*, 2008, pp. 333–333.

[85] S.-J. Wei, X.-L. Zhang, and J. Shi, "Compressed sensing linear array sar 3-d imaging via sparse locations prediction," in *2014 IEEE Geoscience and Remote Sensing Symposium*, 2014, pp. 1887–1890.

[86] C. Liu and P. P. Vaidyanathan, "Super nested arrays: Sparse arrays with less mutual coupling than nested arrays," in *2016 IEEE International Conference on Acoustics, Speech and Signal Processing (ICASSP)*, March 2016, pp. 2976–2980.

[87] R. Bracewell and G. Swarup, "The stanford microwave spectroheliograph antenna, a microsteradian pencil beam interferometer," *IRE Transactions on Antennas and Propagation*, vol. 9, no. 1, pp. 22–30, January 1961.

[88] P. Pal and P. P. Vaidyanathan, "Coprime sampling and the music algorithm," *2011 Digital Signal Processing and Signal Processing Education Meeting, DSP/SPE 2011 - Proceedings*, vol. 0, no. 1, pp. 289–294, 2011.

[89] P. P. Vaidyanathan and P. Pal, "Sparse SensingWith Co-Prime Samplers and Arrays," *IEEE Transactions on Signal Processing*, vol. 59, no. 2, pp. 1405–1409, 2010.

[90] P. Pal and P. P. Vaidyanathan, "Coprime sampling and the music algorithm," in *2011 Digital Signal Processing and Signal Processing Education Meeting (DSP/SPE)*, Jan 2011, pp. 289–294.

[91] C. Liu and P. P. Vaidyanathan, "High order super nested arrays," in *2016 IEEE Sensor Array and Multichannel Signal Processing Workshop (SAM)*, July 2016, pp. 1–5.

[92] H. Wang and M. Kaveh, "Coherent signal-subspace processing for the detection and estimation of angles of arrival of multiple wide-band sources," *IEEE Transactions on Acoustics, Speech, and Signal Processing*, vol. 33, no. 4, pp. 823–831, August 1985.

[93] G. Bienvenu, "Eigensystem properties of the sampled space correlation matrix," in *ICASSP '83. IEEE International Conference on Acoustics, Speech, and Signal Processing*, vol. 8, April 1983, pp. 332–335.

[94] M. Coker and E. Ferrara, "A new method for multiple source location," in *ICASSP '82. IEEE International Conference on Acoustics, Speech, and Signal Processing*, vol. 7, May 1982, pp. 411–415.

[95] Guaning Su and M. Morf, "The signal subspace approach for multiple wide-band emitter location," *IEEE Transactions on Acoustics, Speech, and Signal Processing*, vol. 31, no. 6, pp. 1502–1522, December 1983.

[96] P. Pal and P. P. Vaidyanathan, "A novel autofocusing approach for estimating directions-of-arrival of wideband signals," in *2009 Conference Record of the Forty-*

Third Asilomar Conference on Signals, Systems and Computers, Nov 2009, pp. 1663–1667.

[97] M. A. Alrmah, S. Weiss, and S. Lambotharan, "An extension of the music algorithm to broadband scenarios using a polynomial eigenvalue decomposition," in *2011 EUSIPCO*, Aug 2011, pp. 629–633.

[98] M. A. Alrmah, J. Corr, A. Alzin, K. Thompson, and S. Weiss, "Polynomial subspace decomposition for broadband angle of arrival estimation," in *2014 Sensor Signal Processing for Defence (SSPD)*, Sep. 2014, pp. 1–5.

[99] S. Weiss, S. Bendoukha, A. Alzin, F. K. Coutts, I. K. Proudler, and J. Chambers, "Mvdr broadband beamforming using polynomial matrix techniques," in *2015 23rd European Signal Processing Conference (EUSIPCO)*, Aug 2015, pp. 839–843.

[100] S. Weiss, M. Alrmah, S. Lambotharan, J. G. McWhirter, and M. Kaveh, "Broadband angle of arrival estimation methods in a polynomial matrix decomposition framework," in *2013 5th IEEE International Workshop on Computational Advances in Multi-Sensor Adaptive Processing (CAMSAP)*, Dec 2013, pp. 109–112.

[101] A. Ahrens and S. Lochmann, "Polynomial matrix algorithms for broadband optical mimo systems," in *2016 Advances in Wireless and Optical Communications (RTUWO)*, Nov 2016, pp. 22–27.

[102] A. Sandmann, A. Ahrens, and S. Lochmann, "Evaluation of polynomial matrix svd-based broadband mimo equalization in an optical multi-mode testbed," in *2017 Advances in Wireless and Optical Communications (RTUWO)*, Nov 2017, pp. 1–11.

[103] J. G. McWhirter, P. D. Baxter, T. Cooper, S. Redif, and J. Foster, "An evd algorithm for para-hermitian polynomial matrices," *IEEE Trans. Signal Processing*, vol. 55, no. 5, pp. 2158–2169, May 2007.

[104] S. Redif, S. Weiss, and J. G. McWhirter, "Sequential matrix diagonalization algorithms for polynomial evd of parahermitian matrices," *IEEE Trans. Signal Processing*, vol. 63, no. 1, pp. 81–89, Jan 2015.

[105] J. Corr *et al.*, "Multiple shift maximum element sequential matrix diagonalisation for parahermitian matrices," in *2014 IEEE Workshop on Statistical Signal Processing (SSP)*, June 2014, pp. 312–315.

[106] F. K. Coutts, K. Thompson, I. K. Proudler, and S. Weiss, "Restricted update sequential matrix diagonalisation for parahermitian matrices," in *2017 IEEE 7th International Workshop on Computational Advances in Multi-Sensor Adaptive Processing (CAMSAP)*, Dec 2017, pp. 1–5.

[107] F. K. Coutts, J. Corr, K. Thompson, S. Weiss, I. K. Proudler, and J. G. McWhirter, "Memory and complexity reduction in parahermitian matrix manipulations of pevd algorithms," in *2016 24th European Signal Processing Conference (EUSIPCO)*, Aug 2016, pp. 1633–1637.

[108] S. Kasap and S. Redif, "Novel field-programmable gate array architecture for computing the eigenvalue decomposition of para-hermitian polynomial matrices," *IEEE Transactions on Very Large Scale Integration (VLSI) Systems*, vol. 22, no. 3, pp. 522–536, March 2014.

[109] S. Kasap and S. Redif, "Novel reconfigurable hardware implementation of polynomial matrix/vector multiplications," in *2014 International Conference on Field-Programmable Technology (FPT)*, Dec 2014, pp. 243–247.

[110] S. Kasap and S. Redif, "Fpga-based design and implementation of an approximate polynomial matrix evd algorithm," in *2012 International Conference on Field-Programmable Technology*, Dec 2012, pp. 135–140.

[111] F. K. Coutts, I. K. Proudler, and S. Weiss, "Efficient implementation of iterative polynomial matrix evd algorithms exploiting structural redundancy and parallelisation," *IEEE Transactions on Circuits and Systems I: Regular Papers*, vol. 66, no. 12, pp. 4753–4766, 2019.

[112] A. Eghbali, H. Johansson, and T. Saramäki, "A method for the design of farrow-structure based variable fractional-delay fir filters," *Signal Processing*, vol. 93, no. 5, pp. 1341–1348, 2013. [Online]. Available: https://www.sciencedirect.com/science/article/pii/S0165168412004057

[113] H. Johansson and P. Lowenborg, "On the design of adjustable fractional delay fir filters," *IEEE Transactions on Circuits and Systems II: Analog and Digital Signal Processing*, vol. 50, no. 4, pp. 164–169, April 2003.

[114] M. Alrmah, S. Weiss, and J. McWhirter, "Implementation of accurate broadband steering vectors for broadband angle of arrival estimation," in *IET Int. Signal Processing Conf. 2013*, Dec 2013, pp. 1–6.

[115] "An/ale-55 fiber-optic towed decoy (fotd)." [Online]. Available: https://www.baesystems.com/en-uk/product/an-ale-55-fiber-optic-towed-decoy

[116] W. Coventry, C. Clemente, and J. Soraghan, "Broadband sparse sensing: A polynomial matrix approach to co-prime and super nested arrays," in *2019 IEEE Radar Conference (RadarConf)*, April 2019, pp. 1–6.

[117] P. P. Vaidyanathan and P. Pal, "Sparse sensing with co-prime samplers and arrays," *IEEE Transactions on Signal Processing*, vol. 59, no. 2, pp. 573–586, Feb 2011.

[118] W. Coventry, C. Clemente, and J. Soraghan, "Enhancing polynomial music algorithm for coherent broadband sources through spatial smoothing," in *2017 25th European Signal Processing Conference (EUSIPCO)*, Aug 2017, pp. 2448–2452.

[119] Q. T. Zhang, "Probability of resolution of the music algorithm," *IEEE Transactions on Signal Processing*, vol. 43, no. 4, pp. 978–987, April 1995.